SYNTHESIS AND FABRICATION OF TRIMETALLIC (Ru-Mn-Co) CATALYST SUPPORTED ON TiO_2 AND $Ni(OH)_2$ THIN FILMS FOR PHOTOELECTROCHEMICAL APPLICATIONS

AHMAD NAZEER BIN CHE MAT

FACULTY OF SCIENCE
UNIVERSITI MALAYA
KUALA LUMPUR

2020

SYNTHESIS AND FABRICATION OF TRIMETALLIC (Ru-Mn-Co) CATALYST SUPPORTED ON TiO_2 AND $Ni(OH)_2$ THIN FILMS FOR PHOTOELECTROCHEMICAL APPLICATIONS

AHMAD NAZEER BIN CHE MAT

THESIS SUBMITTED IN FULFILMENT OF THE
REQUIREMENTS FOR THE DEGREE OF
DOCTOR OF PHILOSOPHY

FACULTY OF SCIENCE
UNIVERSITI MALAYA
KUALA LUMPUR

2020

UNIVERSITY OF MALAYA

ORIGINAL LITERARY WORK DECLARATION

Name of Candidate: **AHMAD NAZEER CHE MAT**

Registration/Matric No: **SHC 130081**

Name of Degree: **DOCTOR OF PHILOSOPHY**

Title of Project Paper/Research Report/Dissertation/Thesis (―this Work”):
SYNTHESIS AND FABRICATION OF TRIMETALLIC (Ru-Mn-Co) CATALYST SUPPORTED ON TiO_2 AND $Ni(OH)_2$ THIN FILMS FOR PHOTOELECTROCHEMICAL APPLICATIONS
Field of Study: **MATERIAL CHEMISTRY**

I do solemnly and sincerely declare that:

(1) I am the sole author/writer of this Work;
(2) This Work is original;
(3) Any use of any work in which copyright exists was done by way of fair dealing and for permitted purposes and any excerpt or extract from, or reference to or reproduction of any copyright work has been disclosed expressly and sufficiently and the title of the Work and its authorship have been acknowledged in this Work;
(4) I do not have any actual knowledge nor do I ought reasonably to know that the making of this work constitutes an infringement of any copyright work;
(5) I hereby assign all and every rights in the copyright to this Work to the University of Malaya (―UM”), who henceforth shall be owner of the copyright in this Work and that any reproduction or use in any form or by any means whatsoever is prohibited without the written consent of UM having been first had and obtained;
(6) I am fully aware that if in the course of making this Work I have infringed any copyright whether intentionally or otherwise, I may be subject to legal action or any other action as may be determined by UM.

Candidate‘s Signature Date: 09 MARCH 2020

Subscribed and solemnly declared before,

Witness‘s Signature Date: 09 MARCH 2020

Name:

Designation:

SYNTHESIS AND FABRICATION OF TRIMETALLIC (Ru-Mn-Co) CATALYST SUPPORTED ON TiO_2 AND $Ni(OH)_2$ THIN FILMS FOR PHOTOELECTROCHEMICAL APPLICATIONS

ABSTRACT

Anatase supported heterogeneous photocatalyst consisting of RuO_2, MnO_2 and Co_3O_4 (1:13:13 ratio) was synthesized by precipitation method. The film of the prepared catalyst was fabricated by electrophoretic deposition technique in an aqueous solution of 0.1 mM ammonia and tested for photoelectrocatalytic (PEC) oxidation of methanol in 0.1M KOH under visible light irradiation. The as-prepared photocatalyst was characterized by FTIR, UV–Vis, XRD, Raman spectroscopy, FESEM/EDX, TEM, BET, XPS and TPR. The PEC study by cyclic voltammetry indicates that the oxidation of methanol to CO_2 and H_2O upon exposure to visible light occurs between 400 and 800 nm. The smaller value of the charge transfer resistance (R_{ct}) of the RuO_2-MnO_2-Co_3O_4 supported anatase TiO_2 electrode indicates a faster rate of charge transfer at the electrode-electrolyte interface compared to the TiO_2 catalyst, which could be promising for direct methanol fuel cell application. Additionally, the trimetallic photocatalysts namely RuO_2-MnO_2-Co_3O_4 (1:13:13 ratio) supported anatase TiO_2 also was tested for photoelectrochemical reduction of CO_2 into formic acid in 0.2 M $LiClO_4$ in aqueous and N,N-dimethylformamide (DMF) under visible light. The photocurrent density in aqueous medium is higher than DMF with the value of 12 $\mu A/cm^2$ vs Ag/AgCl. The stable photocurrent from chronoamperometry revealing of good discernment of product where formic acid remains the major product in both aqueous and DMF medium. Furthermore, the photoelectrochemical reduction of CO_2 in aqueous and N,N-dimethylformamide (DMF) was also investigated over spherical $Ni(OH)_2$ photocatahode in 0.2 M $LiClO_4$ prepared by hydrothermal method was investigated under visible light irradiation. The band gap of $Ni(OH)_2$ obtained from UV-Vis spectroscopy was 1.8 eV which enabled efficient visible light absorption for the photoreaction. The porous spherical morphology of $Ni(OH)_2$ allows deeper penetration of light onto the active sites for better photocatalytic performance. The photocurrent density in aqueous and DMF solution at 0.2 V (vs. Ag/AgCl) were 24 mA/cm^2 and 5 mA/cm^2, respectively. Acetaldehyde and methanol are the major products in aqueous solution, while formic acid and methanol were the major products in DMF, after 6 hours of photoelectrolysis. The products formation from the photoelectrochemical reduction of dissolved CO_2 were 612 and 854 ppm in aqueous and DMF, respectively.

Keywords: Trimetallic (Ru-Mn-Co) catalyst supported on TiO_2, $Ni(OH)_2$, photoelectrochemical oxidation of methanol, phototelectrochemical reduction of CO_2, visible light

SINTESIS DAN FABRIKASI FILEM NIPIS PEMANGKIN TRILOGAM (Ru-Mn-Co) TERSOKONG TiO_2 DAN $Ni(OH)_2$ UNTUK APLIKASI FOTOELEKTROKIMIA

ABSTRAK

Fotopemangkin RuO_2, MnO_2 dan Co_3O_4 yang disokongi oleh TiO_2 berfasa anatas dengan nisbah 1:13:13 telah disintesis melalui kaedah pemendakan dan diuji untuk fotoelektropemangkinan pengoksidaan metanol dalam 0.1M KOH di bawah sinaran cahaya nampak. Fotopemangkin tersebut telah dicirikan menggunakan kaedah FTIR, UV-Vis, XRD, spektroskopi Raman, FESEM/EDX, TEM, BET, XPS dan TPR. Kajian PEC oleh kitaran voltametri menunjukkan bahawa pengoksidaan metanol kepada CO_2 dan H_2O apabila terdedah kepada cahaya tampak berlaku antara panjang gelombang 400 dan 800 nm. Nilai rintangan pemindahan cas (R_{ct}) yang lebih kecil oleh elektrod RuO_2-MnO_2-Co_3O_4 yang disokong TiO_2 anatas berbanding pemangkin TiO_2 menunjukkan kadar pemindahan cas lebih cepat pada antaramuka elektrod-elektrolit serta sesuai digunakan untuk aplikasi sel bahan api berasaskan metanol. Tambahan pula, fotopemangkin RuO_2-MnO_2-Co_3O_4 (1:13:13 ratio) berpenyokong TiO_2 fasa anatasa juga telah diuji keberkesanannya ke atas pembentukan asid formik melalui tindakbalas penurunan CO_2 menggunakan teknik fotoelektrokimia di dalam larutan akueus dan N,N-dimetilformamida (DMF) dengan kehadiran 0.2 M $LiClO_4$ di bawah cahaya nampak. Ketumpatan fotoarus di dalam keadaan akueus adalah lebih tinggi daripada DMF iaitu sebanyak 12 μA/cm^2 lawan Ag/AgCl sebagai elektrod rujukan. Daripada analisa kronoamperometri, kestabilan fotoarus yang didapati menunjukkan tahap selektiviti yang lebih baik dalam penghasilan asid formik samaada di dalam keadaan akueus ataupun DMF. Tambahan pula, proses penurunan CO_2 secara fotoelektrokimia juga telah diuji ke atas elektrod $Ni(OH)_2$ di dalam larutan yang sama seperti yang telah digunakan oleh

RuO_2-MnO_2-Co_3O_4 (1:13:13 ratio) berpenyokong TiO_2 fasa anatasa. Elektrod $Ni(OH)_2$ tersebut telah disediakan melalui kaedah hidrotermal. Jurang tenaga yang dipunyai oleh $Ni(OH)_2$ adalah 1.8 eV hasil daripada analisa spektroskopi UV-Vis dengan serapan cahaya nampak dalm lingkungan 500 – 750 nm. Imej permukaan $Ni(OH)_2$ yang berliang sangat penting dalam membenarkan penyerapan cahaya nampak dengan lebih berkesan ke atas bahagian-bahagian yang aktif pada $Ni(OH)_2$. Ketumpatan fotoarus di dalam larutan akueus dan DMF adalah 24 mA/cm^2 and 5 mA/cm^2, masing-masingnya. Di dalam larutan akueus, asetaldehid dan metanol adalah hasil utama manakala asid formik dan metanol adalah hasil utama tindakbalas di dalam larutan DMF. Kepekatan hsail-hasil selepas tindakbalas penurunan CO_2 adalah 612 and 854 ppm di dalam larutan berakueus dan DMF masing-masingnya.

Kata kunci: Pemangkin trilogam Ru-Mn-Co tersokong TiO_2, $Ni(OH)_2$, pengoksidaan fotoelektrokimia methanol, penurunan fotoelektrokimia CO_2, cahaya nampak

ACKNOWLEDGEMENTS

Firstly, I would like to thank my supervisors namely Dr. Nor Asrina Sairi and Prof. Dr. Wan Jefrey Basirun for their guidances and supports. This thesis would not be completed without their sacrifices.

I would also like to extend my appreciations to all of my colleagues from Chemistry Department and all staff of the department for their corporations and kindness in helping me from the beginning until the completion of my research.

Last but not the least, I thank my family for their support and encouragement that bring success to my life. Thank you all so much for all the support and sacrifices.

AHMAD NAZEER BIN CHE MAT

TABLE OF CONTENTS

LIST OF FIGURES

LIST OF TABLES

LIST OF SYMBOLS AND ABBREVIATIONS

BET : Bruneuer-Emmett-Teller
BTC : Benzene 1,3,5-tricarboxylic acid
Bu_4NPF_6 : Tetrabutylammonium hexafluorophosphate
CA : Chronoamperometry
CV : Cyclic voltammetry
DMFC : Direct methanol fuel cell
Dppz : Dipyrido[3,2-a:2′,3′-c]phenazine
EDX : Energy Dispersive X-ray
EIS : Electrochemical impedence spectroscopy
EPD : Electrophoretic deposition
FESEM : Field Emission Scanning Electron Microscopy
FTIR : Fourier Transform Infrared
GCE : Glassy carbon electrode
GCMS : Gas chromatography mass spectroscopy
LSV : Linear sweep voltammetry
MOF : Metal-organic framework
NHE : Normal hydrogen electrode
PEC : Photoelectrochemical
PL : Photoluminescence
XRD : X-ray diffraction
RHE : Reversed hydrogen electrode
SHE : Standard hydrogen electrode
TPR : Temperature programmed reduction
TBAP : Tetrabutylammonium perchlorate
UV-Vis : Ultraviolet Visible

PREFACE

The objective of this thesis is to explore the inexpensive metal oxide-based catalysts namely RuO_2-MnO_2-Co_3O_4 supported onto anatase TiO_2 and $Ni(OH)_2$ for the photoelectrochemical oxidation of methanol and reduction of CO_2 gas, respectively under normal conditions of room temperature and atmospheric pressure. Attempts have been made to deliberate precipitation and hydrothermal method to synthesize the aforementioned photocatalysts. The electrophoretic deposition method was implemented in order to fabricate the thin films for photocatalytic activity under visible light irradiation.

In brief, RuO_2-MnO_2-Co_3O_4 supported onto anatase TiO_2 was tested for two photoelectrochemical studies namely methanol oxidation and CO_2 reduction reaction. The methanol oxidation and CO_2 reduction reactions were intere-related with each other since reducing CO_2 produced methanol while oxidizing methanol produced CO_2. These reactions are paramount important for generating green energy such as direct methanol fuel cell (DMFC) and other chemicals. Precipitation method was used to prepare RuO_2-MnO_2-Co_3O_4 supported onto anatase TiO_2. Then, the catalyst was cured under H_2 and O_2 atmosphere at high 450 ^{o}C a tube furnace. The curing of the prepared catalyst in such reductive and oxidative atmosphere helps to maintain the oxidation state of ruthenium (Ru), manganese (Mn) and cobalt (Co) which provide the necessary active sites in order for the photocatalytic reaction to proceed. The second photocatalyst namely $Ni(OH)_2$ was prepared by hydrothermal method in aqueous medium in the presence of urea as capping agent. The alkalinity of $Ni(OH)_2$ helps to capture more acidic CO_2 onto its surface which might help in reducing CO_2 into organic oxygenates. Additionally, the transformation from $Ni(OH)_2$ to NiO during the reaction further increase the conversion efficiency of CO_2 with the mechanism involved also discussed.

This thesis is divided into five chapters where **Chapter 1** provides general rationalizations of the thesis which focusing on two major issues namely environment and energy. **Chapter 2** describes into details on the literature summaries regarding the development of semiconductor-based photocatalysts and their applications in energy generation such as photocatalysis including methanol oxidation and CO_2 conversion. This chapter also elaborates further the implemented synthetic technique to synthesize RuO_2-MnO_2-Co_3O_4 supported TiO_2 and $Ni(OH)_2$ namely precipitation and hydrothermal method, respectively. Furthermore, electrophoretic deposition method for the fabrication of thin film also is described in this chapter. The findings based on the previous works in the field of methanol oxidation and CO_2 reduction reaction are introduced at the end of this chapter.

Meanwhile, **Chapter 3** describes the details on the materials, experimental procedures, synthetic methodology namely precipitation, thin film fabrication method namely electrophoretic deposition methods and instrumental characterizations such as XRD, FTIR, Raman, UV-Vis, FESEM-EDX, XPS, BET, TPR and electrochemical studies including CV, LSV, CA and EIS analysis of the chosen catalysts.

Chapter 4 focus mainly on the results and discussions of the prepared catalysts based on the characterization techniques mentioned in **Chapter 3** above. The conclusions of the findings of the present research works and some recommendations for further investigations are included in **Chapter 5**.

CHAPTER 1: INTRODUCTION

1.1 Energy and environmental crisis.

After the industrial revolution, human being began to create new technologies that could provide energy and facilitate their daily works. However, we actually forget that the environment and energy sources are closely related to each other. The dependence of more than 80% of the energy source on natural fuel combustion comprising liquefied petroleum, coal and natural gas (Yu et al., 2008) has contributed to the release of CO_2 gas and other carbonaceous particles into the atmosphere and indirectly changing the world's weather to become warmer as proposed by Arrhenius for more than 200 years ago. The global increase in temperature invites some unavoidable natural disasters such as rising sea levels as a result of ice meltdowns in the north and south poles, extreme weather events such as changes in tropical cyclones and hurricanes frequency and intensity, glaciers retreat as well as acidification of the ocean have been discussed and observed by several researchers (Hoyos et al., 2006; Orr et al., 2005; Rahmstorf et al., 2007).

The increasing concentration of CO_2 gas has been exceeded 400 ppm recently is expected to be further increased to 550 ppm before the end of this century (Hoffert et al., 2002; Hoffert & Covey, 1992). Due to the uncontrolled emission of CO_2 gas, numerous methods had been set to reduce its release to the environment either through carbon capture and sequestration by using solid sorbent such as zeolite, mesoporous molecular sieve and metal organic framework or amines adsorbent (Chen et al., 2016; Gholidoust et al., 2017; Hedin et al., 2010; Just, 2013; Silvestre-Albero et al., 2011; Siriwardane et al., 2005; Wang et al., 2011), conversion into value-added chemicals either through electrochemical, photochemical, photoelectrochemical, photoelectrochemical, biological or thermal reduction methods (Hu et al., 2013; Ichikawa & Doi, 1996; Kuramochi et al., 2014), being recycled into beverage industry or utilization of CO_2 as a medium for energy recovery, heat transfer and solvent (Song, 2006). However, the methods described above are still inadequate to curb the increasing emissions of CO_2 gas into the air which is estimated to reach 42.3 Gt in 2019 although the increase in the amount of carbon dioxide gas in the air is only around 3% between 1990 – 2019 (Friedlingstein et al., 2014).

1.2 Solar energy.

Since generations, the sun is the main source of energy for humans and other organisms on earth. Without sunlight, all levels of living organisms will be extinct. Every year, the earth receives a substantial amount of sunlight of 178,000 TW (1 TW = 10^{12} W) and this amount is more than sufficient than what human beings are currently consuming on earth (Hoffmann et al., 2011; Nealson & Conrad, 1999). However, the incident solar energy on Earth further decreases to 120,000 TW when almost half of the energy is reflected back into space while the rest were absorbed by the oceans, clouds and land masses. Nearly 30% of the Earth is covered by land and to utilize solar energy, solar panels are installed only on land and this makes the amount of sunlight received steadily reduced to 36,500 TW. Nevertheless, in 2009, it is estimated that the annual amount of world energy consumption is much lower than the Earth's accepted energy of 16.6 TW only. In order to realize this energy consumption, only 0.2% of the total land area of the Earth is required to be installed with solar panels (Gust et al., 2009).

Therefore, numerous researchers around the globe have already tried diversity of methods to utilize solar sources with the creation of sophisticated technologies such as photovoltaic as well as electrochemical cells to convert energy in the form of sunlight to electricity to facilitate human daily works. Nevertheless, even the more we advance forward with the increasing number of world populations each year, the level of energy consumption is always beyond our ability to utilize and convert sunlight to electricity due to high fabrication cost, low output power density and insufficient light harvesting.

Because of that, we are still rely on non-renewable energy when 85% of the world's energy resources now come from combustion of fossil fuels which consist petroleum oils, natural gas and coal which contribute about 38%, 27.3% and 34.7% out of the total fossil fuel, respectively (Yuan et al., 2014). Combustion of these fossil fuels will certainly increase the release of carbon dioxide into the air and thereby invite more environmental problems as described above.

1.3 Motivation from nature.

The abundance of sunlight received by the Earth has been utilized by green plants, algae and cyanobacteria in the process of photosynthesis to produce carbohydrate (sugar) and oxygen gas from the reduction of carbon dioxide gas in the presence of water at pH of 6-8. The production of oxygen gas in photosynthesis requires eight photons and the process is divided into two separate light systems namely the photosystem I (PSI) and the photosystem II (PSII) systems. The reaction of oxidation of water with the release of oxygen gas occurs on the PSII system using the so-called oxygen evolving complex namely $CaMn_4O_5$ (Dau & Zaharieva, 2009; Tsui et al., 2013). Whereas the reduction of carbon dioxide gas to carbohydrates such as glucose and oxygen gas release occurs on PSII system using electrons and protons from water oxidation reaction in the system PSI. However, the percentage of conversion efficiency is very low which is only in the range of 8 - 9% (Bolton & Hall, 1991). Hence, it is insufficient enough to reduce the concentration of CO_2 gas which is increasing every day in the air and furthermore, very difficult to device a system that is perfectly mimic natural photosynthesis.

In brief, photosynthesis by green plants involves four major processes, namely solar absorption by green pigment called chlorophyll that converts the light energy into adenosine triphosphate (ATP) and nicotinamide adenine dinucleotide phosphate (NADPH), separation of photogenerated charge carriers, water oxidation and fuel production from the reduction of CO_2 gas. Although it is very difficult to mimic natural photosynthesis, but we can imitate the template of natural photosynthesis which is so-called artificial photosynthesis by using photoelectrocatalysis (PEC). There are two fundamental concepts can be adopted from the natural photosynthesis namely energy flow and electron flow in order to power any photocatalytic reaction. The energy from the sun needs to be harvested effectively by photoactive catalyst in order to excite the electron to drive a chemical reaction. The concept PEC is to combine the heterogeneous photocatalyst with electrochemical studies. The advantage of PEC studies over heterogeneous photocatalysis system is the separation of reduction and oxidation reaction sites where product crossover can be minimized. Furthermore, high efficiency can be obtained by using PEC system as compared to powdery photocatalysis system.

1.4 Problem statements.

Since generations, the sun is the main source of energy for all living organisms on earth. Without sunlight, all living organisms will be extinct. Researchers around the globe attempted to diversify the methods to utilize solar sources with the creation of sophisticated technologies suach as photovoltaic as well as electrochemical cells to convert energy in the form of sunlight to electricity to facilitate human daily works. However, due to high device fabricating cost, low output power density and insufficient light harvesting, these accurance has limit the efficiency of the solar light harvesting and its conversion into electricity. Because of this, the combustion of natural fossil fuel is still a major source of energy today. Combustion of this natural fossil fuel releases a remarkable amount of CO_2 into atmosphere which contributes to the environmental pollution besides the depletion of natural fossil fuel in future.

Hence, in order to solve this two major problems namely the source of energy due to the depletion of natural fossil fuel and environmental pollution due to the accumulation of CO_2 from the burning of fossil fuel, an exigent discoveries are needed from academician and industrial experts to search for an alternative source of energy. There are several ways to encounter these problems. Among them is to capture and convert the released CO_2 form the industrial plant into useful chemicals such as methanol. The other method is to mimic natural photosyntheis of the green plant by harvesting solar light in the present of efficient catalyst to produce valuable chemicals such as formic acid, methanol and ethanol.

However, reduction of CO_2 molecule into other useful chemicals as mentioned above is not as easy as expected. The stability of CO_2, high reaction overpotential, high recombination rate of photogenerated charge carriers, stability of photocatalyts in the reaction medium, excessive competition between hydrogen evolution reaction and low absorption of visible light retard the efficiency of CO_2 reduction reaction. Hence, in this study, two photocatalysts, namely RuO_2-MnO_2-Co_3O_4 supported anatase TiO_2 and $Ni(OH)_2$ have been prepared for photoelectrochemical applications such as CO_2 reduction and oxidation of methanol.

1.5 Research objectives.

The main objective for the current research is to develop efficient photocatalysts for photoelectrochemical studies of methanol oxidation and CO_2 reduction reaction under visible light irradiation. However, the specific objectives of the present study can be divided into several points as follows:

(i) To synthesis and fabricate thin films of trimetallic oxides of RuO_2-MnO_2-Co_3O_4 supported anatase TiO_2 and $Ni(OH)_2$, photocatalysts.

(ii) To characterize the prepared photocatalysts by means of XRD, FTIR and Raman, UV-Vis, FESEM/EDX, TEM, BET, and TPR for their phase, structural, morphology and elemental ratio, surface area and reduction temperature analysis respectively.

(iii) To examine the efficiency of RuO_2-MnO_2-Co_3O_4 supported anatase TiO_2 and $Ni(OH)_2$ photocatalysts for photoelectrochemical oxidation of methanol and CO_2 reduction, respectively.

(iv) To propose reaction pathways for the photoelectrochemical oxidation of methanol and CO_2 reduction over RuO_2-MnO_2-Co_3O_4 supported anatase TiO_2 and $Ni(OH)_2$ photocatalysts.

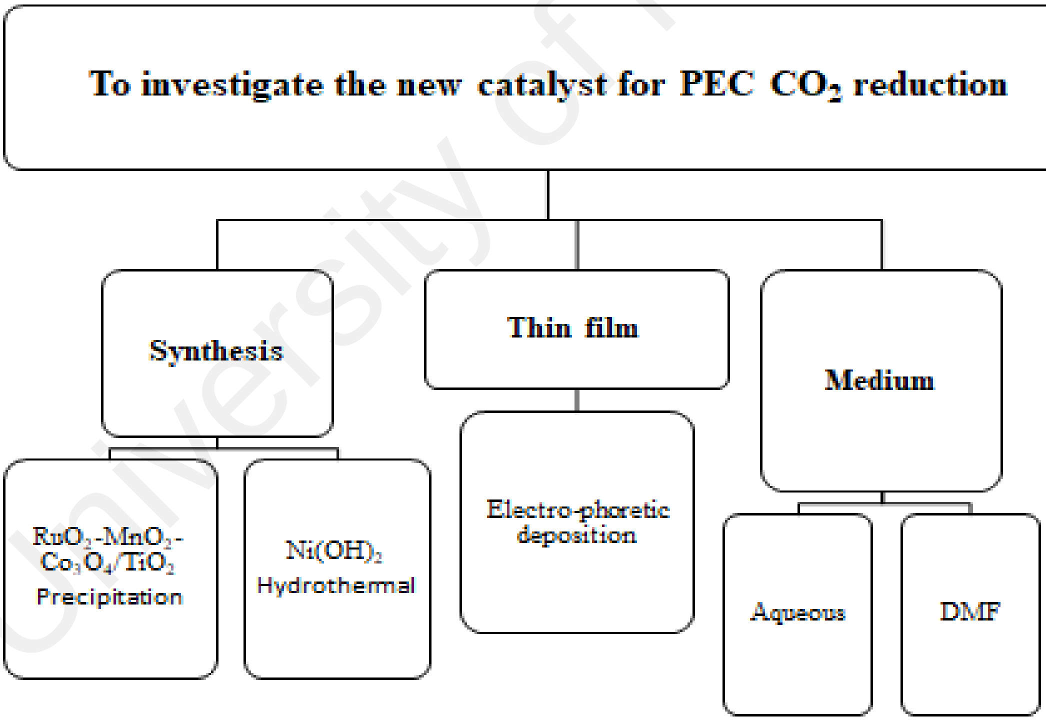

Figure 1.1: Schematic diagram of research objective.

CHAPTER 2: LITERATURE REVIEWS

In Chapter 2, this thesis attempts to divide the discussions based on several issues. At the outset of the Chapter 2, this thesis will introduces about the broad properties of carbon dioxide followed by the discussions regarding absorption technologies of carbon dioxide available nowadays. This chapter also attempts to introduce and discuss the thermal and photocatalytic processes including the implementation of semiconductors and metal complexes for the activation and utilization of carbon dioxide into valuable organic oxygenates such as formic acid, methanol, ethanol and oxalic acid which have been recently reported in the literature (de Brito & Zanoni, 2017; Lee et al., 2018; Shi et al., 2019). Apart from that, the other energy generation related reactions such as oxidation of methanol for direct methanol fuel cell (DMFC) and oxidation of water into hydrogen and oxygen were also discussed in this chapter.

2.1 Photocatalysis

Environmental pollution and the demand of the people for energy in this century have forced researchers in the academic or industrial fields to explore clean, recyclable sources of energy such as wind, biomass, solar and geothermal as alternative sources of energy instead of natural fossil fuel. Solar energy is seen to be more beneficial than other energies as the earth receives a considerable amount of solar energy throughout the year, which exceeds human consumption. Sunlight can be used as a source of energy to split water to H_2 and O_2 (Kudo & Miseki, 2009). It also involves in production of sugar and fuel from the process of CO_2 reduction (Yu et al., 2014) as well as treatment for polluted water from the textile industry, oil spills and excess of toxic substances from the industry (Kudo & Miseki, 2009; Legrini et al., 1993). **Figure 2.1** gives an overview on the variety of applications of heterogeneous photocatalysts.

Photocatalysis can be defined as the conversion of a substance through a chemical reaction when an electromagnetic radiation is adsorbed by an entity accelerated with the presence of a catalyst. The history of research on the photocatalysis has long been about 40 years ago when Honda and Fujishima in their experiments managed to oxidize water to H_2 and O_2 by using titania (TiO_2) as a catalyst (Fujishima & Honda, 1972). After the amazing discovery, research on photocatalyst such as TiO_2 and other oxides are increasing rapidly. TiO_2 is chosen as favourite photocatalyst due to its high stability, cheap, naturally abundant material, resistance to photocorrosion and non-toxic (Su et al., 2004). In spite of the advantages mentioned above, TiO_2 is only photoactive in ultraviolet region, therefore most of the visible light which constitutes a major portion of the sunlight is not utilized. Furthermore, the fast recombination rate between the photogenerated conduction band electrons and valence band holes in TiO_2 limits the performance towards certain applications (Ni et al., 2007). However, a large fraction of these charge carriers often recombine by dissipating energy in the form of heat before reaching the surface to initiate the chemical reaction. Nevertheless, only the well-separated electrons and holes will migrate to the surface and initiate redox reactions with the adsorbed molecules. Therefore, a challenge that needs to be addressed is to find an excellent catalyst that can operate under the visible light with minimum charge carriers recombinations (Cozzoli et al., 2003; Tachikawa et al., 2007).

Photocatalyst comes from a combination of two words namely photo which mean light and catalysts defined as a substance that speeds up the reaction rate of chemical reaction by lowering the activation energy of reaction without being consumed during the reaction and participitating in the production of new products. Thus, phototocatalyst can be described as an acceleration of chemical reaction to produce a substance in the presence of light and semiconductor as a catalyst. However, there are some basic things that need to be understood in the context of photocatalysis. A semiconductor to be photocatalysis must be capable of absorbing as much as possible the light from the sun ranging from UV to infrared which will give energy to the electrons within the semiconductor. Electrons that have enough energy will be excited to the higher level of the conduction band and leave a positively charged entity or vacant spot in the valence band called hole. For a chemical reaction to be performed through the photocatalysis process, the resulting electrons must have a chemical potential between +0.5 to -1.5V while the hole should have a chemical potential value between +1.0 to +3.5 V versus Normal Hydrogen Electrode (NHE). Both photogenerated electrons and holes must be capable of reacting with electron donors and electron acceptors, which are trapped on semiconductor surfaces, facilitate the reduction and oxidation reactions, and desorption of product back to the bulk solution. Another thing to note is the process of charge carrier recombination that converts the light energy absorbed into heat release into the environment. Recombination of this process can occur in many conditions such as surface or electrical double layer. Typically, scavenger or crystalline defects inherent in semiconductors that can trap the resulting electrons and holes cause this recombination. Therefore, a better crystallinity with minimum defects needs to be made so that photogenerated charge carriers can quickly transfer to the surface and reduce the recombination process and increase photocatalytic efficiency (Wang et al., 2014). **Table 2.1** below represents the applications of various photocatalysts.

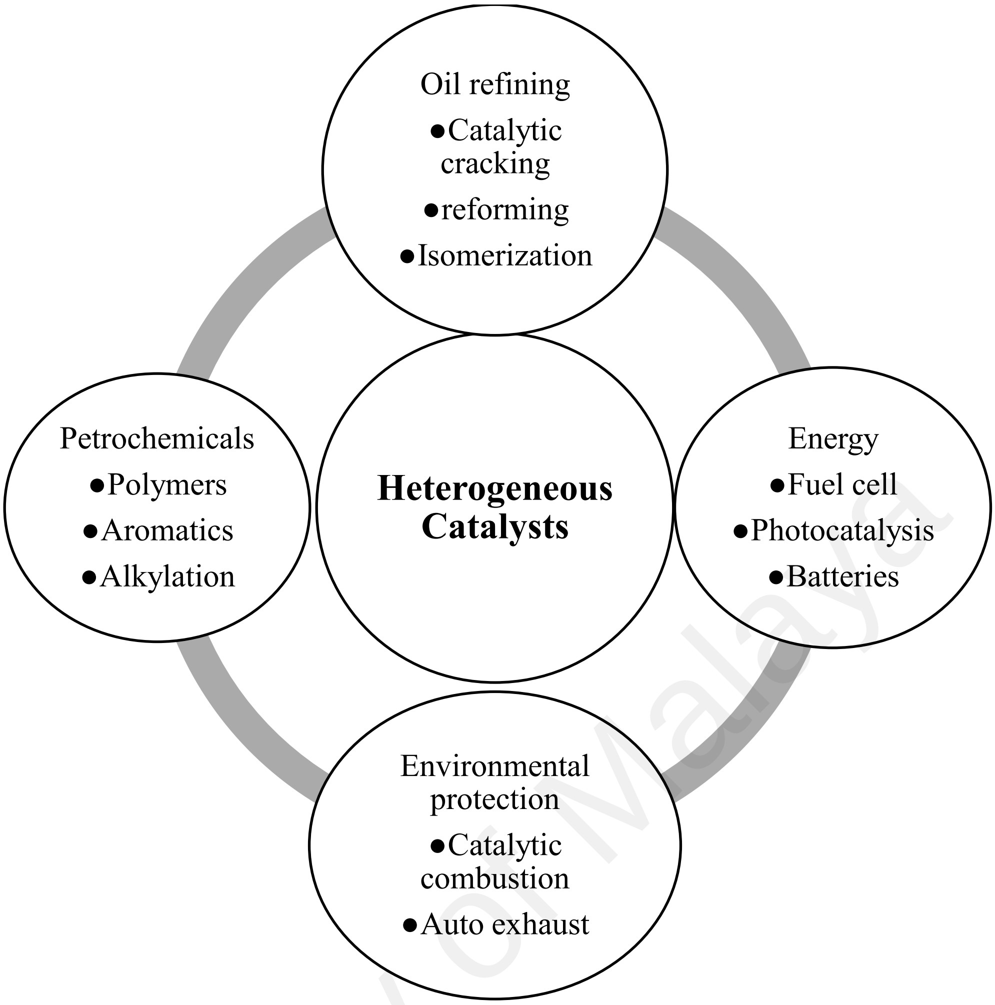

Figure 2.1: Applications of heterogeneous catalysts.

Table 2.1 Recent applications of various photocatalsyts.

Photocatalysts	Preparation method	Bandgap (eV)	Structure	Photocatalytic applications	Ref.
Ni/ZnO/CdS	Biotemplate	2.88	Onion	Cyanobacteria removal	(Serrà et al., 2020)
5% Ag-doped TiO_2, ZnO, ZnS	Sol-gel	2.92 – 3.13	Spherical	Degradation of 2-chlorophenol	(Onkani et al., 2020)
$MnMoO_4/NiFe_2O_4$	Hydrothermal	1.06	Cubic	Degradation of dye	(Paul & Dhar, 2020)
$AgI/BiVO_4$	Hydrothermal	2.24	Micron-seized blocks	Degradation of dye	(Lakhera et al., 2020)
Fe_3O_4/biochar (Sewage sludge, soft wood pellets, rice husk).	Impregnation	2.27 – 2.92	Honeycomb	H_2 evolution	(Norouzi et al., 2019)
BiOBr	Hydrothermal	2.04	Flower	Degradation of pollutant	(Chang et al., 2019)
$CdS/MoS_2/WS_2$-Pt	Microwave	1.04 – 1.88	Granular	H_2 evolution	(Sun et al., 2020)
C_3N_4	Sol-gel	2.8	Porous with agglomeration	Degradation of diclofenac	(Shojaeimehr et al., 2020)
TiO_2	In-situ complexation-hydrolysis	N/A	Nanofiber	Water purification	(Dong et al., 2020)
$Gd/SiO_2/TiO_2$	Sol-gel	3.05	N/A	Degradation of methylene blue	(Feng et al., 2019)
$GO/CdS/CuFe_2O_4$	Hydrothermal	N/A	Spherical	Degradation of dinoseb and imidacloprid	(Zangiabadi et al., 2020)

Table 2.1, continued.

ZnS	Aerosol assisted chemical vapour deposition (aacvd)	3.4	Flower	Water splitting	(Ehsan et al., 2013)
M/TiO_2 (M = Pd, Au)	Self-essembly	~2.30	Spherical	H_2 evolution	(Luna et al., 2020)
SnO_2/TiO_2	AACVD	2.8	Flower	Water splitting	(Naeem et al., 2018)
$ZnO/BiVO_4$	Hydrothermal	N/A	Nanorod	Water treatment	(Chang et al., 2020)
$Ag_3PO_4/AgBr/g\text{-}C_3N_4$	Chemical deposition technique	2.38 - 3.02	Spherical	Degradation of tetracycline	(Yu et al., 2020)
$V/TiO_2/In_2S_3$	AACVD	2.3	Nanorod	Water splitting	(Mumtaz et al., 2016)
α-Fe_2O_3/poly(3-hexylthiophene)/polyoxometalate O-Ti-O	Hydrothermal	2.01 – 2.23	Agglomeration	Degradation of bisphenol A	(Zhu et al., 2020)
MoO_3/Bi_2O_4	Hydrothermal	1.9 – 2.8	Nanoblock	Degradation of rhodamine B	(Jiang et al., 2020)
α-$Fe_2O_3/g\text{-}C_3N_4/ZnO$	Sol-gel	2.6	Aggregation of wrinkled and flat sheets structure	degradation of tartrazine dye	(Balu et al., 2019)
$WO_3/ZnIn_2S_4$	Solvothermal	2.4 – 2.75	Nanorod	Degradation of nitenpyram	(Tang et al., 2019)
$MgTi_2O_5$	AACVD	3.4	Spherical	Water splitting	(Ehsan et al., 2017)

Table 2.1, continued.

Ag/$LaTiO_3$	Hydrothermal	2.37	Needle	Degradation of atrazine	(Shawky et al., 2020)
Bi_2O_3/Bi_2MoO_6	In-situ alkaline treatment	N/A	Flower	H_2 evolution	(Fu et al., 2019)
Fe/I/TiO_2	Sol-gel	2.86	N/A	Degradation of benzene	(Tian et al., 2020)
WO_3/TiO_2	Induced liquid phase plasma	3.04	Cubic	Degradation of diethyl phthalate	(Ki et al., 2019)
TiO_2/AlON	Carbothermal reduction and nitridation	N/A	Porous skeleton structure	Degradation of Methylene blue	(Xu et al., 2019)
Bi_2O_3/BiOBr	Ultrasonication	2.39	Spherical	Degradation of bacteria	(Li, Wang, et al., 2020)
$SrTiO_3$/($BiFeO_3$@ZnS)	Solvothermal+sol-gel	2.05-3.3	Spherical	Degradation of 2,4-dichlorophenol	(Qu et al., 2020)
$Bi_xSb_{2-x}S_3$	Hydrothermal	2.3	Nanorod	Degradation of Rhodamine B	(Dashairya et al., 2020)
Pt@$BiVO_4$/g-C_3N_4	Impregnation	2.42	Nanoblock	Degradation of industrial waste	(Samsudin et al., 2019)

2.2 Semiconductor in photocatalysis

Photocatalyst can be categorized into two types, namely homogeneous and heterogeneous photocatalysts. Homogeneous photocatalysts are often dissolved in a solution during chemical reactions and the difficulty in separating them from the reaction products results in less favourable from the economic point of view. While the heterogeneous photocatalysts occur when there are two different phases between catalysts and the reactants. Generally, several processes of reaction occur before obtaining the desired product such as the diffusion of molecules in bulk solution, the molecular movement or adsorbtion to the catalyst surface, the redox processes occur on the surface, the desorption of the product and the diffusion product to the bulk solution (Pirkanniemi & Sillanpää, 2002). The use of heterogeneous photocatalyst is preferred as it happens at ambient temperature and pressure, the difficulty in product separation process can be avoided, high yield and purity, low cost oxidation agents, is considered green technology because the process of decomposition of products such as CO_2, water and mineral acids involve mild acidity. Since the chemical reaction in the heterogeneous photocatalysts occurs on the catalyst surface, then the reaction is also different whether the excitation occurs on the surface of the catalyst or adsorbate molecule. If the excitation occurs on the surface of the adsorbate molecule followed by a reaction with the catalyst, it is said to be catalysed photoreaction. On the other hand if excitation occurs on the surface of the catalyst and involves the transfer of electrons to the adsorbate molecules, they are called sensitized photoreaction (Linsebigler et al., 1995). The electronic structure of semiconductor can be divided into three main areas namely forbidden band, valence band (E_v) and conduction band (E_c). For pure semiconductor, no energy state is allowed to be in the forbidden band. The energy state is only allowed to be in higher or lower than forbidden bands. If the level of electronic energy in the vacuum is used as a reference, the lowest energy level is called the valance band where the electrons are placed. These electrons can be propagated to a higher energy level namely conduction band which has no electrons in it. This excitation process can be made either thermal or optical. Once the electron is excited to the conduction band, it will leave a vacant space that is positively charged so-called hole. For semiconductors where their E_v and E_c can not be experimentally determined, the equation below may be used to determine the value of both bands (Xu & Schoonen, 2000):

$$E_c = -\chi + 0.5\, E_g \tag{2.1}$$

$$E_v = -\chi - 0.5\, E_g \tag{2.2}$$

where χ electronegativity value and E_g is the band gap i.e the difference between E_v and E_c. In addition, the semiconductor size also plays a role in determining the electronic properties of a semiconductor. Quantum size effect will occur if the semiconductor size is equal to or smaller than the Bohr radius in which a particle will have both the bulk properties and molecular phases (Hagfeldt & Graetzel, 1995). This effect often occurs for semiconductors whose size is almost or less than 10 nm. If the size is too small, the band gap value will increase, as well as for E_c and slightly decrease in E_v (Beydoun et al., 1999). Typically, the photocatalyst efficiency is taken into account when photogenerated electrons and holes are displaced as far as possible to each other and reach the surface of the catalyst for further reactions. However, more than 90% of the energy is wasted due to the process of recombination between photogenerated electrons and holes resulting in reduced overall photocatalytic efficiency. This recombination process can occur either in the volume or on the surface of the photocatalyst (Linsebigler et al., 1995).

Most semiconductor suffer from recombination process (**Figure 2.2**) because of the duration of the photogenerated e^-/h^+ recombination is much shorter than the diffusion rate of the e^-/h^+ to reach the surface (Alfaifi et al., 2018). This is evidenced by the analysis of femtosecond and picosecond transient absorption and emission spectroscopy which studies the charge carrier trapping and recombination rate in ZnO. The results of the analysis show that the electron trapping time is between 20-200 fs and the recombination process takes only 30 ns. However, the recombination process remains in the interval between nanosecond and picosecend (Colombo & Bowman, 1996; Serpone et al., 1995; Skinner et al., 1995). Typically, particle size is closely related to this e^-/h^+ recombination process. The ideal size to reduce the recombination process is between 10 - 15 nm. If the size is smaller than the ideal size, the existence of the quantum size effect as discussed above needs to be considered. The inevitable recombination among semiconductors is due to the presence of impurities, lattice defects and vacancies that exist on the surface, the boundary between two semiconductors or the bulk of the semiconductor (Almquist & Biswas, 2002).

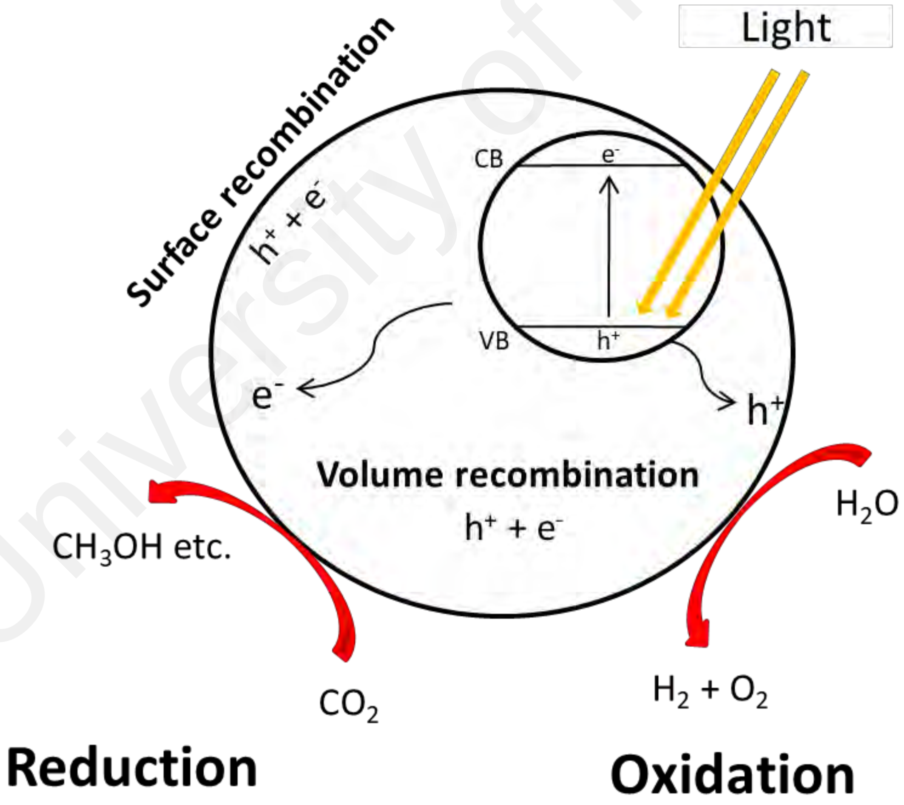

Figure 2.2: Photocatalytic processes in semiconductor.

2.3 Charge transfer enhancements

Various ways have been practiced to increase the electron separation and transfer to the surface of the photocatalysts and reduce the recombination reaction from occurring in order to enhance the photocatalytic activity in any photocatalytic applications (**Figure 2.3**). In this thesis, there are several ways that can be summed up for the aforementioned purposes, among others: (i) combining two semiconductors with different band gap values, (ii) surface modification through the fabrication of metal-semiconductor, (iii) couple semiconductor-carbon materials such as graphene, carbon nanotubes, (iv) simultaneous scavenging of e^-/h^+ by surface adsorbed redox species and (v) by using charge carrier trapping.

Fabrication of semiconductor-semiconductor heterojunction typically has been implemented in order to enhance photogenerated charge carriers separation and/or minimizing the recombination process. In this method, semiconductor-semiconductor heterojunction can be divided into two categories namely p-n heterojunction and non-p-n heterojunction. Storage and separation of charges are effective in the context of p-n heterojunction. This is because the combination of p- and n-type semiconductor can create space-charge region at the interface due to the diffusion of photogenerated e^-/h^+ resulting in a built-in electric field that can lead the e^-/h^+ to move in the opposite direction. When exposed to light, e^-/h^+ is separated by the built-in electric field where electron will move towards the conduction band of n-type semiconductor while holes will be directed to the valence band of p-type semiconductor (Jiang et al., 2012). Some advantages in the use of p-n heterojunction are the rapid separation and transfer of charge carriers to the catalyst and the lifetime of the charge carriers can be prolonged. In the context of non p-n heterojunction, two semiconductors of A and B are bounded with each other to form a remarkable heterojunction. If conduction band of semiconductor A is higher than conduction band of semiconductor B and valence band of semiconductor

B is lower than valence band semiconductor of A, under the presence of light, conduction band of semiconductor B will receive electron from the semiconductor A while holes from the valence band of semiconductor B will move in opposite direction of the electron stream towards valence band of semiconductor A. This method can overcome the recombination process of charge carriers without any obstacles for further redox reactions. For example, $BiWO_6$-TiO_2 nanoplate has been successfully synthesized by using electrospinning method showing that the photocatalytic efficiency is eight times higher than bare $BiWO_6$ against acetic acid decomposition. High catalytic activity is caused by lack of recombination between e^-/h^+ on $BiWO_6$-TiO_2 (Shang et al., 2009). Moreover, Rhodamine B (Rh B) decomposition is 2.5 times higher over SnO_2-TiO_2 when compared to bare TiO_2 due to the excellent charge separation process after two semiconductor are combined (Wang et al., 2009). Apart from the TiO_2 based catalyst, the WO_3-$BiVO_4$ fabricated by layer-by-layer deposition method of WO_3 and $BiVO_4$ on conductive glass also showed increased photocurrent by 1.74 and 7.3 times compared to the bare WO_3 and $BiVO_4$ (Hong et al., 2011).

When combined with metal-semiconductor, electron flows will occur from high Fermi level to low Fermi levels to create an area called Schottky barrier at the interface of metal-semiconductor where the metal will have a positive charge surplus while the semiconductor will have a surplus of charge negative. This phenomenon can usually be seen on n-type semiconductors such as TiO_2 where electrons flow from TiO_2 which has lower working functions than metals. The Schottky barrier was found to enhance the photocatalytic activity because it acts as an electron trap and indirectly reduces the recombination of charge carriers. For example, the addition of 0.5 wt% Au to TiO_2 prepared by the multicomponent assembly approach process was found to have catalytic activity three times that of bare TiO_2 in the phenol oxidation reaction and the reduction of Cr resulted from improved light absorption capability (Li et al., 2007). In addition, combinations of metals such as Cu, Ag and Au on p-Si for CO_2 reduction have increased the photovoltage value by 0.5 V (Hinogami et al., 1998). Furthermore, the use of plasmonic photocatalysts such as Ag-AgX (X = Cl-, Br-, PO_4^{3-}) prepared from various techniques such as polyol, hydrothermal and ion exchange methods can enhance photocatalytic efficiency compared to pure AgCl, AgBr and Ag_3PO_4 towards the decomposition of compounds organic such as RhB and methyl orange (MO) due to efficient charge separation and transfer through silver particles (Bi et al., 2012; Wang et al., 2014).

Semiconductor-carbon heterojunction is formed when a semiconductor is combined with carbonaceous materials such as activated carbon compounds, carbon nanotubes (CNTs) and graphene. The large surface area properties give advantages to these carbon compounds to be used as support in various photocatalyst reactions such as water decomposition to H_2 and O_2, decomposition of organic compounds and reduction of CO_2 gas to oxygenated hydrocarbons such as methanol, ethanol, formic acid and so forth (Gao et al., 2011; Ge et al., 2017; Kecsenovity et al., 2016). CNT for example, has a very special feature such as having conductivity like metallic semiconductor and can form a Schottky barrier when combined with it. In addition, CNT has high capacity and capability as electron storage and this reduces the probability of a charge carrier recombination that can increase photocatalytic activity. Once exposed to light, photogenerated charge carriers will be produced with electrons going to CB of TiO_2 and subsequently to the CNT surface until the Fermi levels of the semiconductor and CNT are in equilibrium for the reduction reaction to take place, whereas holes continus to remain in VB TiO_2 for oxidation reaction (Hoffmann et al., 1995).

The next strategy to enhance the photocatalytic activity is through the addition of electron acceptor and donor. This is because without the presence of electron acceptor and donor, severe charge carriers recombination will occur thereby affecting the activity and efficiency of the overall photoreaction. Decomposition reaction of organic chemical compounds is more effective in the presence of electron acceptor compounds such as oxygen by reducing the e^-/h^+ recombination rate. In addition, electron acceptor helps to increase the production of hydroxyl radicals ($^{\bullet}OH$) which are very important in the decomposition reactions of organic compounds. In addition, the formation of other radical species can be enhanced in the presence of electron acceptor. Among the compounds that can be used as an electron acceptor other than oxygen are H_2O_2, $KBrO_3$ and $K_2S_2O_4$ (Bahnemann et al., 2007; Wei et al., 2009). Moreover, the addition of a donor electron (hole scavenger or sacrificial agent) can also enhance the photocatalytic efficiency of a reaction. This electron donor species is very important in the photocatalysis reaction so it can react with the photogenerated hole of the VB of a semiconductor and at the same time reduce the recombination process. Among the commonly used electron donor in photocatalytic reactions are methanol, ethanol, lactic acid, formaldehyde, cyanide ions (CN^-) and ethylenediaminetetraacetic acid (EDTA). Therefore, with the use of donor electrons, the resulting carrier carrier can be separated and transferred to the surface of the photocatalyst for redox reactions more efficiently (Bamwenda et al., 1995; Li et al., 2003; Wu & Lee, 2004).

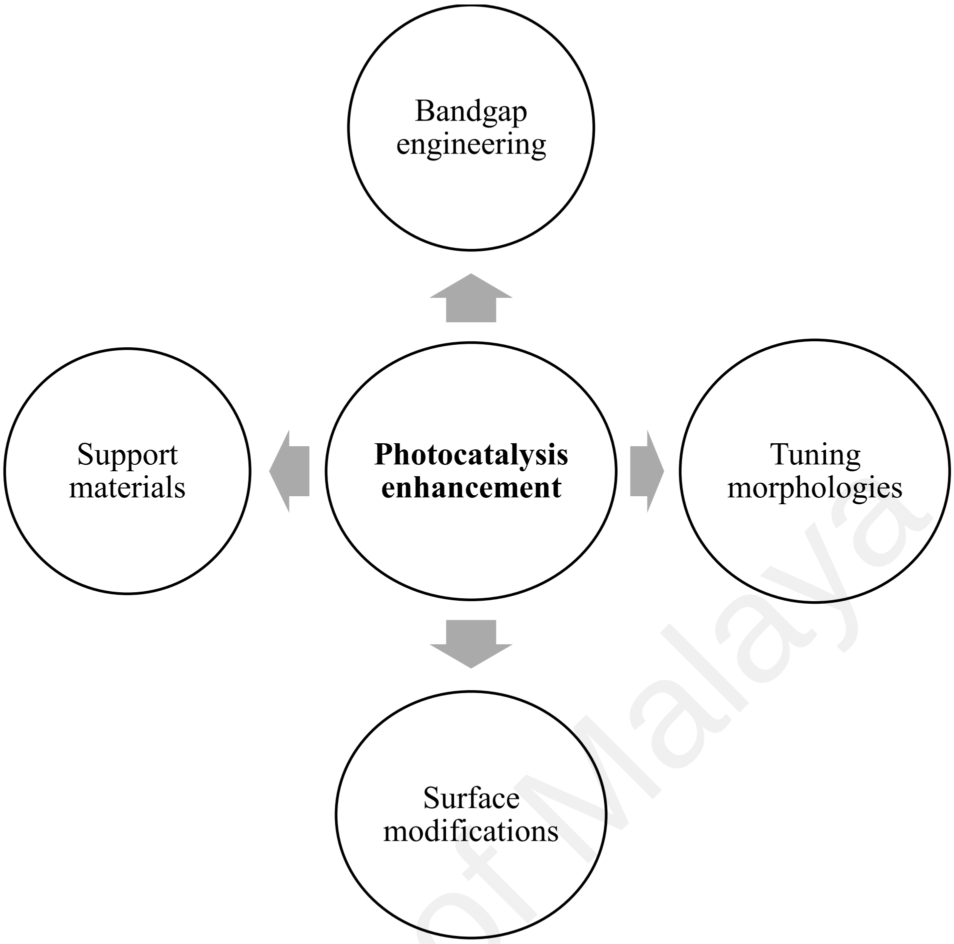

Figure 2.3: Startegies to improve photocatalytic activity.

2.4 Band bending of semiconductors

Difference of Fermi level or redox potential between semiconductors and other substances either in the form of solid, liquid or gas causes the occurrence of an electric charge imbalance which exists between the phase of the two materials after contact. Therefore, these electrical charges will be re-established to achieve a balance in the chemical capability resulting in the formation of an electrical double layer. The charge carrier transfers between the semiconductors and the materials joining them create a space charge region or the depletion layer at the interface which affects the band bending of semiconductor. Band bending in semiconductor affects the separation of charge carriers, recombination and subsequent photocatalytic efficiency of a reaction.

The band bending depends on the material that is joined to the semiconductor either metal/semiconductor, p/n-type, semiconductor/electrolyte, suface state-induced band bending, field effect-induced band bending or adsorption-induced band bending (Zhang & Yates Jr, 2012).

2.4.1 Metal/semiconductor band bending

The properties of metals and semiconductor have been studied by Mott and Schottky about 80 years ago. The charge transfer between them needs to take into account the differences in the work function of the metal (φ_m) and the semiconductor (φ_{sc}) which are related to the change of Fermi level after the combination occurs. If φ_m is greater than φ_{sc}, then the electrons will be transferred from semiconductor to metal. When this happens, the surface of the semiconductor has less positive charges while the metal surface will undergo excessive negative charges which creates a layer called the depletion layer or the space charge region where there is a positive charges surplus in the semiconductor. This condition causes the energy band to curve up towards the interface. If φ_{sc} is greater than φ_m, the electrons will accumulate in the space charge region and electrons transfer will occur from metal to semiconductor so that the energy band will curve downward.

2.4.2 p/n semiconductor band bending

There has been much effort to combine p-type semiconductors with n-type semiconductors such as NiO/ZnO, $CuBi_2O_4/WO_3$, $CaFe_2O_4/AgVO_4$ and Cu_2O/In_2O_3 (Bard, 1979; D‘Arienzo et al., 2011; Morris Hotsenpiller et al., 1998; Zhou et al., 2012). In p/n heterojunction, the Fermi level of p-type semiconductor is lower than that of the n-type semiconductor. Thus, electrons flow from n-type to p-type semiconductor while the hole will flow from p-type to n-type semiconductor. Thus, there is a positive surplus in the n-type semiconductor and negative charge surplus on the p-type semiconductor. As a result, the built-in electric filed is produced near the p/n junction resulting in the energy band of n-type semiconductor bent upward meanwhile the energy band of p-type semiconductor bent downward. This condition indirectly reduces the recombination of photogenerated charge carriers during photocatalysis reactions.

2.4.3 Semiconductor/electrolyte band bending

The redox potential of an electrolyte and Fermi level of a semiconductor play an impotant role in determining the direction of charges transfer. Charge transfers will occur if there is an imbalance of both electrochemical potential of solution (electrolyte) and Fermi level of semiconductor (Bott, 1998). The band bending mechanism for this situation is the same as a metal/semiconductor bending band where it depends on the semiconductor Fermi level and the electrolyte redox potential used. There are four conditions of band bending if the semiconductor is in contact with electrolyte solution namely (i) the formation of a flat band where there is no space charge region is formed and the charge distribution is uniform, (ii) the accumulation layer where the positive charge exists at the interphase while the electrons accumulate in semiconductors near the surface resulting in the density of electrons rising and reducing the density of holes on the surface. This causes the band of semiconductors to bend downward due to the reduction of electron potential energy, (iii) the depletion layer in which the positive charge increases on the surface and the electrons accumulate near the surface. This makes the density of electrons decreases and the density of the positive charge increases on the surface causing the band energy bent upward toward the surface and (iv) the inversion layer where the depletion layer is extent far above the valence band while the Fermi level decreases below the intrinsic level. Surface properties are more to p-type while bulk is more n-type semiconductor. For n-type semiconductor, the positive charge moves towards interphase and undergoes chemical reaction while the negative charge moves towards the bulk of the semiconductor (Barsan & Weimar, 2001; Göpel & Schierbaum, 1995).

2.4.4 Suface state induced band bending

Surface state exists when there is a termination of lattice on the surface of the semiconductor due to the interaction of lone pair electron on the semiconductor surface producing norrow energy band at semiconductor bandgap. For the pure (undoped) semiconductor, Fermi energy level at the surface is similar to the Fermi level energy in the bulk of the semiconductor, hence there is no charge transfer between the bulk and the surface is found, therefore the band is flat. Whereas for n-tpye semiconductor, it shows that the Fermi energy level of the bulk is higher than the Fermi's energy level on the surface and close to the conducting band causing the transfer of electrons from bulk to surface before equilibrium is reached. Here, to achieve the equilibrium, the Fermi level of bulk is decreased and the surface energy level will be increased. After achieving equilibrium, the energy band will be bent over as one move towards the surface. For p-type semiconductor, the Fermi level energy of the bulk is approaching the valence band, which is at a lower level than the surface energy level. Here, the electrons flow from the bulk to the surface causing downword band bending. Generally, the surface state is measured by taking into account the atomic structure for semiconductor surfaces. Different atomic structures even in the same semiconductor still provide different surface state induced band bending (Brillson, 1982).

2.4.5 Field effect induced band bending

Field effect induced band bending exists due to the presence of an external field. Here, assumption is made by assuming $\varphi_m = \varphi_{sc}$ where if there is no voltage is supplied between metal and semiconductor (voltage = 0 V), the energy level is flat. If an external potential is supplied to metals and semiconductors ($V \neq 0$), the electric field will penetrate the semiconductor surface due to low concentration of charge carrier in semiconductor. When a higher voltage is supplied, it will cause electron accumulation near the surface and cause the band bending downword and vice-versa (Ghosh & Raychaudhuri, 2011; Ma et al., 2007).

2.4.6 Adsorption induced band bending

When a molecule approaches the semiconductor surface, the empty molecular orbital reacts with the semiconductor surface resulting in the formation of an internal electrical field and the band bending upward towards the surface of the semiconductor. Whereas for donor molecules, electrons move from molecules to semiconductors and bands bent downward (Zhang & Yates Jr, 2010).

2.5 Preparation of photocatalysts

Since this thesis utilized metal oxide as photocatalysts in chemical reactions, discussions on the preparation of photocatalysts in this section are limited to the preparation of metal oxide-based only by precipitaion. Now, the use of metal oxide has been widely applied to various research branches such as physics, chemistry, materials science and others because of its unique properties and easy preparation methods besides of high stability towards heat, chemicals and environmental effects. Metal oxides that attract interest among researchers are TiO_2, ZnO, CaO, ZrO_2, Al_2O_3, CuO, Fe_2O_3 and WO_3. This is due to the fact that they exhibit semiconductors-like properties which are suitable for catalyst, sensor, fuel cell, solar cells as well as microelectronics. In the preparation of metal oxide, the main course is the strategy to produce nanoparticles that have a small particle size with a large surface area for a chemical reaction. Therefore, methods such as sol-gel, precipitation, hydrothermal, microemulsion, chemical vapor deposition, electrophoretic deposition and others have been studied and used to obtain metal oxides with the desired characteristics. However, this section will only discuss three methods which were used in the production of metal oxides namely precipitation, electrophoretic deposition and aerosol-assisted chemical vapor deposition.

2.5.1 Precipitation method

Metallic oxides and/or mixed-metal oxide can be prepared using precipitation methods. This method is a versatile method because it is simple, economical and environmental friendly as it can be done in aqueous medium at room temperature (Iida et al., 2007). In this method, the formation of a precipitate is due to the presence of physical transformation either by increasing or altering the pH, temperature, concentration, solvent vaporization, the presence of additives and complexing agent. In general, precipitation occurs via two major processes, namely nucleation where the formation of small particles take place followed by the process of growth or agglomeration of particles (Schwarz et al., 1995). The challenge to be dealt with in this method is the kinetic control of the nucleation of particles where the precise control of the above parameters can form monodisperse nanoparticle with narrow size distribution (Burda et al., 2005; Namin et al., 2008).

Precipitation reaction mechanism involves the dissolution of a metal salt in an organic solvent or aqueous solvent followed by the formation of a non-soluble hydroxide metal which can be separated from the solvent by settling down in the reactor base. This metal hydroxide is produced from the reaction between the dissolved metal salt with the addition of basic solution such as NaOH, NH_3 or NH_4OH, urea and Na_2CO_3 (Jadhav et al., 2009; Kalantari et al., 2013; Sadegh et al., 2014). Furthermore, the metal hydroxides formed will besubjected to calcination at high temperature to yield the desired metal oxides.

For example, TiO_2 nanoparticle can be produced from precipitation of $TiCl_4$ with the help of ammonium hydroxide as precipitating agent after reflux for 6 h at 90 ^oC followed by oven dried for overnight at temperature more than 100 ^oC (Namin et al., 2008). In addition, $ZnWO_4$ has also been produced by precipitation method using zinc nitrate hexahydrate, $Zn(NO_3)_2.6H_2O$ and sodium tungstate dihydrate, $Na_2WO_4.2H_2O$ in different solvents and polymeric agents where polypropylene glycol and polyethylene glycol showed the best results (Hosseinpour-Mashkani et al., 2016). In addition to the preparation of single metal oxide, this precipitation method can also be used in the preparation of mixed-metal oxide which is dependent on the solubility of a metal used in the solvent during the reaction (Gupta & Tripathi, 2012). This can be seen from the formation of CuO-NiO-ZnO using a ratio of 1:1:1 of $CuCl_2.2H_2O$, $Ni(NO_3)_2.6H_2O$ and $Zn(NO_3)_2.6H_2O$ in water and ethanol (4:1 ratio) with NaOH as a precipitation agent. The trimetallic oxide can be produced after the conversion of metal hydroxide through calcination at 500 ^oC which produces black colour powder (Juma et al., 2017).

2.5.2 Hydrothermal method

Hydrothermal method is another versatile method to synthesize nanomaterials ranging from metal oxides, metal sulphides, metal nitrides and others. Typically, hydrothermal method is referred to a technique to produce single crystal under high temperature and pressure in a close reactor called autoclave. Several compensations of hydrothermal method can be established for crystal growth technique compared to other technique such as developing crystalline phases which are not stable at the melting point, growing materials with high vapour pressure and suitable for growing good quality of crystals with the controlled composition. However, an expansive autoclave and impossibility of observing the crystal growth inside the autoclave are some of the limitations of hydrothermal method.

Example of photocatalysts that have been synthesized by hydrothermal method is $BiVO_4$. Hydrothermal method enable Fe^{3+} to be doped and substituted in the lattice of $BiVO_4$ producing a flower-like structure in the presence of sodium dodecyl benzene sulfonate (SDBS) as surfactant for degradation of methyl orange where the mole ratio of Fe/Bi of 2.5% showed the highest photocatalytic efficiency as compared to other ratios (Li, Zhang, et al., 2017). Furthermore, the morphology of photocatalysts can be varied by changing the pH of the solution thus further affect the photocatalytic activity of the prepared photocatalyst for any applications. Recently, Bi_2WO_6 nanoplates have been fabricated by changing the pH of the solution using various surfactants such as citric acid, nitric acid, sodium hydroxide and sodium bicarbonate at 180 ^oC for 12 h and tested for the reduction of Cr(IV) (Li, Shi, et al., 2017).

Another study on hydrothermal synthesis was conducted recently by Cheng et al. (Cheng et al., 2018) incorporating metal and non-metal elements namely iron and nitrogen in TiO_2. The material was tested for decomposition of acid orange 7 (AO 7) utilizing titanium isopropoxide ($Ti(OC_4H_9)_4$), iron nitrate nonahydrate ($Fe(NO_3)_3.9H_2O$ and ammonium nitrate (NH_4NO_3) as precursors for TiO_2, Fe and N, repectively. The photocatalytic efficiency reached up to 90% with the optimum dosage of 20 mg/L photocatalsyt after 10 h reaction under visible light irradiation. Meanwhile, nanocubes of WO_3 was successfully obtained at temperature of ranging from 80 - 200 ^oC after 24 h in autoclave by using sodium tungstate dehydrate ($Na_2WO_4.2H_2O$) as a precursor for WO_3 in the absence of any surfactant. The temperature and time of the reaction play significant role in producing nanocubes structure for photocatalytic decomposition of rhodamine B dye (RhB) where temperature of 200 ^oC showed the optimum photocatalytic avtivity of 92.0 % (Wang et al., 2019).

In the case of $Ni(OH)_2$, interconnection with graphitic carbon ($g\text{-}C_3N_4$) has been developed for photocatalytic oxidation of water at 120 ^oC for 12 h using $NiCl_2$ as a precursor for $Ni(OH)_2$ in the absence of any organic agent. The result indicated that 0.5 wt% of $Ni(OH)_2$ gave the optimal apparent quantum yield (AQY) of 1.48% under 405 nm illumination. It was reported that the thickness of $Ni(OH)_2$ can be varied by controlling the concentration of $NiCl_2$ which influenced the photocatalytic efficiency toward water splitting reaction (Yan et al., 2016). Additionally, $Ni(OH)_2$ nanoplates also can be obtained from hydrtothermal method at 200 ^oC utilizing $NiSO_4$ as precursor in the presence of alkaline solution of 7 M NaOH in aqueous medium. The studied showed that, doping $Ni(OH)_2$ with 5% Ce enhanced photodegradation of naproxen, an organic pollutant up to 75% efficiency within 3 h or reaction (Regmi et al., 2018). The effect of organic surfactant such as sodium dodecylbenzenesulfonate (SDBS) in producing $Ni(OH)_2$ nanosheet has been investigated recently in alkaline solution of 0.05 M NaOH and nickel nitrate hexahydrate at 140 ^oC for 24 h. The presence of SDBS in the reaction will aggregate into miclelles which is so-called a soft-template and act as a seed for the growth of $Ni(OH)_2$ (Li & Liu, 2012).

2.6 Thin film fabrication

2.6.1 Electrophoretic deposition method

Electrophoretic deposition method (EPD) is a thin film production technique through the movement of charged particles in suspension by the action of external electrical current over the conductive substrate. Therefore, basic knowledge such as the factors affecting the EPD process such as the particle size, the strength of the supplied power, suspension stability, time of deposition and others are very important in producing high quality deposition. EPD method has been used to deposit numerous nanomaterials such as graphene (González et al., 2018; Ma et al., 2018), carbon nanotubes (Ata et al., 2018;

Haghbin et al., 2018; Qingliang et al., 2018), metal oxides (Argüello et al., 2019; Mohammadi et al., 2018; Morelli et al., 2018), polymer nanocomposites (Baştan et al., 2018; Rehman et al., 2019), biomaterials (Singh et al., 2018; Usmaniya et al., 2019), nanocrystalline multilayer structures and composite laminates (Dzepina et al., 2013; Hadraba et al., 2012). In addition, this technique has been widely used in piezoelectric motors, biomedical ultrasound probes, chemical sensors, and multifunctional and/or bioactive coatings. This technique is also very flexible and versatile because the parameters mentioned above can be varied to obtain the desired morphology and chemical properties such as nanorod, nanotubes, nanowires and nanoflakes (Besra & Liu, 2007; Corni et al., 2008).

There are two methods of deposition to produce thin films by imposing an electric current on the particles in the solution namely EPD and electrolytic deposition. The difference between the two is very significant where the EPD process involves solid suspension while electrolytics involve a salt solution of a substance in the ionic state (Zhitomirsky, 2002). Generally, the fabrication of the thin film by EPD involves two major processes namely electrophoretic reactions of charged particles in the suspension under the applied electric current and the accumulation of the particles on the surface of the conductive substrates (Van der Biest & Vandeperre, 1999). The EPD process is a simple process where it requires only two electrodes regarded as working and counter electrodes connected with the external circuit for the purpose of deposition. The thin film deposition depends on the supply of electrical current during the EPD process that is either direct (D.C) or indirect (A.C). DC-EPD and AC-EPD are generated from direct and indirect electrical current supply, respectively. Since the production of thin films EPD depends on the charge that exists on the particles in the suspension, normally the positively charged particles will be deposited on the cathode and coded as cathodic EPD while the negatively charged particles will be deposited on the anode and called the anodic EPD.

2.6.2 Parameters affect on EPD

One of the main factors affecting the EPD process is the size of the particles. However, there is no resolution to the optimum particle size that should be used to obtain a quality deposition. Heavens et al. (Heavens, 1990) has reported that a good deposition should have a particle size between 1 - 20 µm, but the size of particles that are outside the range can still undergo the deposition. EPD deposition of a substance can only be performed if there is a charged particle movement in the suspension on the substrate surface. The ability of a particle to move in suspension and remain suspended must be higher than its rate of the suspension to settle down. This is because for large particles, they are more likely to settle down and when this happens, the resulting film is uneven where the upper part becomes thicker than the bottom when the substrate is placed vertically. However, large particle deposition can be performed when higher voltage is used. In addition, the probability of cracking on the deposited film is higher than that of smaller sized particles. This condition has been studied on $YBa_2Cu_3O_{7-x}$ where the film produced from small particles can provide a uniform morphology and crack can be reduced (Sato et al., 2001).

In general, the conductivity of a solution will increase when the dielectric constant of a solution is increased. This situation is evident from Powers' observations (Powers, 1975) on the deposition of β-alumina in some organic solvents and he found that EPD can be produced in solvents having a dielectric constant between 12 - 25. If the dielectric constant of a solvent is high than the concentration of the ionic species in the solution will be enhanced and this can decrease the double layer region and electrophoretic mobility. Therefore, deposition by using EPD must ensure take into account the concentration of ionic species in the appropriate solution and dielectric constant of the solvent used. In addition, the conductivity of suspension is also a measure of the effectiveness of the deposition using the EPD technique (Ferrari & Moreno, 1997). This is because suspensions that have a very high conductivity will cause the movement of the particles slowly and vice versa. Suspension viscosity is another factor that should also be taken into account in the EPD process. One way to measure suspension viscosity is through rheology measurements. However, in the EPD process, solid content in the solution are very low and it is impossible to measure the viscosity level of the suspension. However, a good suspension for the EPD process must have a high dielectric constant, low conductivity and low viscosity (Ferrari & Moreno, 1997). The value shown by Zeta potential, ξ is another factor to be emphasized in the EPD process where Zeta potential provides information on suspension stability by measuring the strength of the interaction between the particles in the suspension, the density of the deposit and the direction and speed of the charged species during the EPD process. Zeta potential strongly influenced by factors such as solid loading, acidity and basicity of the suspension as well as solvent concentration used which affects the density of the resulting deposit. In the EPD, there are two forces that affect suspension stability namely the attractive forces and Van der Waals forces. The coagulation that occurred during the EPD process has to do with both of the forces. If the electrostatic repulsion of the particles in the suspension is due to the large particle charge, then the coagulation can be avoided thus producing a high density deposit. If the particle charge in the suspension is low, then the agglomeration process will occur and form a porous deposit. Therefore, the charge in the particles plays a very important role in determining the quality of the deposit that will result from the EPD process (Chen et al., 1999; Krueger et al., 2004; Wang et al., 1997).

To obtain a good deposition by the EPD method, the suspension formed must be stable. Suspension stability is determined by the size of particles dispersed into the solution. Stable suspension contains particles which are capable of continuously being suspended for a long period of time with slow precipitation rate. This can be observed on particles of less than or equal to 1 μm. Such a situation occurs due to the Brownian movement of the particles. However, the particle size which is greater than 1 μm tends to settle down quickly and unable to stay in a suspended state for a long period of time. This causes the coagulation process to easily occur if the particle size is large.

Some researchers found that at a constant voltage, the rate of deposition decreased when the deposition time increased (Basu et al., 2001; Wang et al., 2004). This situation is very different at the beginning of the deposition process where the deposition rate increases linearly with deposition time. However, the deposition rate becomes a plateau after a certain period of time due to the formation of insulating layer of ceramic paricles on the surface of the electrode (Zhitomirsky & Gal-Or, 1997). In addition to the deposition time, the voltage supply also affects the EPD process. Typically, the amount of material that can be deposited will increase at high voltage. This is because the suspended particles can move faster under high voltage, but thin films produced have low quality. One report states that the EPD method can be done well if it uses a voltage between 25 - 100 mV/s while films produced using a voltage exceeding 100 mV/s have low quality (Basu et al., 2001).

This is because, at high voltage, suspended particles move faster so they do not have time to find a suitable place on the surface of the substrate to produce a close packed structure. In addition, for the deposition of multicomponent system with EPD technique, the solid concentration in the suspension is very important. The different solid concentration in suspension causes them to deposit at different rates depending on the volume fraction of the solid in the suspension. If the volume fraction of solid is high then they will be deposited at the same rate, but if their volume fraction is low then the deposition will take effect at the individual deposition rate. In addition, conductivity of substrate also affects the deposition and quality of the resulting material (Peng & Liu, 2001). For example, the low conductivity of the $La_{0.9}Sr_{0.1}MnO_3$ substrate causes the resulting film to be less uniform results from a slow deposition rate. The same situation is also noted by Chen et al. (Chen & Liu, 2001) on the substrate conductivity of $La_{0.9}Sr_{0.1}MnO_3$. They found that the conductivity of the $La_{0.9}Sr_{0.1}MnO_3$ substrate increased after performing the calcination process at 700 °C for 30 minutes when the organic binder decomposes and produces a good yttrium-stabilized zirconia (YSZ) film.

2.6.3 Type of EPD medium

A quality thin film fabricated from EPD process must ensure that the suspension is stable, unagglomerated and homogeneous including the reaction medium whether in aqueous or non-aqueous medium. The obstacles in organic solvents such as the supplied voltage is lower besides of suffering from the economic and environmental perspectives can be overcome with the use of aqueous solvents (Chen & Liu, 2001). However, there are some weaknesses in the use of aqueous solvent such as electrochemical reactions that occur on the surface of the electrode which is the release of gas as a result of the water electrolysis reaction. The gas released from water electrolysis is usually trapped in the deposits and reduces the quality of the deposit generated by creating crack on the deposit surface, Joule heating of the suspension and oxidation of the metal electrode which causes the dissolution of metal into the suspension which is also deposited as heterogeneity or residual entities on the substrate (Moreno & Ferrari, 2000).

The use of organic solvents in the EPD process can solve the problems encountered in the application of aqueous solvent as described above. However, organic solvents have a low dielectric constant, resulting in the low production of ionic species in the suspension due to the low ionization power found in organic solvents. Therefore, the voltage to be supplied should be high to allow the process of deposition to occur and to move the suspended particles towards the substrate on the electrode. Commonly used organic solvents are ketones and bezene which have high redox potential. The production of protons in organic solvents can be seen from the reaction between ketone and iodine according to the equation below (Ishihara et al., 1996; Mathews et al., 2000):

$CH_3\text{-}CO\text{-}CH_3 + I_2 \rightarrow I\text{-}CH_2\text{-}CO\text{-}CH_2\text{-}I + 2H^+ + 2I^-$ (2.3)

$CH_3\text{-}CO\text{-}CH_2\text{-}CO\text{-}CH_3 + I_2 \rightarrow I\text{-}CH_2\text{-}CO\text{-}CO\text{-}CH_2\text{-}I + 2H^+ + 2I^-$ (2.4)

The adsorption of the protons on the suspended particles surface makes them positively charged and if the DC current is supplied, these positively charged particles will move towards the cathode and deposited on the cathode. **Table 2.2** below represents the implementation of electrophoretic deposition method to deposit some nanoparticles.

Table 2.2 Applications of electrophoretic deposition.

Materials	**Deposition medium**	**Applied voltage (V)**	**Deposition time (min)**	**Applications**	**References**
Chitosan-copper	Water:ethanol (20:80 v/v)	20	5	Anticorrosion	(Tabesh et al., 2019)
Ni/Yttria stabilized zirconia	Acetone	35	30	Superalloy	(Alavi et al., 2019)
$PbMoO_4$	Isopropanol	12	30	Photocatalyst	(Obregón et al., 2018)
$SrTiO_3$	Aqueous	40	2	Photocatalyst	(Phoon et al., 2018)
ZnO/chitosan/ bioactive glass	Ethanol:water:acetic acid (79:20:1 v/v)	25	1	Antibacterial	(Karbowniczek et al., 2017)
NiO/nongraphitic flake	Isopropanol	100	3 - 6	Ethanol electrooxidation	(Daryakenari et al., 2017)
$CaBiVMoO_8$	Isopropanol	12	30	Photocatalyst	(Vázquez et al., 2020)
Polymethylmethacrylate (PMMA)-Al_2O_3	Ethanol:water (85:15 v/v)	3	30	Biomedical	(D'Elia et al., 2020)
Co_3O_4/nongraphitic flake	Acetone + I_2	25	2.5	Li-ion battery	(Keshmarzi et al., 2019)
CdSe/TiO_2	Chloroform	150	80	Quantum Dot Sensitized Solar Cell	(Kyaw et al., 2019)
rGO/TiO_2	Aqueous	4 (TiO_2); 10 (rGO)	30s	Dye sensitized solar cell	(Peiris et al., 2018)
TiO_2 (anatase, rutile, P25, UV 100)	Ethanol+isopropanol+acetone+tetrahydrofuran+heptane.	300	10	Photocatalyst	(Zouzelka et al., 2018)
TiO_2	Aqueous	5	10	Dye sensitized solar cell	(Marandi et al., 2015)
Chitosan/TiO_2/bioglass	Aqueous	0.5 – 2.5	0 - 600	Bioimplants	(Clavijo et al., 2016)
TiO_2/Cu_2O	Aqueous	10 – 30	1 - 3	Solar cell	(Ichimura & Kato, 2013)

Table 2.2, continued.

MWCNT/TiO_2/Co	Acetyl acetone + acetone + ethanol	80	5	H_2 storage	(Bordbar et al., 2015)
rGO/RuO_2	Aqueous	4	8.3	Supercapacitor	(Amir et al., 2016)
$Ni(OH)_2$	EtOH:Water (19:1 v/v)	57 – 71	0 – 15	Pseudo-capacitor	(Gonzalez et al., 2017)
$Ni(OH)_2$/YSZ and NiO/YSZ	Acetylacetone	25	1	Electrochemical device	(Salehzadeh et al., 2019)
Co_3O_4	Acetylacetone: ethanol (1:1v/v)	100 – 150	1 – 30	Electrochemical device and catalyst	(Zhang et al., 2014)
$Fe_2O_3/Mn_{1.5}Co_{1.5}O_4$	Ethanol:water (60:40 v/v)	50	20	Solid oxide fuel cell	(Zanchi et al., 2019)
Hydroxyapatite/Fe_2O_3/ chitosan on Ti/13Nb/13Zr alloy	Ethanol: chitosan (70:30 v/v)	15	6	Biomedical	(Singh et al., 2020)
RGO/NiO	EtOH: H_2O (19:1 v/v)	200	15s	Electrochemical device	(Yus et al., 2019)
CuO/ZnO	Isopropanol	40	7	Microbial fuel cell	(Khajeh et al., 2020)
ZnO	Methanol	10	10	Photocatalyst	(Taheri et al., 2018)
$LiFePO_4$	Ethanol:water (30:70 v/v)	10 – 50	3 – 10	Li ion battery	(Michaud et al., 2019)
Gelatin/chitosan	Ethanol:water	10 – 50	3 – 5	Drug delivery	(Heise et al., 2019)
$Ba_{0.5}Sr_{0.5}Co_{0.8}Fe_{0.2}O_{3-\delta}$	Ethanol	150	10	Oxygen separation	(Ishii et al., 2019)

2.6.4 Mechanism of EPD

Generally, in the EPD technique, after the electric field is applied, the suspension particles will move towards the electrodes depending on the particle charge. However, the mechanisms that occur in the EPD process are sophisticated although there are some recommendations in the literatures. Among them, the EPD process occurs through flocculation of particle where the deposition process is equal to the sediment formation caused by gravity action. The supplied electrical field is used to move the charged particles to the electrode to be deposited. The pressure imposed by the particles is sufficient to overcome the interparticle repulsion in order to be deposited. This method is suitable for depositing material on the porous membrane (Besra & Liu, 2007).

The second mechanism is through neutralization of charged particles. This mechanism suggests that the particles will be neutralized when in contact with the electrode and will become stiff or static. This mechanism is very important for the single and monolayer deposition. However, it is valid for a diluted suspension and invalid for long-term EPD, when particles-electrode is prevented as in the semi-permeable membrane induced deposition where the reaction that occurs in the electrode involves changes in pH (Besra & Liu, 2007).

The third mechanism is called the electrochemical particle coagulation mechanism where it involves the decline in the force of repulsion between particles due to an increase in the electrolyte concentration near the electrode. This makes the zeta potential low and causes flocculation of particles to occur which leads to the deposition of a substance. However, this mechanism is useful when the electrode reaction produces OH- as an example in a suspension containing water and can not be applied if no increment in electrolyte concentration near the electrode (Besra & Liu, 2007).

Problems arising when the absence of the increment in electrolyte concentrations near the electrode attracted interest in Sarkar et al. (Sarkar & Nicholson, 1996) in explaining new mechanisms involving the movement of positively charged metal oxide towards the cathode in the EPD which is called the electrical double layer distortion and the thinning mechanism. When the lyosphere which is referred to the counter ions around the charged particles are moved, the electric field and the fluid dynamic will be distorted. The cation in the suspension and the positively charged particles are also moving towards the cathode. Therefore, the anions in the solution tend to react with cation causing the double layer to be thinner to allow the incoming particles with enough Van der Waals (VDW) interaction to form coagulation or deposited. The distortion of double layers provides an opportunity for the formation of coagulation of particles near the electrode.

2.7 Photoelectrochemical (PEC) studies

Photoelectrochemical studies can be regard as the improvement to the photocatalytic reaction where the reduction and oxidation reaction occurs on the surface of the electrode which is cited as a cathode and anode in the presence of an external electric field compared to the photocatalysis process where the redox reaction occurs on the single semiconductor particle or aggregate which can increase the probability of charge carrier recombinations. The most important requirement in the implementation of PEC studies is the immobilization of semiconductor or molecular photocatalysts on the conductive substrate which allow the modification of the Fermi level of the respective photocatalysts. In addition, quantum efficiency for photocatalytic reaction uses the photocatalytic reaction ratio in the unit elementary charge and the flux of the incident photons, whereas for PEC reaction, quantum efficiency will increase with an increase in electric field that allows the spatial separation of photogenerated charge carriers. However, the discussion of PEC studies in this thesis only focuses on the oxidation of methanol, oxidation of water and the reduction of CO_2 gas using semiconductor photocatalysts.

2.7.1 Methanol oxidation

What is important in the DMFC is the assembly of the electrodes, anode and cathode with a polymer exchange membrane (PEM) either in acidic or alkaline conditions. Conventionally, the anode consists of the PtRu catalyst and the cathode is Pt/C attached to the membrane which is normally a gas diffusion electrode (GDL) which plays a role in providing support for reactant distribution, current collection and catalysts layer protection. In general, methanol and water mixtures will be passed to the anode and oxidized to CO_2 gas by removing the electrons to the external circuit while the protons will be diffused through GDL to the cathode where the supplied oxygen reacts with the protons and electrons from the oxidation reaction of methanol to produce water. The Equation (2.5 – 2.10) below shows the reaction that occurs in acidic and alkaline conditions (Joghee et al., 2015).

In acidic condition,

Anode: $CH_3OH + H_2O \rightarrow CO_2 + 6H^+ + 6e^-$ (2.5)

Cathode: $3/2O_2 + 6H^+ + 6e- \rightarrow 3\ H_2O$ (2.6)

Overall reaction: $CH_3OH + 3/2O_2 \rightarrow CO_2 + 2H_2O$ (2.7)

In alkaline condition,

Anode: $CH_3OH + 6OH^- \rightarrow CO_2 + 5H_2O + 6e^-$ (2.8)

Cathode: $3/2\ O_2 + 3H_2O + 6e^- \rightarrow 6OH^-$ (2.9)

Overall reaction: $CH_3OH + 3/2O_2 \rightarrow CO_2 + 2H_2O$ (2.10)

DMFC can be said to be eco-friendly because they do not release toxic substances into atmosphere. Reactions between CO_2 and released water as a by-product can be recycled to methanol or produce other organic substances such as ethanol, formic acid and so on. Development of fuel cells could be applied in transportation, portable equipment and microfuel cells. This is because fuel cell can replace a combustion engine that involves a lot of power loss especially in thermal engines and generators. It can also replace the battery as a vehicle's power source and reduce the weight and space in the manufacturing of electronic and portable devices.

In addition to the advantages that exist, DMFC also has its own weakness which is slow kinetic electro-oxidation. During the oxidation process of methanol, CO will be produced as a intermediate species before being oxidized to CO_2. In addition to the formation of CO, other species such as HCO, COH and HCOO are also generated. However, there are some of intermediate species are difficult to be oxidized, thus remain adsorbed on the catalyst surface and inhibit other methanol molecules to be adsorbed on the surface of the catalyst and oxidized. Therefore, the oxidation process of intermediate species is very important since it measures the overall rate of oxidation reaction of methanol. Furthermore, desorption of this intermediate species without the complete oxidation to CO_2 will further reduces fuel cell efficiency.

Additionally, the presence of methanol crossover also reduces DMFC efficiency. The main objective of using membrane in fuel cell or DMFC is to prevent fuel and oxygen from reaching the electrode at the opposite side. In the case of DMFC, due to the high hydrophilic nature of the OH functional group of methanol, the methanol molecule will be carried by hydronium ion and interacts with ion exchange sites on the PEM used. In addition, methanol's ability to react directly with the supplied oxygen gas at the cathode in the presence of electrons further lowered DMFC's performance as well as creating internal shortcuts and losses of current (Sajgure et al., 2016).

Meanwhile, by hybridizing Pt with semiconductor photocatalyst such as TiO_2 could be able to enhance the efficiency of DMFC under the irradiation of UV-Vis light. Thus, generating a novel type of DMFC namely photoassited direct methanol fuel cell or photo-oxidation of methanol (He et al., 2013; Zhu et al., 2016) by converting the chemical energy and the abundance solar energy into electrical energy. However, before the development of photoassisted methanol oxidation, it is generally known that TiO_2 has been used as support and/or additive for methanol oxidation reaction in dark conditions in Pt-based catalyst (Antolini, 2010; Antolini & Gonzalez, 2009; Lv & Mu, 2014).

Some transition metal oxides such as TiO_2, SnO_2 and WO_3 have been reported as suitable cocatalysts since they can reduce the severe poisoning effect of Pt by removing the methanol oxidation reaction intermediates from the catalyst suface (Antolini & Gonzalez, 2009). Among the ceramic oxides mentioned above, TiO_2 is widely used as catalyst support and/or cocatalyst due its execellent photocorrosion properties in various electrolytic media (Diebold, 2003). However, low surface area and poor electrical conductivity of TiO_2 are the major factors that decrease the efficiency of DMFC. Thus, carbonaceous nanomaterials such as carbon black, CNT and graphene (Su et al., 2017) are sometimes used as support materials in some studies in order to improve the performance of TiO_2-based DMFC. The formation of nanotubes and nanowires of TiO_2 also have been suggested to increase the efficiency of DMFC due to enhancement of TiO_2 surface area (Abida et al., 2011; Sui et al., 2014).

On top of that, the incorporation or doping TiO_2 with metal ions such as Fe^{3+}, Cr^{3+}, Ru^{3+}, Ce^{4+}, Cu^{2+}, Mn^{2+} and Co^{2+}, non-metals such as N,C, B, F and noble metals such as Ag and Au are reported to be successfully increase the visible light absorption of TiO_2 which lead to the improvement of DMFC performance (Fujishima et al., 2008; Kolobov et al., 2017; Nguyen et al., 2015; Schneider et al., 2014). Besides that, the effectiveness of methanol oxidation reaction has also been compared between anatase and rutile TiO_2 of different facet. It is found that single crystal anatase with (101) facet is more active than single crystal rutile with (001), (100) and (110) surface which lead to higher photocatalytic activity (Ahmed et al., 2011) due to ineffective holes in rutile as compared to anatase TiO_2 to drive efficient and irreversible methanol oxidation reaction (Wang et al., 2015). It is suggested that the C-H bond in methanol is cleaved first on anatase forming $^{\bullet}CH_2OH$ radicals whereas, in rutile methanol has to be adsorbed first on the surface of rutile before the cleavage of C-H bond can take place which make the oxidation reaction on anatase is kinetically more faster than rutile (Sfaelou & Lianos, 2016).

Upon light irradiation onto the surface of TiO_2, electrons with sufficient energy to overcome the band gap energy of TiO_2 will be promoted from the valence band to conduction band leaving the positive holes to remain in the valence band to assist the oxidation reaction to take place (Fujishima et al., 2008). Then, hydroxyl radicals, $OH^{\bullet}$ are generated by the oxidation reaction of water and/or hydroxide ions, OH^- with the remaining holes in the valence band on the surface of TiO_2. At this stage, two types of methanol oxidation reaction takes place namely direct and indirect oxidation reaction accoding to Park et al. (Park et al., 2007) and Villareal et al. (Villarreal et al., 2004), respectively. For direct methanol oxidation reaction, methoxide ion react with holes to form methoxy radical which undergoes further reaction to form formaldehyde. Whereas, for indirect methanol oxidation reaction, with the aid of $OH^{\bullet}$ radicals, C-H bond of methanol cleaved to form methoxy radical and water before producing formaldehyde at the end of the reaction. The following equation summarized the methanol oxidation reaction processes.

$TiO_2 + h\upsilon \rightarrow e^- + h^+$ (2.11)

$h^+ + H_2O \rightarrow OH^{\bullet} + H^+$ (2.12)

$h^+ + OH^- \rightarrow OH^{\bullet}$ (2.13)

Direct methanol oxidation reaction

$CH_3O^- + h^+ \rightarrow CH_3O\bullet$ (2.14)

$CH_3O^{\bullet} \rightarrow HCHO + H^+ + e^-$ (2.15)

Indirect methanol oxidation reaction

$CH_3OH + OH^{\bullet} \rightarrow CH_2OH^{\bullet} + H_2O$ (2.16)

$CH_2OH^{\bullet} \rightarrow HCHO + H^+ + e^-$ (2.17)

In another study conducted by Shen et al. (Shen & Henderson, 2011), they suggested that surface adsorbed methoxy species is the more reactive species than surface adsorbed methanol which photodecomposes into formaldehyde through the cleavage of C-H bond. Thus, they proposed that methoxy radicals species is a good hole scavenger in methanol oxidation reaction. To summarize based on their work, the pathway for methanol oxidation reaction is through the surface adsorption of methanol onto TiO_2 followed by the dissociative reaction of methanol leading to the formation of methoxy groups. The advantages of the methoxy group is the negative charge on methoxy species induced band bending near-surface region which split the photgenerated electron-hole pairs, minimizing charge recombination effect and fascilitating hole migration towards the surface for the oxidation reaction to take place (Panayotov et al., 2012; Setvin et al., 2017).

Apart from gold, platinum and palladium, the photocatalytic activity of TiO_2 can also be enhanced by metals such as ruthenium. RuO_2 is one of the transition metal oxides with a rutile-like structure, possesses a variety of attractive features such as high chemical stability, high electrical conductivity and diffusion barrier properties. Therefore, RuO_2 has been used in various applications such as supercapacitors, electrolytic generation of chlorine (Trasatti, 1991), water oxidation (Mills et al., 2010), CO oxidation in sensors (Reuter & Scheffler, 2006), methanation of CO_2 (Abe et al., 2009) and HCl oxidation (Mondelli et al., 2011). Sakata et al. (Sakata et al., 1984) reported that the incorporation of small amounts of RuO_2 on the surface of TiO_2 effectively separates the photogenerated electrons and holes. However, excessive amounts of RuO_2 may function as recombination centres for the charge carriers. Polymeric precursor method has been employed to develop Pt-Ru-TiO_2/C for methanol oxidation showed that an improvement in anodic current up to 18% in light as compared to dark condition where 20% TiO_2, 5% Pt and 5% Ru showed the best performance for oxidation of alcohol. The existence of synergistic effect between photo- and electrocatalyst is believed to be the main factor of high efficiency in methanol oxidation reaction (Polo et al., 2011).

Meanwhile, cobalt oxide such as Co_3O_4 is p-type semiconductor with excellent electronic and magnetic properties which has various applications as photocatalysts (Ishimaki et al., 2017), high temperature solar selective absorbers (Barrera et al., 1998) and pigment for glasses and ceramics. It is often regarded as the most versatile oxides among the first row transitions metal oxides (Patil et al., 1996). On the other hand, manganese oxide (MnO_2) is widely used as photocatalysts, electrodes in batteries and supercapacitors. This is due to the unique properties of MnO_2 such as low band gap, high natural abundance, multiple oxidation states and excellent electrochemical properties (Yu et al., 2016). Fabricating a heterojunction of MnO_2 with other traditional photocatalyst such as TiO_2 improves the photocatalytic activity. This is due to the capture and retention of photogenerated electrons and holes by the MnO_2, thus inhibiting their recombination. Xu et al. (Xu et al., 2014) reported that the electrons and holes can be released due to the higher conductivity of MnO_2, thus creating an open circuit nanoscale battery between the MnO_2 and TiO_2. This effect further enhances the photocatalytic activity in the visible region. Moreover, the photocatalytic activity of the RGO/TiO_2 composite was significantly enhanced when doped with MnO_2, due to the lower charge transfer resistance of MnO_2 (Cao et al., 2015).

Additionally, electrochemical oxidation of ethanol over cadmium doped cobalt supported carbon nanoparticle in 1 M KOH has been synthesized by using sol-gel method showed high current density of 70 mA cm^{-2} with low onset potential of ~585 mV vs normal hydrogen electrode (NHE) (Barakat et al., 2013). Other example of oxidation of organic substance can be observed from the degradation reaction of benzyl alcohol over Co_3O_4 supported with various support reached the conversion up to 90% after 6 h (Cordoba et al., 2017). The used of Co_3O_4 in dehydrogenation of alcohol due to the Co_3O_4 can provide Lewis acid sites for the reaction to proceed (Zhu et al., 2011).

Apart from Co_3O_4 and RuO_2, MnO_2 has widely been used on electrochemical oxidation of alcohol. It has been reported that, MnO_2 is possesses proton-electron intercalation which is expected to show excellent electrochemical performance under various operating conditions (Rebello et al., 2006; Zhao & Li, 2008; Zhao et al., 2010). Furthermore, due to existence of Mn^{3+}/Mn^{4+} redox couple and labile oxygen, enable MnO_2 to promote excellent antipoisoning activities for alcohol electrooxidation (Meher & Rao, 2013). Additionally, electrochemical oxidation of alcohol also is affected by structure of the prepared catalyst. For example, one dimensional (1D) structures suh as nanorod, naotubes and nanowires possesses distinctive crystalline phase state, nonlinear optical properties and quantum size effects as compared to their bulk counterparts (Patzke et al., 2011). Besides, the interaction between metal crystallites and an oxide surface were influenced by the nature of interfacial contact and crystalline characteristic of the oxide. Smaller size MnO_2 with uniform cryatllite structure tend to provide active sites for the interaction with Pt which optimized the synergistic effect for electrochemical oxidation of alcohol (Boucher et al., 2011; Li et al., 2012). Furthermore, introduction of conducting polymer and reduced graphene oxide over MnO_2 is reported to further enhance the oxidation of methanol for direct methanol fuel cell. For example, PEDOT:PSS/MnO_2/rGO has been prepared by using hydrothermal and oxidative polymerization method showed that the anodic, cathodic electron transfer coefficient and heterogeneous rate constant for electrocatalytic oxidation of methanol were 0.51, 0.45 and 0.055 s^{-1}, respectively with the current density as high as 56.38 mA/cm^2 and lower onset potential (0.32 V). The synergistic effects of excellent conductivity of rGO and PEDOT:PSS coated on MnO_2 nanorods was the main contribution for the outstanding performance of the material (Baruah & Kumar, 2018). Some recent studies related to the oxidation of methanol were tabulated in **Table 2.3** below.

Table 2.3 Catalysts for methanol oxidation.

Catalysts (Working electrode/Anode)	**Synthetic method**	**Counter electrode (Cathode)**	**Electrolyte**	**Current density (mA/cm^2)**	**References**
B/N/Pt/graphene aerogel	Microwave	Pt wire	0.5 M H_2SO_4 + 0.5 M CH_3OH	~19	(Çögenli & Yurtcan, 2020)
Pd/Co@CoO-rGO	Hydrothermal	Pd foil	0.5 M KOH + 2 M CH_3OH	1786 mA/mg (mass activity)	(He et al., 2019)
Cu_2O/PPy/GO	Reduction of borohydride	Pt wire	0.05 M H_2SO_4 + 2 M CH_3OH	155	(Pattanayak et al., 2018)
Nickel foam/ Co_3O_4/$NiCo_2O_4$	Hydrothermal	Pt	1 M KOH + 0.5 M CH_3OH	140	(Qian et al., 2020)
Pt/N-Vulcan carbon	Hot injection	Graphite rod	0.1 M $HClO_4$ + 0.5 M CH_3OH	3.25	(Yoo et al., 2020)
CeO_2/NiO	Hydrothermal	Pt foil	1.0 M KOH + 1.0 M CH_3OH	140	(Li, Song, et al., 2020)
Cu-Pt/C	Hydrothermal	Graphite rod	0.5 M H_2SO_4 + 0.5 M CH_3OH	N/A	(Long et al., 2020)
Pt_xPd_{1-x} alloys	Ligand displacement	Pt mesh	1.0 M KOH + 1.0 M CH_3OH	64 mA/mg	(De la Cruz-Cruz et al., 2020)
CuO/Ni foam	Electrodeposition	Pt wire	1 M KOH + 0.5 M CH_3OH	80	(Roy et al., 2019)
Pt/graphene	Chemical vapour deposition (CVD)	Pt plate	1 M NaOH + 1 M CH_3OH	939 mA/mg	(Berghian-Grosan et al., 2020)
$ZnCo_2O_4$	Microwave	Pt	1 M KOH + 0.5 – 4 M CH_3OH	223.3	(Sreekanth et al., 2019)
Ni/NiO/MWCNT	Combustion	Pt	0.1 M KOH + 0.05 – 0.7 M CH_3OH	15.94	(Askari et al., 2019)
NiO-MOF/rGO	Hydrothermal	Pt wire	1 M NaOH + 3 M CH_3OH	275.85	(Noor et al., 2019)
TiO2/ZnO/Pt	Electrodeposition	Pt wire	0.1 M NaOH + 0.5 M CH_3OH	6	(Özdokur et al., 2018)

Table 2.3, continued.

Pt/1-D TiO_2	Hydrothermal	Pt plate	1.0 M KOH + 1.0 M CH_3OH	5.32 mA mg^{-1}	(Hu et al., 2017)
TiO_2-SnO_2/SO_4^{2-}	Sol-gel and thermal decomposition	Pt wire	0.5 M NaOH + 0.5 M CH_3OH	1.5	(Li et al., 2019)
Pt/TiO_2	Atomic layer deposition	Pt wire	1 M H_2SO_4 + 1 M CH_3OH	74	(Anitha et al., 2018)
CuI/TiO_2	Hydrothermal	Pt wire	1.0 M KOH + 1.0 M CH_3OH	3772 mA mg^{-1}	(Sun et al., 2017)
5,10,15,20-tetrakis(4-carboxylphenyl)porphyrin/ NiCo-LDH	Hydrothermal	Pt foil	1 M KOH + 1 M CH_3OH	34.9	(Yang et al., 2020)
Au/fullerene-C_{60}	One-pot electrochemical	Pt wire	1 M NaOH + 1 M CH_3OH	98 m^2 g^{-1}	(Bhavani et al., 2019)

2.7.2 CO_2 reduction

Environmental care tasks to ensure the survival of future generations due to the climate change because of increasing CO_2 gas emissions into atmosphere lately has been the primary responsibility of all parties. Factors such as the increase in world population, full dependence on natural fuels as a source of energy as well as the improvement of the global economy have been a major contributor to global climate change. Therefore, a drastic step utilizing the emitted CO_2 as a carbon source for the production of carbon-based chemicals should be implemented. The use of either homogeneous or heterogeneous catalysts has played a very important role in many CO_2 utilization routes such as photocatalysis, electrocatalysis and photoelectrocatalysis in mitigating the problems encountered in relation to environmental pollution and energy sources.

Harvesting electromagnetic radiation can be done by using semiconductor photocatalysis. Once the electromagnetic radiation is absorbed, the electron in the valance band will be excited to the conduction band if it has the energy larger than that of the band gap of semiconductor leaving the positive charge particles called holes to be remained in the valence band. The resulting photogenerated charge will be migrated to the surface or captured in the trapped sites or recombine on the surface or in the semiconductor. Effective photoreaction should successfully diffuse and transfer the photogenerated electrons and holes to reach the adsorbed species on the surface of photocatalysts to facilitate the redox reaction (Linsebigler et al., 1995).

Numerous innovative systems found in literatures on homogeneous and heterogeneous photocatalysts have been used for the purpose of CO_2 reduction reactions such as supramolecular, enzymatic, composites heterogeneous photocatalysts and many more. Among homogeneous molecular photocatalysis, transition metals complex of Re and Ru diimine carbonyl, Ni and Co complex tetraazamacrocycles and Fe and Co porphyrins had attracted much attention (Cokoja et al., 2011; Eisenberg & Hendriksen, 1979; Gibson, 1999; Morris et al., 2009). Tricarbonyl Re(I) diimine complex of Re(bpy)$(CO)_3$Cl is widely used in CO_2 reduction reaction had led to the formation of CO with quantum efficiency of 0.59 (Hawecker et al., 1983; Takeda et al., 2008; Takeda et al., 2011). Diimie and metalloporphyrin complex photocatalysts are more favorable for CO_2 reduction reaction is due to their ability to harvest more light while Ni and Co complex tetraazamacrocyclics require photosensitizer such as $Ru(bpy)_3^{2+}$ (bpy: bipyridine) to absorb light. Typically, homogeneous photocatalysis in the reduction of CO_2 reaction occur by promoting CO_2 molecule after the absorption of light (Fisher & Eisenberg, 1980; Fujita et al., 1991; Kimura et al., 1993; Matsuoka et al., 1993; Shionoya et al., 1990).The energy gained by CO_2 from the light irradiation facilitate the molecule to the excited state which then quenched by electron transfer from the sacrificial electron donors such as triethylamine and triethanolamine. Normally, the products formed in the presence of sacrificial agent such as the same tertiary amine or water is formic acid and CO. The insertion of CO_2 into the reduced metal center is the most important step in homogeneous photocatalysis. For example, incorporation of CO_2 molecule into Re(bpy)$(CO)_3$Cl complex produces formate (Morris et al., 2009).

However, electron transfer from photosensitizer of $Ru(bpy)_3^{2+}$ to photocatalyst is sometimes insufficient. Therefore, heteronuclear supramoleular photocatalyst has been disintegrated and used to enhance the absorption of visible light where the photosensitizer is linked directly with the photocatalyst (Grills & Fujita, 2010; Rau et al., 2007; Schulz et al., 2012; Takeda & Ishitani, 2010). The ability of polypyridyl Ru(II) to absorb light makes it suitable candidate as photosensitizer and this can be seen when it is used together with Ni(II) cyclam catalyst by Komura and his co-workers (Chiorboli et al., 2005). The existence of bonds between polypyridyl Ru(II)-Ni(II) cyclam add to the stability of the complex as well as enhancing photocatalytic activity towards CO_2 reduction reactions. They also found that the selection of bridging ligand affects the catalytic activity of the supramolecular system in which the alkylation of the nitrogen atom of cyclam changes the photocatalyitc activity of CO_2 reduction and redox properties of the supramolecules (Kimura et al., 1994; Schulz et al., 2012).

Beside the use of molecular complex photocatalysts, semiconductors such as TiO_2 (Szaniawska et al., 2018), ZnO (Cai et al., 2018), CdSe (Cho et al., 2018), $BiVO_4$ (Wei et al., 2018) others have been widely studied as well. Among them, TiO_2 has received considerable attention in the several fields such as photovoltaic cell (Grätzel, 2005), environment (Bessekhouad et al., 2003), built environment (Mills et al., 2006) and biomedicine (Mitoraj et al., 2007) due to its high reactivity, good stability, nontoxicity and cost-effectiveness. In general, TiO_2 naturally exists in three crystal phases at atmospheric pressure known as anatase, rutile and brookite. All of them contains TiO_6 octahedral unit but different on the manner in which the edges and corners are shared. In anatase, the edges are shared by four of the eight neighbors from each octahedral units while the others shared corners by forming (001) planes (Diebold, 2003; Hwang et al., 2015). Meanwhile, two edges and eight corners have been shared in octahedral unit of rutile where the corner forming (100) plane. The Ti-O bond length for anatase are 1.937 and 1.966 Ǻ, whereas in rutile the bond length are 1.946 and 1.983 Ǻ in the equatorial and axial directions, respectively (Diebold, 2003). Both corners and edges are connected in brookite (Di Paola et al., 2013; Xu, Lin, et al., 2015). The other TiO_2 polymorphs that have been reported comprising of TiO_2 II or Srilankite, cubic fluorite-type, pyrite-type, monoclinic baddeleyite-type and cotunnite-typre polymorphs (Hanaor & Sorrell, 2011). Among them, rutile is the most stable while anatase and brookite are metastable with the later is difficult to synthesize, thus is seldom used. The arrangement of atoms in the TiO_2 lattice which differ from each other gives different physical properties to TiO_2 as the density and band gap energy. For anatase and rutile phases, their gap energy band is 3.20 eV (384 nm) and 3.0 eV (410 nm), respectively.

In general, it has been accepted that anatase TiO_2 has a higher photocatalytic activity than other polymorphs although there is still a debate in literature about it. There are several reasons that anatase has a better photocatalytic activity. Having high band gap energy than rutile gives a meaningful advantage to the anatase. Although a high band gap band reduces the absorption of light, at the same time, it increases the valence band maximum of anatase TiO_2 to a higher level than the redox potential of the adsorbed molecule. This condition causes the oxidation power of anatase increases and the electron transfer can be more easily facilitate from TiO_2 to the adsorbed molecules (Luttrell et al., 2014). Surface properties of photocatalyst are another factor which plays an important role as a medium for the adsorption of molecules and subsequent charge transfer to the adsorbed molecules. These surface properties are not only polymorphs dependent but are also found within the same material as there is a difference in surface orientation. These surface properties need to be noted because they ultimately affect photocatalytic activity (Wilson & Idriss, 2002). Surface properties can be divided into four main categories, namely (a) chemical effects; for example the co-ordination of surface structures that control the adsorption of a molecule (Tao & Batzill, 2010), (b) the surface electronic structure or defect and adsorbate-induced states which is crucial for charge transfer and separation on the surface (Tao et al., 2011), (c) molecular interaction between the adsorbed molecules and the surface defects (Setvín et al., 2013) and (d) the difference in surface potential ie the difference in the work function measured in the vacuum and in the aqueous solution (Bullard & Cima, 2006). Anatase has an indirect band gap energy that is lower than that of rutile which is having direct band gap energy. Charge carriers lifetime in anatase is longer than that of rutile phase. The longer lifetime of charge carriers is important in photocatalytic reaction in order to minimize the recombination reaction and as a consequent, surface reaction can be facilitated effectively (Xu et al., 2011).

However, the efficiency of TiO_2 is limited due to several limiting factors such as rapid recombination of photogenerated charge carrier, large band gap and has a low absortion of visible light as compared to ultraviolet light. Therefore, some methods such as doping with transition metals, surface sensitization with organic dye, preparation of mixed phase, fabricating nanoscale particle size, identification of active plan have been used to increase TiO_2 light absorption capability into visible light. The implementation of TiO_2 as photocatalyst for CO_2 reduction into organic oxygenates are well documented in the literatures for more than a decade. Crystal structure, phases, morphology, surface area and particle size are among factors that influence the photocatalytic activity of TiO_2. The dependence of crystal facet of TiO_2 towards photocatalytic reduction of CO_2 has been investigated by Yamashita et al. (Yamashita et al., 1994). Among (100) and (110) facet of TiO_2, the former was more active than the later in producing methane and methanol with the value of 3.5 μmol/h g.cat and 2.4 μmol/h g.cat, respectively as compare to (110) facet which produced only 0.8 μmol/h g.cat of methanol and infavour to produce methane. Additionally, mixed facet of TiO_2 also has substantial effect on the amount of products. Xu et al. (Xu et al., 2013; Xu, Yu, et al., 2015) for example prepared 75% (100) and 25% (001) facets of TiO_2 cubes found that 4.56 and 1.48 μmol/h g.cat of methane and methanol formed, respectively, where the rate of formation of organic compounds over various facets is different with an order of (100) > (101) > (001). Besides crystal facets, other parameter such as particles size plays an important role in determining the photocatalytic activity of CO_2. Decreasing the particle size indeed increase the surface area of the prepared nanomaterials, however, on the other hand, the band gap energy will increase as well which lead to the reduction of light absorbing ability (Zhang et al., 1998). The relationship between band gap energy and the article size can be seen from the work of Koci et al. (Kočí et al., 2009) who prepared 4.5 – 29 nm TiO_2 found that the band gap energy decrease from 3.14 – 3.08 eV with the highest CO_2 conversion rate of 0.308 μmol/h g.cat with 14 nm size of TiO_2.

The reaction of CO_2 reduction using photoelectrochemical cells is one of the methods that can overcome the problems faced by photocatalytic systems such as back-oxidation of the generated products into CO_2 and rapid photogenerated charge carrier recombination. Photoelectrochemical cells contain photoanaode and photochatode which are connected to an external electrical circuit in the presence of electrolytes. Photoanode contains water oxidation catalysts while photocathode contains CO_2 reduction catalyst where water is used as an electron donor. Water will undergo oxidation process to produce H_2 gas which will flow through the proton exchange membrane and react with CO_2 at the cathode to produce the desired organic compounds such as formic acid, methanol and methane (Alstrum-Acevedo et al., 2005; Song et al., 2011). Photoelectrochemical reduction of CO_2 utilizing the combination of photocathode and dark anode has been used by Halmann for the first time in 1978. The photoelectrochemical cell consists of p-GaP, carbon and an aqueous buffered solution acting as photocathode, counter electrode and electrolyte, respectively. Upon irradiation with Hg lamp, the formation of HCOOH, HCHO and CH_3OH were detected (Halmann, 1978). Motivated from the work of Halmann as aforementioned above, various p-type semiconductors such as p-GaAs, p-InP, p-Si, N-doped Ta_2O_5 (N-Ta_2O_5), Cu_2O, p-NiO, p-Co_3O_4 and ZnTe have been exploited as photocathode for photoelectrochemical reduction of CO_2 (Zhao et al., 2014). However, there are still some issues that still need to be addressed in photoelectrochemical reduction of CO_2. Among them, the selectivity issues still remain as the major obstacle due to favaourable water reduction reaction, high overpotential due to less positive value of valence band of p-type semiconductor to oxidize water (Xie et al., 2016). However, combination with co-catalysts enables to activate the inert CO_2 molecule, hence enhancing the photocatalytic activity of CO_2 reduction reaction.

Mixing p-type semiconductor photocathodes with metal complexes have attracted considerable strategy among the researchers nowadays (Zhao et al., 2014). The main requirement for this approach is by designing the lowest unoccupied molecular orbital (LUMO) of the metal complexes to be more positive than the conduction band of semiconductors and more negative the reduction potential of CO_2 into a particular product. Hydrogen-terminated p-type Si with tricarbonyl complex Re(I) has been used for the purpose of CO_2 reduction reaction and the potential required for the purpose of CO_2 reduction was 600 mV lower when compared to potential using Pt electrode (Kumar et al., 2010; Kumar et al., 2012). Similar situations also can be observed for p-GaP photocathode with the presence of pyridine as electrocatalyst in the production of methanol where its electrical potential is 300 mV lower than the standard potential for the formation of methanol (Kumar et al., 2012). Motivated from the prior work, CO_2 conversion to formate was observed at Pt/TiO_2 photoanode coated onto a conducting glass coupled with p-type semiconductor modified with Ru(II) polymer photocathode. Water oxidation by the photogenerated hole produced on Pt/TiO_2 photoanode produces the electrons and protons required for CO_2 reduction reactions. Photoexcited electrons produced in the photoanode will be transferred to Ru(II) catalyst by p-type semiconductor and was used for CO_2 reduction reaction (Sato et al., 2011).

Instead of p-Si, CO could be formed by using a inexpensive p-type semiconductor namely Cu_2O. Though, amorphous TiO_2 layer is needed to protect the unstable Cu_2O under reductive conditions (Paracchino et al., 2011). Conjugation between Cu_2O, TiO_2 and Re(bipy-*t*-Bu)$(CO)_3Cl$ for the formation of CO reached the current density of 1.5 mA cm^{-2} with 100% Faradaic efficiency in acetonitrile. The high Faradaic efficiency of the combined Cu_2O-protected TiO_2 with Re bipyridyl complex eradicate photogenerated charge carriers limitations for photoelectrochemical reduction of CO_2 (Schreier et al., 2015). In addition, the formation of CO could also be observed in a hybrid system of Ru(II)-Re(I) supermolecular metal complex immobilized onto p-NiO which sustained high Faradai efficiency and durability (Sahara et al., 2015). Newly, the photocatalytic activity of CO_2 reduction reaction has been enhanced after the combination of conducting polymer such as polypyrrole with p-type semiconductor namely ZnTe photocathode in aqueous solution of $KHCO_3$ under visible light irradiation. The high Faradaic efficiency and selectivity towards the formation of HCOOH was attributed to the negative value of conduction band position of ZnTe which enables the fabricated materials to provide largest driving force for the transfer of charge carriers to an acceptor, thus suppressing the competitive hydrogen evolution reaction (Chung et al., 2015).

The interesting properties possessed by the 1-D semiconductor photocathodes such as high surface area, more active sites, excellent charge carriers transportation and potentially superior light absorption are one of the most recent strategies to improve the photoelectrocatalytic activity of CO_2 reduction reaction (Xia et al., 2003). The fabrication of 1-D ZnTe/ZnO/Zn through microwave assisted hydrothermal method showed the formation of CO at -0.7 to -0.2 V vs reverse hydrogen electrode (RHE) in aqueous solution of $KHCO_3$ with 60% incident photon-to-current conversion efficiency (IPCE) (Jang et al., 2014). Futhermore, methanol was observed as the major product for photoelectrochemical reduction of CO_2 over CuO-Cu_2O hydrid nanorod arrays under simulated sunlight in aqueous solution of 0.1 M Na_2SO_4 at -0.2 V vs standard hydrogen electrode (SHE) (Ghadimkhani et al., 2013). With the band gap of 2.07 eV, Co_3O_4 is another 1-D p-type semiconductor which offers promising outcomes for photoelectrochemical reduction of CO_2. Incorporation of Cu nanoparticles to Co_3O_4

nanotubes demonstrated high conversion of CO_2 to formate in aqueous solution of Na_2SO_4 under visible light irradiation with selectivity and formate concentration of nearly 100% and 6.75 mmol/L.cm^2 after 8 h of photoelectrocchemical reaction at -0.9 V (Huang et al., 2013; Shen et al., 2015).

The two electron products namely HCOOH and CO are commonly obtained during CO_2 reduction reaction over p-type semiconductor. However, due to the extensive competition reaction with water reduction, the efficiency is still low provided that p-type semiconductors are expensive or unstable under the reaction conditions. Therefore, *n*-type semiconductors such as TiO_2, $BiVO_4$ or WO_3 have been exploited as photoanode for CO_2 reduction reaction. Recently, HCOOH, CH_3OH, CH_3COOH and CH_3CH_2OH were obtained form the combination of Pt-TiO_2 nanotubes (Pt-TNT) photoanode and Pt modified reduced graphene oxide (Pt-RGO) cathode even under high bias potential (+2.0 V) with the optimum rate of formation of 1.5 mmol/h.cm^2 (Cheng et al., 2014). In addition to CH_4 and to CH_4 and CH_3OH, HCOOH was also obtained from the combination of N-doped TiO_2 photanode with Cu cathode under high bias potential of +2.8 V. The exploitation of N-doped TiO_2 enable the reduction reaction to be performed under visible region (Peng et al., 2012). Furthermore, the choice of metal cathode indeed influenced the formation of reduction products. For instant, CH_4 was observed as the major product along with the formation of CO and C_2H_4 when WO_3 photoanode, an n-type semiconductor was combined with Cu cathode. However, the Faradaic efficiency of the products increased from 42.3%, 4% and 5.1% to 67%, 2.7% and 0.6%, respectively as the applied voltage increased from +0.55 to +0.75 V. Meanwhile, the formation of products were totally different when the cathode was changed to Sn/SnO_x, the formation of HCOOH and CO were obtained as the main product along with the production of H_2 with the Faradaic efficiency of 27.5% and 15.8%, respectively at applied bias potential of +0.7 V (Magesh et al., 2014).

Before the study was made more thoroughly with the electrochemical reduction of CO_2 gas, there are several parameters to consider in the reaction involving electrochemistry such as onset potential, overpotential, current density, faradaic efficiency, tafel plot and electrochemical cell used. The onset potential, applied voltage and current density are interrelated among each other. The applied voltage where the current density can be calculated is known as the onset potential. Since the electrochemical reduction reaction of CO_2 need to overcome the kinetic barrier, the standard reduction potential is often more positive than the onset potential during the reaction. Hence, the difference between the standard reduction potential and onset potential will give the overpotential of the reaction. The performance of electrocatalysts can also be investigated by using Tafel plot which unite the logarithm of current density and overpotential of the reaction. Generally, a better electrocatalysts have a small Tafel slope indicative of better catalytic performance. Fabrication of electrochemical cell is very important in electrochemical research. The most common type of electrochemical cell is H-type cell which consist of two partitions for the placement of three electrodes namely working, counter and reference electrodes equipped with inlet and outlet gas valves. The cell is separated by proton exchange membrane (PEM) to circumvent the products crossover (Wang et al., 2018).

The production of organic compounds from CO_2 reduction reactions using electrochemical methods has been getting attention from researchers over the last few years especially in the production of CO, formic acid, formaldehyde, ethylene, methanol, ethanol and oxalic acid (Albo et al., 2015; Qiao et al., 2014). Some of the advantages of electrochemical reduction reaction of CO_2 are the ease of tuning the experimental conditions such as applied potential, the reaction take place at room temperature and pressure and the supplied electricity is used to generate the desired fuels or chemical feedstock without releasing extra CO_2 into environment.

Notwithstanding of the advantages, electrochemical process possesses several limitations that should be taken into account such as large overpotential required for the formation of $CO_2^{\bullet -}$ intermediate denoting lower efficiency of the reaction, reaction rates are rather low to the limited mass transfer ability of CO_2 to the surface of electrocatalysts, mixing gases and liquid products during the reaction cause the separation process costly. The surface of electrocatalysts can also be easily poisoned or blocked by the intermediates or by-products which lead to the deactivation of the electrocatalyst and lower the overall efficiency of the reaction (Akhade et al., 2014; Gangeri et al., 2009). The fundamental of electrochemical reduction of CO_2 is more difficult to understand as compared to to hydrogen evolution reaction (HER), oxygen evolution reaction (OER) and oxygen reduction reaction (ORR) since it involves multiple coupling steps of electrons and protons. Lastly, the occurance of side reaction such as HER which takes place at much lower potential is more favourable than the electrochemical CO_2 reduction reaction (ECR) should be addressed seriously by designing proper electrocatysts with high selectivity towards ECR rather HER.

There are many factors that affect the results of CO_2 reduction reactions such as electrode type, electrolyte concentration, temperature, pH, reaction medium either aqueous or organic solution (Barton Cole et al., 2010; Hori et al., 2003; Ogura et al., 1991). Therefore, the electrocatalyst selection and reaction conditions that provide high selectivity with low overpotential are the main goals in CO_2 reduction reactions. Homogeneous and heterogeneous catalysts have been used by dissolving the transition metal complexes within the electrolyte solution and using reactive electrode made of conductive materials to reduce CO_2.

The reaction of CO_2 reduction in aqueous solution experienced severe competition with the water decomposition reaction to H_2 and O_2 as well as a low CO_2 solubility in aqueous solution of 0.03 M only. Therefore, some organic solutions such as dimetylformamide (DMF), dimethyl sulfoxide (DMSO), propylene carbonate (PC), acetonitrile (AN) and methanol have been widely used as alternative medium for CO_2 reduction reaction not only to increase CO_2 absorption even to reduce competition with release H_2 (HER). Overall, in the organic medium, the metal electrodes can be divided into three groups, the first group consisting of Pd, Hg, Tl and Pb produces oxalate, the second group producing CO is Ni, Cu, In, Sn, Ag, Pt and Au and the third group consists of Cr, Fe, Mo, Pd and Cd form CO and oxalate (Amatore & Saveant, 1981; Fischer et al., 1981; Gennaro et al., 1996; Tomita et al., 2000).

The activation of CO_2 molecules over the surface of the metal electrode can be accomplished through three coordination namely through carbon atoms, oxygen or both. It is found that coordinated CO_2 molecules through carbon and oxygen atoms with steps and kinks are preferred for CO_2 reduction by lowering the bond angle to less than 180^o. Electrochemical reduction of CO_2 on Pt surfaces (210), (310) and (510) found that reducing reaction on open structure was preferred (Fan et al., 2007) and CO_2 reduction activity on the single crystal surface has been reported to increase in order of Pt (110) > Pt (100) > Pt (111) (Hoshi et al., 2003).

Furthermore, RuO_2/TiO_2 nanotube and RuO_2/TiO_2 nanoparticle have been studied for electrochemical reduction of CO_2 into methanol after modification with Pt electrode by Qu et al. (Qu et al., 2005). Their studies showed that RuO_2/TiO_2 nanotube exhibit 60.5% current efficiency as compared to RuO_2/TiO_2 nanoparticle (40.2%) in producing methanol. They also proposed that the nanotube surface structure in an important strategy in getting high efficiency for CO_2 reduction reaction. In another experiment conducted by Popic et al. (Popić et al., 1997) for CO_2 reduction over Ru, RuO_2 and RuO_x + IrO_x electrode surfaces showed relatively lower overpotential where methanol and acetone were found in the bulk of the electrolyte with the current efficiency of producing methanol was in the range of 15.3% to 38.2%. Furthermore, CO_2 reduction reaction over RuO_2 deposited or modified at different substrates have also been studied elsewhere (Bandi, 1990; Bandi & Kühne, 1992; Spataru et al., 2003). Furthermore, binary system of RuO_2/TiO_2 and multi-component system of $RuO_2/TiO_2/SnO_2/MoO_2$ were investigated towards the formation of methanol from electrochemical reduction of CO_2 in acidic solution of 0.05 M H_2SO_4 (pH 1.2) with Faradaic efficiency of 24% at -0.15 V vs recrese hydrogen electrode (RHE). However, the Faradic efficiency of binary RuO_2/TiO_2 was increased up to 74% in phosphate buffer of pH 4. Addition of Cu on the binary system of RuO_2/TiO_2 further enhanced the Faradaic efficiency toward methanol up to 30% for Cu doped 75:25 Ru:Ti electrode (Bandi, 1990; Bandi & Kühne, 1992).

Nowadays, numerous cobalt systems such as plane Co, CoO and Co-organic complexes have been used in catalytic reduction of CO_2 into hydrocarbons, such as CH_4 and CO in the presence of rare earth metal, in particular palladium, platinum, and/or alkali promoters like potassium (Russell & Miller, 1950). Recently, Co_3O_4 has been demontrated to reduce CO_2 electrochemically to CO with Faradaic efficiency of 65%. The used of polyacrylnitrile (PAN) as a polymeric template enable to produce high crystalline Co_3O_4 with extansion of surface active sites for the reduction reaction to proceed. The prepared Co_3O_4 electrode was reported to be stable after 8h of reaction with current density of 0.5 mA/cm^2 (Aljabour et al., 2018). However, the formation of product for CO_2 reduction depends on the reaction medium. The reduction reaction in non-aqueous solvent such as acetonitrile after considering of solubility of CO_2 (0.27 M at room temperature and pressure in acetonitruile) enable the suppression of hydrogen evolution reaction (HER) from water splitting. Nevertheless, small amount of water (1% v/v H_2O, 0.55 M) in acetonitrile produced formate as by-product in addition to CO formation, considering that Co_3O_4 favors formate generation in aqueous solution (Gao et al., 2016).

In recent time, manganese oxide (MnO_2) has attracted attention in various electrochemical applications such as oxygen reduction reaction catalyst due to its environmental friendly, cheap and unique electrochemical proeprties (Roche & Scott, 2009; Zhang et al., 2019). However, the investigation of MnO_2 as CO_2 reduction catalyst is scarcely reported. For example, metal-nitrogen-doped carbon (M-N-C) electrocatalysts where M was Mn, Fe, Co, Ni, and Cu have been syntehsized for CO_2 reduction reaction. However, the electrocatalytic performance of Mn-N-C remains largely limited, especially as compared with Fe-N-C and Ni-N-C catalysts (Ju et al., 2017; Möller et al., 2019; Pan et al., 2018). In another report, the formation of CO over MnO_2 nanosheets array supported nickel foam which has been prepared by hydrothermal method has been obtained with current density of 14.1 mA/cm^2 and Faradaic efficiency of 71% after 10 h. The excellent Faradaic efficiency was reported due to the well-distributed MnO_2 nanosheet which provide a much higher density of accessible active sites for CO_2 reduction reaction, thus enabling better selectivity for CO_2 reduction (Peng et al., 2019).

Lately, Ni-based catalyst such as $Ni(OH)_2$ has been utilized in various applications due to the high abundance, low cost, low toxicity and high capacitance. In general, $Ni(OH)_2$ exists in two phases namely α- and β-phases. The former is a metastable phase and can be easily transformed into the β-phase during synthesis and in a strong alkaline medium, while β-phase is a hexagonal phase isostructural with brucite $Mg(OH)_2$ (Yang, 2002). $Ni(OH)_2$ has received increasing attention as positive electrodes of alkaline rechargeable batteries for decades (Wu et al., 2019), in addition to other applications such as direct oxidation of carbohydrates (Ganesh et al., 2011), supercapacitor (Lokhande et al., 2018), water splitting (Zhou et al., 2014) and sensor (Zhou et al., 2017). The high performance of $Ni(OH)_2$ in electrochemical applications is influenced by its morphological properties and the particle size. The optimum performance of

$Ni(OH)_2$ is influenced by the synthetic method, solvents, precipitating agents, surfactants, temperature, pH, ageing time and nickel salt concentration. A flower-like morphology between 0.7 to 1.0 µm size was obtained by ultrasound synthesis from an aqueous ammonia solution (Cabanas-Polo et al., 2011) by Jeerapan *et al*. who reported that the size of the $Ni(OH)_2$ nanoparticles can be decreased from 12-14 nm to 7 nm with the addition of polyvinylpyrolidone in hydrazine hydrate at temperature of 54-65 °C (Tientong et al., 2014). Furthermore, different types of solvent used during synthesis influenced the presence of different $Ni(OH)_2$ phases. In such case, $Ni(OH)_2$ prepared in ammonia and sodium hydroxide gave predominantly the β-phase while urea produced only the α-phase (Acharya et al., 2003).

A part from various synthetic methods that have been introduced to prepare $Ni(OH)_2$, selecting an appropriate application for $Ni(OH)_2$ is vital and the most momentous research nowadays is concerning global environmental problem and generation of green energy. Thus, form the authors point of view, it is imperative to scrutinize the effectiveness of $Ni(OH)_2$ to mitigate CO_2 through photoelectrochemical reduction reaction. Only a few research works on reduction of CO_2 have been done implementing $Ni(OH)_2$ can be found from literatures as compared to other application such as HER (Cao et al., 2019; Xu et al., 2018), degradation of pollutant (Regmi et al., 2018; Sharma et al., 2017) and sensor (Pal et al., 2018). For example, a hybrid nanocomposite of $Ni(OH)_2/TiO_2$ for the photocatalytic reduction of CO_2 in aqueous medium result in the formation of CH_4 with photoreduction rate of 2.20 $\mu mol/g_{cat}.h$ after 0.5 wt% of $Ni(OH)_2$ loading while loading with 15 wt% $Ni(OH)_2$ lead to the formation of CH_3OH (0.58 $\mu mol/g_{cat}.h$) and CH_3CH_2OH (0.37 $\mu mol/g_{cat}.h$). The presence of $Ni(OH)_2$ in the nanocomposites increases the selectivity of the product besides acting as the co-catalyst (Meng et al., 2018). Another recent study of photoreduction of CO_2 over $Ni(OH)_2$ doped water dispersible graphene was conducted by Siva et. al (Palanisamy &

Srinivasan, 2019) over different types of electrolyte namely $NaHCO_3$, $KHCO_3$ and $NaCO_3$ in aqueous medium to produce CO. Their report stated that $NaHCO_3$ is a better choice of electrolyte for the formation of CO as compared to other electrolytes. However, details report on the role of $Ni(OH)_2$ for the formation of CO from photoreduction of CO_2 has not been discussed so far. Another investigation of photoreduction of CO_2 into CO also has been reported by Lei et al. (Dai et al., 2017) over Cu/$Ni(OH)_2$ in 0.5 M $KHCO_3$ against reverse hydrogen electrode (RHE). Eventhough the formation of CO reached the Faradaic efficiency of 92% with photocurrent density of 4.3 mA/cm^2, least attention has been paid to the function of $Ni(OH)_2$ and reaction mechanism of photocatalytic reduction of CO_2 rather than the importance of Cu has been acknowledge a lot. Some recent studies related to the photocatalytic reduction of CO_2 were tabulated in **Table 2.4** below.

Table 2.4 Photoelectrochemical reduction of CO_2 into organic oxygenates.

Photocatalysts	**Reaction medium**	**Electrolyte**	**Light source**	**Major product**	**Faradaic Efficiency (%)**	**References**
TiO_2 based photocatalysts						
TiO_2/M-phthalocyanine (M = Ni, Co, Sn)	Aqueous	0.1 M Na_2SO_4	300 W Hg lamp	CO	98	(Kobayashi et al., 2020)
N-doped TiO_2	Aqueous	0.1 M $KHCO_3$	100 W Xe lamp	CH_4	7.83	(Peng et al., 2012)
Pt-Reduced graphene oxide‖Pt-TiO_2 nanotube	Aqueous	1 M $NaHCO_3$	300 W Xe arc lamp	HCOOH	40	(Cheng et al., 2015)
$Cu_2O/TiO_2–Cu^+$	Aqueous	0.3 M $KHCO_3$	AM 1.5 G irradiation	CH_3OH	56.5	(Lee et al., 2018)
Ni-foam/amine-functionalized TiO_2	Aqueous	0.1 M $KHCO_3$	N/A	CH_3OH	100	(Wang et al., 2017)
Si/TiO_2/Pt	Aqueous	0.1M $NaHCO_3$	125 W UV–Vis	CH_3CH_2OH	97	(Guaraldo et al., 2015)
Pt/Hydroxyapatite/TiO_2	Aqueous	0.5 M Na_2SO_4	Visible light	CH_4	95	(Chong et al., 2018)
Cu_2O/non-stoichiometric TiO_2	Aqueous	0.1 M Na_2SO_4	150 W Xe lamp	CH_3OH	N/A	(Szaniawska et al., 2018)
Pt/graphene aerogel/Cu foam/TiO_2	Aqueous	0.5M $NaHCO_3$	Xe lamp	CH_3CH_2OH	30	(Zhang et al., 2017)
TiO_2/ p-GaP	Aqueous	0.5 M NaCl	Green laser	CH_3OH	55	(Zeng et al., 2014)
N-TiO_2	Aqueous	0.1 M $KHCO_3$	100 W Xe lamp	CH_4	7.83	(Peng et al., 2012)
Sn/ TiO_2	Aqueous	0.5M $NaHCO_3$	300 W Xe lamp	$HCOO^-$	70	(Irtem et al., 2017)
CoO_x/TiO_2	Aqueous	0.5M Na_2SO_4	300 W Xe lamp	HCOOH	60.9	(Pan et al., 2020)
$WO_{3–x}/TiO_2$	Aqueous	0.5M $KHCO_3$	500 W Xe lamp	HCOOH	N/A	(Yang et al., 2016)
Pt/TiO_2/Pt/RGO/Ni foam	Aqueous	0.5M $NaHCO_3$	300 W Xe lamp	HCOOH, EtOH	N/A	(Zhang et al., 2016)

Table 2.4, continued.

$Ti/TiO_2/ZrO_2$	Aqueous	0.1M Na_2SO_4	125 W Hg lamp	CH_3OH	N/A	(Perini et al., 2018)
Cu_2O/AZO/TiO_2/Re	Non-aqueous	0.1M Bu_4NPF_6	N/A	CO	80 - 95	(Schreier et al., 2016)
$InP/TiO_2/Cu$	Non-queous	0.5 M KCl	Visible light	CH_3OH	8.7	(Qiu et al., 2015)
CdSeTe NSs/TiO_2	Aqueous	0.1 M $KHCO_3$	500 W Xe lamp	CH_3OH	88	(Li et al., 2014)
$GaAs/InGaP/TiO_2/Ni$	Aqueous	2.8 M $KHCO_3$	N/A	$HCOO^-$	94	(Zhou et al., 2016)
$Cu/Si/TiO_2$	Aqueous	1M $NaHCO_3$	150 W Xe lamp	CO	N/A	(LaTempa et al., 2012)
$CuGaS_2$/RGO–TiO_2	Aqueous	0.05 - 0.1 M Na_2S, 0.1 M K_2SO_3	300 W Xe lamp	CO, HCOOH	N/A	(Takayama et al., 2017)
TiO_2	Aqueous	N/A	High pressure Hg lamp	CH4 + CH_3OH + CO	N/A	(Anpo et al., 1995)
TiO_2	Aqueous	N/A	UV light	CH_4		(Tan et al., 2006)
N-Fe_2O_3/TiO_2	Aqueous	0.1M $NaHCO_3$	Hg lamp	HCOOH	N/A	(Jiang et al., 2018)
FeS_2/TiO_2	Aqueous	0.1M $KaHCO_3$	500 W Xe lamp	CH_3OH	40	(Han et al., 2018)
TiO_2/KIT-6	Aqueous	N/A	300 W UV lamp	CO	22	(Hussain et al., 2015)
N-TiO_2	Aqueous	$NaHCO_3$	300 W Xe lamp	CH_3OH, CH_2O, CH_4	N/A	(Akple et al., 2015)
Pt/C-TiO_2	Aqueous	0.1M KNO_3	150 W Xe lamp	CH_4	N/A	(Tasbihi et al., 2019)
Ag/brookite TiO_2	Aqueous	$NaHCO_3$	300 WXe lamp	CO/CH_4	N/A	(Li et al., 2016)

Table 2.4, continued.

Non-TiO_2 nased photocatalysts						
CdS/N-doped carbon particles	Aqueous	0.5M $NaHCO_3$	300 W Xe lamp	CH_3OH	77.3	(Cheng et al., 2020)
InGaN/GaN	Aqueous	1.0M NaCl	300 W Xe lamp	HCOOH	1.09	(Sheu et al., 2017)
Sn/*p*-Si	Aqueous	0.1M $KHCO_3$	AM 1.5 G light	$HCOO^-$	7.8	(Choi et al., 2014)
Cu-Co_3O_4	Aqueous	0.1M Na_2SO_4	Visible light	$HCOO^-$	~100	(Shen et al., 2015)
ZnTe-Zn/ZnO	Aqueous	0.5M $KHCO_3$	500 W Hg lamp	CO	22.9	(Jang et al., 2014)
Co-MoS_2	Aqueous	0.1M $KHCO_3$	500 W Xe lamp	CH_3OH	N/A	(Peng et al., 2015)
ZnO/ZnSe	Aqueous	0.5M $NaHCO_3$	150 W Xe lamp	CO	97	(Cai et al., 2018)
Mg-$CuFeO_2$	Aqueous	0.1M $NaHCO_3$	75 W Xe lamp	$HCOO^-$	10	(Gu et al., 2013)
SnO_2/Fe_2O_3	Aqueous	0.1M $KHCO_3$	Xe lamp	CH_3OH	87	(Yang et al., 2017)
p-InP	Non-Aqueous	0.3 M TBAP	Xe lamp	CO	93	(Hirota et al., 1998)
Fe/$ZnGa_2O_4$	Aqueous	0.2 M Na_2SO_4	300 W lightning cure	CO	N/A	(Liang et al., 2020)
$Bi_2O_2(OH)NO_3$/*g*-C_3N_4	Aqueous	0.5 M Na_2SO_4	300 W Xe lamp	CO	N/A	(Liu et al., 2019)
$CuFe_2O_4$	Aqueous	0.1M $NaHCO_3$	300 W Xe lamp	CH_3OH	14.4	(Karim et al., 2018)
Co_3O_4/ $Ru(bpy)_2dppz$	Aqueous	0.1M $NaHCO_3$	Xe lamp	$HCOO^-$	86	(Huang et al., 2016)

CHAPTER 3: MATERIALS AND METHODOLOGY

3.1 General Contemplations

This chapter highlighted the synthetic methodology of the catalysts namely RuO_2-MnO_2-Co_3O_4 supported anatase TiO_2 and $Ni(OH)_2$ by precipitation and hydrothermal method, respectively, while electrophoretic deposition method has been used for thin film fabrication. The prepared RuO_2-MnO_2-Co_3O_4 supported anatase TiO_2 and $Ni(OH)_2$ were tested for photoelectrochemical applications such as methanol oxidation and CO_2 reduction reactions in the presence of visible light in aqueous and N,N-dimethylformamide (DMF). The preparation methods for both catalysts were presented in **Figure 3.1** and **Figure 3.2**.

3.2 Chemicals

25% ammonia solution, ruthenium trichloride monohydrate ($RuCl_3.H_2O$) was procured from Merck; acethylene black, polivinylidene fluoride (PVDF), lithium perchlorate ($LiClO_4$), urea, manganese nitrate tetrahydrate ($Mn(NO_3)_2.4H_2O$) and 0.1 M KCl solution with 1 mM $[Fe(CN)_6]^{4-}/[Fe(CN)_6]^{3-}$ (1:1) mixture solution were purchased from Sigma-Aldrich; Nickel nitrate.$4H_2O$ ($Ni(NO_3)_2.4H_2O$), cobalt nitrate hexahydrate ($Co(NO_3)_2.6H_2O$) and methanol (MeOH, 99.8%) were obtained from Fisher Scientific; and anatase TiO_2 (particle size: 5nm, surface area: 289 m^2/g) was purchased from US Research Nanomaterials, Inc., Pt/C was obtained from Fuel Cell Earth LLC (US) and N,N-dimethylformamide (DMF) was purchased from Brendemann Schmidt Chemical.

3.3 Photoelectrochemical studies

All photoelectrochemical studies in this work were carried out on an Autolab potentiostat/galvanostat (Ecochemie, Netherlands) at ambient temperature and presure in a photoelectrochemical cell obtained from PINE Research Instrumentation, US by the implementation of 1 cm^2 thin film of the respective photocatalysts on FTO slides as working electrode which were ultrasonically cleaned with distilled water and acetone several times and dried at ambient temperature before deposition by using electrophoretic deposition. Photoelectrochemical oxidation of methanol was studied by cyclic voltammetry (CV) in aqueous solute on of 0.1 M KOH at different concentration of methanol from 0 to 5 M in the potential ranges of -0.5 to 0.5 V vs Ag/AgCl at 50 mV/s. The commercial TiO_2 and Pt/C catalyst (10% Pt). The ferro/ferri cyanide $[Fe(CN)_6]^{4-}/[Fe(CN)_6]^{3-}$ (1:1) redox couple were purchased from Sigma-Aldrich (USA), and dissolved (1 mM) in 0.1M KCl for the EIS measurements (Shahid et al., 2014). Meanwhile, photoelectrochemical reduction of CO_2 (at -0.5 V vs Ag/AgCl) was inversitgated by using linear sweep voltammetry (LSV) and chronoamperometry (CA) in aqueous and DMF solution of 0.2 M $LiClO_4$ in the potential range of -1 to 0.2 V vs Ag/AgCl at ambient temperature after CO_2 bubbling for 1 h. Both photoelectrochemical studies were performed by using a 150 Watt halogen lamp was obtained from Alltion Co. Ltd. (China) as the light source throughout the experiment. Both photoelectrochemical oxidation of methanol and reduction of CO_2 used platinum wire, Ag/AgCl and the prepared catalysts as counter, reference and working electrodes, respectively. The Faradaic efficiency was calculated by using the following formula of Faradaic efficiency (F.E) = $(\alpha \text{ x } n_{product} \text{ x } F)/Q$ where, α refers to the number of electron needed to for product evolution, $n_{product}$ is the concentration of product, F is Faradaic constant and Q is the total charge passed during the reaction.

3.4 Synthesis of photocatalysts

3.4.1 RuO_2-MnO_2.Co_3O_4 supported anatase TiO_2

RuO_2-MnO_2.Co_3O_4 supported onto anatase TiO_2 for photoelectrochemical oxidation of methanol was prepared by dissolving 0.046 g (2.0 mmol) $RuCl_3.H_2O$, 0.915 g (3.9 mmol) $Mn(NO_3)_2.4H_2O$ and 0.998 g (3.4 mmol) $Co(NO_3)_2.6H_2O$ in 50 ml of deionized water and acidified with 0.1 M HCl to pH 5. Then 2.003 g (25.1 mmol) anatase TiO_2 was added to the solution with continuous stirring for 30 min to produce a fine suspension. The precipitate was filtered and washed with water and ethanol several times followed by oven drying for overnight at 120 ^oC to yield a homogeneous black powder which was then manually grounded into a fine powder on the next day. The obtained fine black powder was calcined in a tube furnace under hydrogen/oxygen atmosphere for 3 cycles at 450 ^oC by using quartz tube in the tube furnace in order to activate the catalyst. Before the curing process took place, the air inside the quartz tube was evacuated with Argon for 1h after the prepared catalyst was added in the quartz tube. After the temperature reached 450 ^oC, then H_2 gas was purged inside the quartz tube for 3h. After 3 h of purging H_2, once again Ar was purged for 1 h to evacuate H_2, purging with O_2 for 3 h to complete one cycle. The process is followed by purging with Ar for 1 h for everytime changing the gas from H_2 to O_2 and from O_2 back to H_2 until all 3 cycles were completed. The thin film of the prepared catalyst was fabricated through electrophoretic deposition method. The electrophoretic solution was prepared by sonicating 100 mg of RuO_2-MnO_2.Co_3O_4 supported onto anatase TiO_2 photocatalyst for 30 min in 0.1 mM NH_3. The electrophoretic deposition process was carried out for 5 min at +15 V.

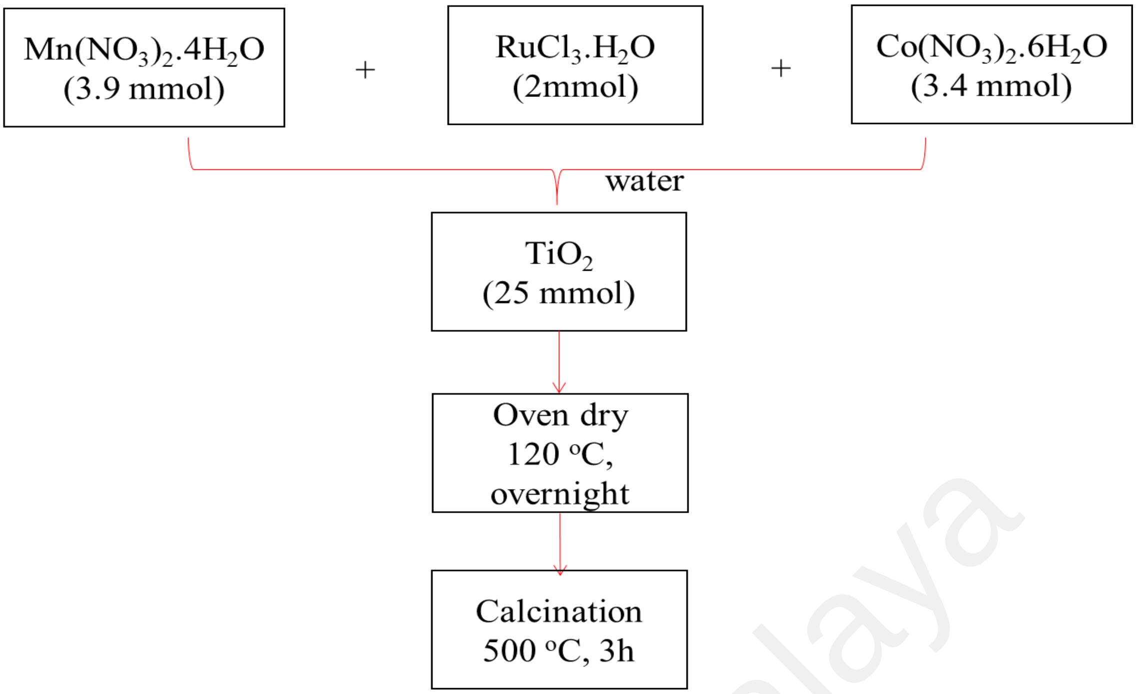

Figure 3.1: Schematic diagram of the synthesis of RuO_2-MnO_2-Co_3O_4 supported onto anatase TiO_2.

3.4.2 $Ni(OH)_2$

Nickel (II) hydroxide ($Ni(OH)_2$) powder was synthesized using 0.60 g $Ni(NO_3)_2.6H_2O$ and 0.25 g urea, dissolved in 100 ml distilled water with stirring at room temperature for 2 h. The $Ni(OH)_2$ powder was collected and washed with distilled water several times and dried in an oven at 90°C. The $Ni(OH)_2$ electrodes were fabricated using the $Ni(OH)_2$ powders with acetylene black and poly(vinylidene) fluoride (PVDF) binder in a weight ratio of 8:1:1. The mixture was pressed onto a thin nickel foam to form the electrode. The mixture was autoclaved at 100 °C for 12 h.

The amount of CO_2 in aqueous and non-aqueous solution is determined by using the titration method. Briefly, 10 mL of carbonated solution was mixed with 30 mL aqueous NaOH (0.5 M) and 30 mL $BaCl_2$ (0.5 M). Then, phenolphtalein indicator was added and the solution was titrated with 1.0 M HCl until colorless. After that, methyl orange indicator was added until the orange colour turn pink. Equation of calculating the amount of dissolved CO_2 is shown in Equation (3.1) below.

Amount of CO_2 (ppm) = (Normality of NaOH x Equivalent weight of CO_2 x Volume of NaOH taken)/Volume of sample taken (3.1)

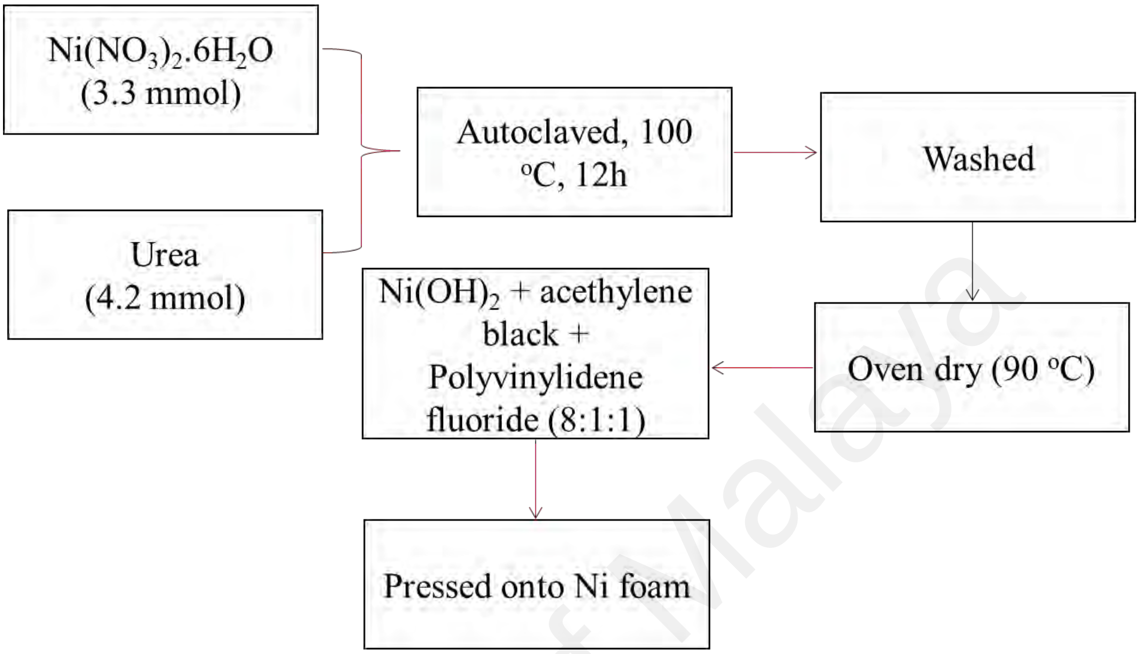

Figure 3.2: Schematic diagram of the synthesis of $Ni(OH)_2$.

3.5 Characterizations

3.5.1 Scotch tape test

The scotch tape test or adhesion test was performed to determine bonding strength between sample and substrate after the formation of thin film. Several constraints such as pulling angle, pulling rate and type of tape predisposed the consequence of the test. If the quality of the film is poor, the deposited film will be adhered to the tape after the tape was pulled out.

3.5.2 X-ray diffraction (XRD)

XRD is non-destructive characterization method and commonly used as a fingerprint tool in analizing of a substance. It is used to characterize the crystalline material, the dimensions of the cell unit, and the purity of the sample and identify the fine minerals such as mixed layer clay, which cannot be determined optically. The interaction between X-rays with a crystalline material causes this radiation to diverge and the relationship between the wavelength, the diffraction angle and the lattice spacing in the crystalline sample can be linked to the Bragg Law $n\lambda=2d\sin\theta$ where λ is the wavelength of the irradiating X-ray, d is the lattice spacing and θ the angle diffracted. X-ray diffraction (XRD) patterns of the thin films were obtained between 5^{o} to 90^{o} 2θ on a PANanalytical EMPYREAN diffractometer with Cu $K\alpha_1$ radiation (λ = 1.54060 Å), at a step size of 0.01^{o}, with an operating current and voltage of 40 mA and 40 kV, respectively.

3.5.3 UV-Vis spectroscopy

UV-Vis deals with electronic transitions fro lower to higher energy levels. Most UV-Vis spectrometers consist of light source normally built up from a tungsten-filament lamp (scanning visible region) and hydrogen or deuterium discharge tube (scanning near UV region), sample and reference cells which were made from silica or quartz, a wavelength selection device or monochromator to spread out the wavelength either by using prisms or diffraction grating and a detector to receive the radiation and then transfer into spectrum. The band gap energy between the valence and conduction band of the photocatalyst(s) can be calculated from UV-Vis spectrum by employing the following equation:

$$\Delta E_{bg} = hc/\lambda = 1239.95/\lambda \qquad (3.1)$$

where, E_{bg} = band gap energy in eV; h = Plank‘s constant = 6.63 x 10^{-34} Js; c = speed of light = 3 x 10^{8} m/s and λ = wavelength in nm. UV-Vis spectrum of the powdered catalyst was recorded on Lambda 750 Perkin-Elmer diffuse reflectance UV-Vis-NIR spectrophotometer, between wavelength ranges of 300 - 900 nm.

3.5.4 Photoluminescence spectroscopy

Photoluminescence is the emission of light from any materials after absorbtion of photons or electromagnetic radiation. Photoluminescence spectrum was obtained by Micro-Raman PL system of Renishaw at the excitation of 325nm under He-Cd laser source.

3.5.5 X-ray photoelectron spectroscopy (XPS)

It is well known that, the interaction of an object with electromagnetic beam will result in the release of electrons. The XPS spectra are obtained by releasing the electron from the sample surface after irradiating with monoenergetic Al Kα X-rays. The free electrons resulting from these reactions are called as photoelectrons. Due to the law of conservation of energy, the free energy of the bonded electron, E_b can be determined if the incident energy and kinetic energy, E_{kin} are known by using $E_{kin} = h_v - E_b$. The kinetic energy is the characteristic of the sample studied and used to determine the existence of an element and the oxidation number of the element. Hence, XPS is also useful characterization technique to study the interfacial phenomena at solid-state and solid-gas boundries. The typical XPS spectrum consists of a plot of the number of electron released against the binding energy of the electrons identified. Therefore, it has been widely utilize in numerous industrial and research applications including photovoltaics, catalysis, corrosion, adhesion, coating, magnetic media and display technology. XPS was performed by ULVAC-PHI Quantera II with 32 channels Spherical Capacitor Energy Analyzer under vacuum (1 x 10^6 Pa) with monochromated Al K_α radiation (1486.8 eV) and a natural energy width of 680 meV. The carbonaceous C 1s line (284.6 eV) was used as the reference to calibrate the binding energies.

3.5.6 Raman spectroscopy

Raman is one of the most common non-destructive techniques used to determine the crystallinity of a material. The Raman spectroscopy concept is based on the inelastic scattering of the laser light due to the excitation of vibration, rotation, and other low frequency modes in the sample which leads to the formation of Raman shift. The Raman spectroscopy is essential in informing the chemical structure of a material. Raman spectrum (Renishaw, InviaRaman Microscope) was recorded between 4000 - 100 cm^{-1}.

3.5.7 Fourier transformed infrared spectroscopy (FTIR)

Infrared spectroscopy is the study of interaction of infrared light with matter based on the vibration of the atoms of a molecule. It is indeed a useful technique in industrial applications such as pharmaceutical, food, agricultural, pulp and paper and environmental field. The most common type of spectrometer nowadays is called Fourier Transform Infrared (FTIR). The spectrum may be recorded for organic and inorganic samples, if they can absorb light energy with the frequency in the IR region at 14,000 - 10 cm^{-1} which can be further divided into three categories namely far-, mid- and near infrared which corresponds to 400 – 10 cm^{-1}, 4000 – 400 cm^{-1} and 14,000 – 4000 cm^{-1}, respectively. A molecule should have a change in its dipole moment during the vibration in order to be IR active. Fourier transformed infrared spectrum (FTIR) was obtained from 4000 -200 cm^{-1} on a Perkin Elmer 400FTIR/FT-FIR spectrometer.

3.5.8 Field Emission Scanning Electron Microscope-Energy Dispersive X-ray (FESEM-EDX)

Morphology and elemental composition of a substance can be determined by using field emission scanning electron microscope (FESEM) when the electrons removed from the hot tungsten filament strike the surface of the material under the airtight conditions. The surface topology information of a substance will be obtained after the secondary electron interacts with the surface of the material. Conduction band electrons are released as soon as the electron beam strikes the sample surface. In addition, the electron beam can also be re-reflected and this electron reflection is used to determine the presence of an element in the sample. This process will continue until the image of the sample surface is obtained. Meanwhile, EDX spectroscopy indentifies the elment present in the sample by bombarding the sample with high-energy electrons. The information regarding the elemental composition of the prepared sample canbe determined by using the process so-called X-ray mapping. The detector used in EDX spectroscopy is lithium-drifted silicon or silicon drifted detector in the range of 100 eV – 20 keV. However, by using high purity germanium (HpGe), the detection range can be extended to 100 keV. Thus, making EDX spectroscopy a useful technique in measuring the entire element of the periodic table exceot H, Li, B and He. The morphology and elemental analyses were performed with a field emission scanning electron microscope-energy dispersive X-ray (FESEM-EDX) SU8220 Hitachi.

3.5.9 Temperature Programmed Reduction (TPR)

Reduced metal oxides will form if the original metal oxide reacts with hydrogen gas. This process can be studied by the temperature programmed reduction (TPR). This method also determines the ability of a substance to be removed when reacting with hydrogen gas. The hydrogen gas streamed will eliminate the oxygen atom contained in the oxygen lattice inside the metal oxide structure to produce the reduced species. Each metal oxide reacts with hydrogen at different temperatures. By this method, the oxidation number of a substance and the number of each species can also be determined. The faster the rate of hydrogen consumption, the easier materials to be removed. The ability of a material to be reduced is also closely related to the oxygen-movment in the lattices of metal oxides. If the metal oxide has a high hydrogen consumption rate at a small temperature range then oxygen movement is high and it is easy to be reduced. Whereas, if the metal oxide has low hydrogen consumption rate at a large temperature range, it is difficult to reduce and has a low oxygen movement. The temperature programmed reduction (TPR) was performed using ThermoFinnigan TPDRO 1100 series. For the pretreatment conditions for TPR analysis has been done under N_2 atmosphere with the flow rate and ramping rate of 20 ccm/min and 10 ^{o}C/min, respectively. The pretreatment temperature was started at 25 ^{o}C and stopped at 120 ^{o}C. Meanwhile, the conditions used for the TPR analysis was including the gas used, flow rate, ramping rate, holding time, start and end temperature were 5% H_2 in N_2, 20 ccm/min, 10 ^{o}C/min, 60 minutes, 40 ^{o}C and 900 ^{o}C, correspondingly.

3.5.10 Surface area analysis

The determination of porosity is one of the non-destructive analysis methods. It is based on the amount of gas absorbed when the pressure is increased. Among the information obtained from porosity analysis is surface area (S_{BET}), pore size, pore size distribution and void structures. The determination of this surface area is based on the gas absorption, usually N_2 gas, onto the catalyst surface at the condensing temperature of the gas used for example, the condensation temperature of N_2 gas is at 77 K. The surface area analysis of the catalysts were studied using Brunauer-Emmett-Teller (BET) Micromeritics TristarII. The BET analysis was conducted at 90 ^{o}C to 200 ^{o}C with holding time 1 h and 4 h, respectively.

CHAPTER 4: RESULTS AND DISCUSSIONS

4.1 Photoelectrochemical oxidation of methanol

Since direct methanol fuel cell (DMFC) uses expensive rare metals such as platinum, the results in this manuscript suggest that it is possible to fabricate a catalyst based on cheap and readily available metals such as manganese and cobalt. However, the use of expensive rare metals such as ruthenium as the co-catalyst is minimized to 1%, while TiO_2 is used as the support for the photo-oxidation of methanol. The various oxidation states of Ru, Mn and Co is another factor which modifies the band gap of TiO_2 to enhance the photocatalytic performance, the conductivity, as well as the stability of the as-prepared photocatalyst.

The RuO_2-MnO_2-Co_3O_4 catalyst supported onto porous anatase, TiO_2, with a surface area of 289 m^2/g was prepared by dissolving the precursor salts in deionized water acidified with hydrochloric acid. The solution was stirred for 30 minutes to produce homogeneous slurry which was dried slowly at 395 K overnight. The black powder obtained was grinded in a mortar and pestle to produce a fine powder, calcined at 500 ^oC for 6 hours and divided into two parts. One part was used for the deposition of thin films on FTO by electrophoretic deposition technique and the second part was used for XRD, UV-Vis, FTIR, Raman, BET, TPR, XPS and FESEM-EDX analyses. Both the deposited thin film catalysts and the powders were cured at 500 ^oC for 3 h in hydrogen gas. Finally, the thin films were tested for methanol oxidation and the powder for analysis.

4.1.1 Structural characterization of of RuO_2-MnO_2-Co_3O_4 supported anatase

The XRD pattern of the hydrogen cured RuO_2-MnO_2-Co_3O_4 powder supported on anatase TiO_2 is displayed in **Figure 4.1**. The diffraction peaks at 2θ of 25.4^o, 37.9^o, 48.3^o, 55.2^o, 62.8^o, 75.1^o and 83.0^o are attributed to the anatase phase, corresponds to the (101), (004), (200), (211), (204), (215) and (312) diffraction planes respectively, and matches with the ICDS no.00-004-0477 of the tetragonal crystal system, space group I41/amd with a = b =3.7830 Å and c = 9.5100 Å; $\alpha = \beta = \gamma = 90^o$. The diffraction peaks of tetragonal RuO_2 with space group of P42/mnm was observed at 2θ of 27.5°, 35.1°, 40.0°, 65.6°, 69.0°, 74.0° and 83.0° which correspond to the (110), (101), (111), (221), (301), (202) and (321) diffraction planes respectively, with the unit cell parameters of a = b = 4.5200 Å and c = 3.1160o; $\alpha = \beta = \gamma = 90^o$, which agrees with the ICDS card no. 00-065-2824.

Manganese seems to exist in two different phases of $MnTiO_3$ and MnO_2. The diffraction peaks of rhombohedral Pyrophanite ($MnTiO_3$) at 2θ values of 23.7°, 32.3°, 40.0°, 48.3°, 52.5°, 55.2°, 61.0°, 62.8°, 69.1°, 69.9° and 73.9° are attributed to the diffraction planes of (012), (104), (110), (024), (116), (018), (214), (300), (1010), (119) and (220) respectively. The Pyrophanite has the space group of R-3 with unit cell parameters of a = b = 5.1370 and c = 14.2900 Å; $\alpha = \beta = 90^o$ and $\gamma = 120^o$ that matches very well with the ICDS card no. 00-012-0435. The orthorhombic manganese dioxide (MnO_2) has 2θ values of 27.5°, 35.1°, 41.4°, 56.7° and 69.1° and are attributed to the (1 2 0), (1 3 0), (2 1 0), (2 4 0) and (0 6 1) diffraction planes, which matches with the space group of Pbnm (a = 4.5330 Å, b = 9.2700 Å, c = 2.8660 Å; $\alpha = \beta = \gamma = 90.0000^o$) of ICDS no. 00-007-0222. All these two types of manganese oxide phases could have formed during the curing process.

Meanwhile, cobalt oxides appear as two different phases of Co_3O_4 and $CoTiO_3$. The diffraction peaks of cubic Co_3O_4 at 2θ of 36.2°, 37.9°, 44.3°, 48.3°, 54.6° and 64.2° is attributed to the diffraction planes of (311), (222), (400), (331), (422) and (440), respectively. The cubic Co_3O_4 has the space group of Fd-3m with the unit cell parameters of a = b = c = 8.1975 Å; $\alpha = \beta = \gamma = 90^o$, matches very well with the ICDS card no. 01-080-1540. Furthermore, the diffraction peaks of orthorhombic $CoTiO_3$ was observed at 2θ of 35.1°, 36.2°, 37.9°, 40.0°, 44.3°, 55.2° and 56.7° are attributed to the diffraction planes of (211), (311), (222), (320), (321), (410), (510) and (511) respectively with the unit cell of a = b = c = 8.4680 Å; $\alpha = \beta = \gamma = 90.0000^o$, matches with the ICDS no. 00-029-0516.

The presence of $MnTiO_3$ and $CoTiO_3$ solid solutions in the composite is evident from the XRD pattern shown in **Figure 4.1.** These metal oxides were formed during the catalyst preparation and sintering processes. **Table 4.1** shows the concurrence of XRD peaks of the catalyst cured in three cycles of H_2/O_2 indicating the presence of $MnTiO_3$ and $CoTiO_3$ in addition to RuO_2, MnO_2 and Co_3O_4. The existence of these bimetallic oxides was further supported by the Raman scattering, where the peaks at 377 cm^{-1} and 206 cm^{-1} indicate the existence of $CoTiO_3$ and $MnTiO_3$, respectively.

The formation of $MnTiO_3$ and $CoTiO_3$ are mainly due to the presence of oxygen vacancies during the catalyst pre-treatment with hydrogen, thus allowing the Mn and Co to diffuse into the titania crystal lattice. This is in accordance with the work of E. Bailon-Garcia (Bailón-García et al., 2015) who reported that the formation of 2-D Pt nanoparticles and oxygen vacancies favours the Pt diffusion into the TiO_2 lattice after the H_2-treatment. The Debye-Scherrer's formula $D = K\lambda/\beta \cos \theta$ (where D is the crystallite size; K is a dimensionless constant = 0.94; λ is the X-ray wavelength equal to 1.54056 Å; β is the full-width at half-maximum of the diffraction peak and θ is the diffraction angle) was used to estimate the crystallite size from the main (101) lattice reflection at 2θ of 25.44° and was found to be 21.2 nm.

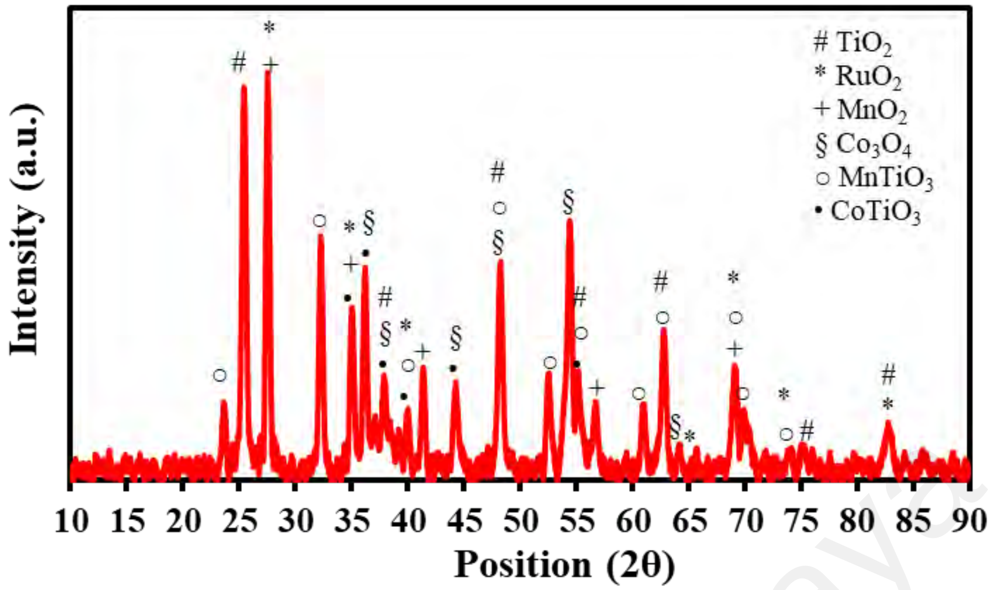

Figure 4.1: XRD pattern of RuO_2-MnO_2-Co_3O_4 supported TiO_2.

Table 4.1: Concurrence of XRD peaks of RuO_2-MnO_2-Co_3O_4 supported TiO_2.

Detected compounds from XRD					
2*θ* value					
TiO_2	**RuO_2**	**MnO_2**	**Co_3O_4**	**$CoTiO_3$**	**$MnTiO_3$**
					23.7°
25.4°					
	27.5°	27.5°			
					32.3°
	35.1°	35.1°		35.1°	
			36.2°	36.2°	
37.9°			37.9°	37.9°	
	40.0°			40.0°	40.0°
		41.4°			
			44.3°	44.3°	
48.3°			48.3°		48.3°
					52.5°
			54.6°		
55.2°				55.2°	55.2°
		56.7°		56.7°	
					61.0°
62.8°					62.8°
			64.2°		
	65.6°				
	69.0°	69.1°			69.1°
					69.9°
	74.0°				73.9°
75.1°					
83.0°	83.0°				

The FTIR spectrum of titania supported catalyst displayed in **Figure 4.2** reveals absorption bands below 1000 cm^{-1} due to the inter-atomic vibrations. The presence of various oxide species of Ru, Mn, Co and Ti might be the main reason for the obscurity of the peak of each element. For example, the FTIR of Ti-O-Ti occurs around 590 cm^{-1} (Rajakumar et al., 2012), while 456 cm^{-1} and 562 cm^{-1} (Kannan & Sundrarajan, 2015) are assigned to the bonding or stretching vibrations of RuO_2. The O-Mn-O vibrations can be observed at 475 cm^{-1} which showed the presence of MnO_2 (Jaganyi et al., 2013). Furthermore, the presence of a very weak peak at 531 cm^{-1} also indicative of the existence of Mn-O bond among MnO_2 (Mylarappa et al., 2016). The stretching and bridging vibrations of Co-O and Co-O-Co are located around 564 cm^{-1} and 665 cm^{-1} respectively (Trivedi & Prasad, 2016). Meanwhile, peak at 3500 cm^{-1} was assigned to the presence of stretching vibration of OH- group (Vetrivel et al., 2015).

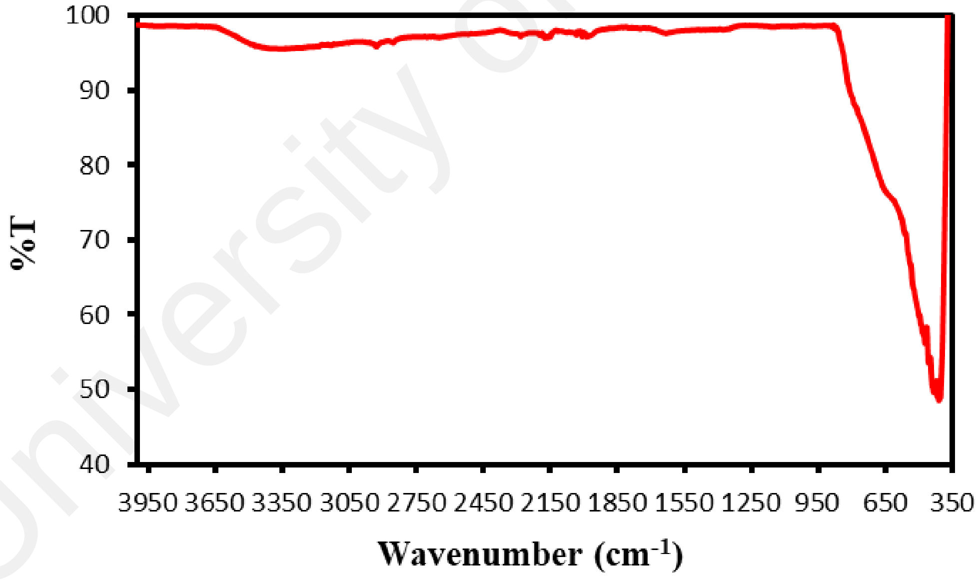

Figure 4.2: FTIR spectrum of RuO_2-MnO_2-Co_3O_4 supported TiO_2.

Figure 4.3 shows the Raman spectrum of trimetallic catalyst supported anatase. It is generally observed that the Raman scattering for TiO_2 is strong, while the absorption peaks due to other components such as RuO_2, MnO_2 and Co_3O_4 are weaker due to their lower concentration. The Raman scattering of TiO_2 anatase phase appears at 145, 198, 396, 505 and 633 cm^{-1} which corresponds to the E_g, E_g, B_{1g}, A_{1g}+E_g and E_g symmetries, respectively (Arsov et al., 1991). However, a slight shift in the Raman peak at 505 cm^{-1} as compared to Arsov et al. (Arsov et al., 1991) might be due to the changes in the crystal lattice of TiO_2. This effect is due to the migration of Mn and Co during the formation of the $MnTiO_3$ and $CoTiO_3$ phases, are observed at 228 cm^{-1}, 254 cm^{-1}, 327 cm^{-1} and 362 cm^{-1} (Avcı et al., 2014). The Raman scattering peaks for RuO_2, MnO_2, Co_3O_4 is indicated in **Table 2**.

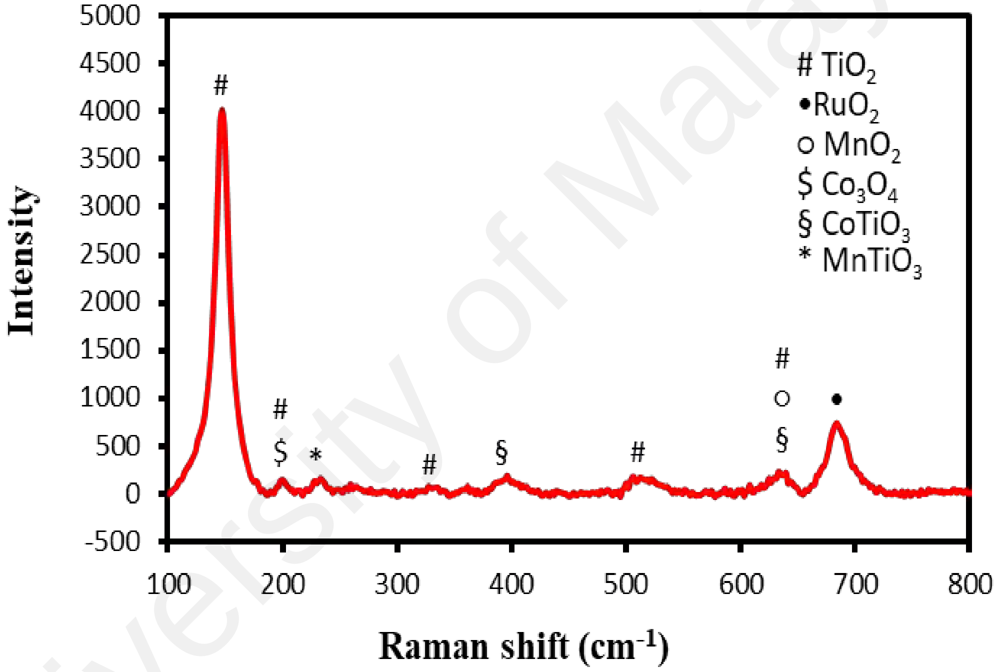

Figure 4.3: Raman spectrum of RuO_2-MnO_2-Co_3O_4 supported TiO_2.

Table 4.2: Raman peaks of RuO_2-MnO_2-Co_3O_4 supported TiO_2.

Raman shift of metal oxides (cm^{-1})						
Ru/Mn/ Co/TiO_2	**TiO_2 (Arsov et al., 1991)**	**RuO_2 (Korotcov et al., 2007)**	**MnO_2 (Zahn, 1999)**	**Co_3O_4 (Shahid et al., 2015)**	**$CoTiO_3$ (Avcı et al., 2014)**	**$MnTiO_3$ (Avcı et al., 2014)**
145	144					
					156	158
198	197			192		
						206
228					224	224
254					258	255
327					328	326
						352
					377	
396	399					
						426
					443	
			476			
505						
	516	528	523	516		
						606
				612		
633	639	646	633			
						676
683				680	684	
		716				

4.1.2 Optical properties of RuO_2-MnO_2-Co_3O_4 supported TiO_2

The as-prepared titania supported catalyst was investigated by UV-Vis spectrophotometry between the wavelength range of 380 – 850 nm (**Figure 4.4**) to gain an insight of the band gap. The UV-Vis spectrum of the trimetallic catalyst showed a wide absorption range which gradually increases towards higher energy with an optimum absorption between 400 – 800 nm as compared to pure titania which was 360 nm. The calculated band gap from the Tauc‘s plot gives a value of 1.66 eV, indicative of a good decrement in the band gap of titania. The decrease in band gap value of the trimetallic catalyst as compared to the pure titania namely 3.3 eV is expected to enhance light absorption and hence photocatalytic performance. The optical absorption threshold (λ_g) can be calculated by the equation of $\lambda_g = 1240$/band gap (Kerkez-Kuyumcu et al., 2015), with a value of 747 nm indicative of a red shift to the visible region. The synergic effect generated between the transition metals and TiO_2 enhances the ability of TiO_2 to absorb light in the visible region and introduces a new band gap state that allows the efficient charge carrier pair generation and separation (Kerkez-Kuyumcu et al., 2015; Momeni & Nazari, 2016). In addition, the absorption of the RuO_2-MnO_2-Co_3O_4 supported TiO_2 in the visible region is most probably due to the surface plasmon effect, which is related to the excitation of collective electron oscillations in the metallic oxides (Uddin et al., 2013). Zhu et al. (Zhu et al., 2006) and Klosek et al. (Klosek & Raftery, 2001) reported that the d-orbitals of Fe^{3+}-TiO_2 and V-TiO_2 were lowered below the conduction band, whereby the electrons from the valence band could be excited easily to the conduction band due to the decrease in the band gap energy of the transition metals-semiconductor heterostructures. The Kubelka-Munk equation was used to determine the band gap value of the as-prepared catalyst and is given as follows:

$$Ah\upsilon = A[(h\upsilon - E_g)]^n \qquad (4.1)$$

where, α is the absorption coefficient; h is the Plank‘s constant (4.136 x 10^{-15} eV); υ is the light frequency (3 x 10^8 ms^{-1}); A is a constant (~1); E_g is the band gap energy and n is equal to 2 for indirect allowed transitions. The conduction band edge and valance band edge for RuO_2, MnO_2 and Co_3O_4 supported anatse TiO_2 are tabulated in **Table 4.3**. The details calculation for the RuO_2, MnO_2 and Co_3O_4 supported anatse TiO_2 are given in **Appendix**.

Table 4.3: Valance band and conduction band edge for the RuO_2, MnO_2 and Co_3O_4 supported anatse TiO_2.

Metal oxides	**Valance band (eV)**	**Conduction Band (eV)**
RuO_2	-0.50	-2.16
MnO_2	-0.63	-2.29
Co_3O_4	-1.85	-0.71
TiO_2	-0.71	-2.37

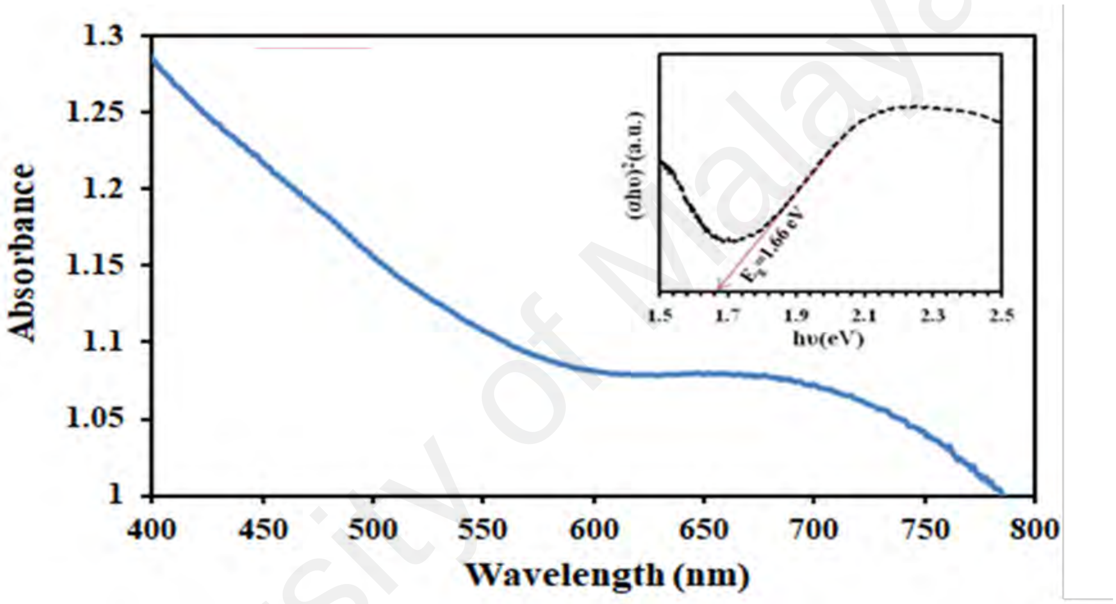

Figure 4.4: The UV-Vis absorption spectrum and inset: the Tauc's plot of energy vs $(\alpha h\upsilon)^2$ of RuO_2-MnO_2-Co_3O_4 supported TiO_2.

The recombination of photogenerated charge carriers and defect levels of anatase TiO_2 and the as-prepared catalyst was investigated by using photoluminescence spectroscopy (PL) as indicated in **Figure 4.5.** Self-trapped excitation that originates from the interaction of conduction band electrons on Ti 3d and holes of the valence band on oxygen 2p at 432 nm in anatase TiO_2 was not observed in the as-prepared catalyst. Both the pure anatase and the prepared catalyst gave a coincidence peak at around 566 nm in the visible region which is indicative of the presence of defects due to the oxygen vacancies in the materials (Chang et al., 2012; Mathew et al., 2012). The lower intensity of the trimetallic RuO_2-MnO_2-Co_3O_4 supported anatase TiO_2 indicates a better separation and suppression of the recombination process of photogenerated charge carriers. The broad peak of the unmodified anatase TiO_2 around 700 nm indicates a poor separation of the electrons and holes. Furthermore, based on the previous study (Choudhury & Choudhury, 2013; Xu et al., 2005a), metal doping such as Mn affect the photoluminescence intensity through the formation of a large number of non-radiative centres and luminescence quenchers (Choudhury & Choudhury, 2013; Xu et al., 2005b). Furthermore, the decrease in the intensity of the photoluminescence spectrum was also reported by Nakajima and Shi (Nakajima et al., 2004; Shi et al., 2007), with Pt doping into anatase TiO_2 due to the efficient electron transfer from anatase TiO_2 to Pt nanoparticles, by improving the charge carriers separation process, and confining electrons in Pt and holes in the valence band of TiO_2.

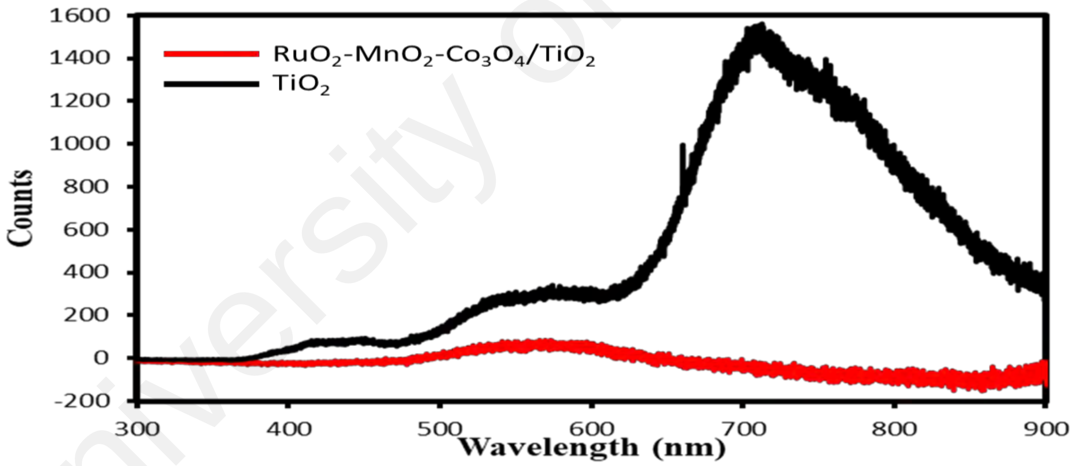

Figure 4.5: PL spectrum of RuO_2-MnO_2.Co_3O_4 supported TiO_2.

4.1.3 Surface characterizations of RuO_2-MnO_2-Co_3O_4 supported TiO_2

X-ray photoelectron spectroscopy (XPS) is a powerful technique to investigate the surface chemical bonding and the electronic valence band positions. **Figure 4.6** presents the XPS spectra of the RuO_2-MnO_2-Co_3O_4 supported anatase TiO_2 photocatalyst. The peak located around 286 eV is attributed to the C 1s of adventitious carbon-based contaminants. The two peaks in the Ti 2p region, namely the Ti $2p_{3/2}$ and Ti $2p_{1/2}$ peaks are located at 459.5 and 456.2 eV, respectively. The separation of the Ti $2p_{3/2}$ and Ti $2p_{1/2}$ peaks is 5.7 eV, which is in a good agreement with the Ti^{4+} oxidation state (Uddin et al., 2013). The detection of the Ru oxidation state must be based on the Ru $3d_{5/2}$ which is located at 281.4 eV, since the Ru $3d_{3/2}$ peak overlaps with the C 1s peak. This observation is indicative of the presence of Ru^{4+} cation, as expected from the presence of RuO_2 in XRD (Uddin et al., 2013). The binding energies of 642.3 and 654.5 eV are attributed to the Mn $2p_{3/2}$ and Mn $2p_{1/2}$. The spin orbit splitting between the Mn $2p_{3/2}$ and Mn $2p_{1/2}$ is 12.2 eV, indicative of the +4 oxidation state of manganese due to the formation of the MnO_2 (Harichandran et al., 2014). Furthermore, the spin orbit doublet for Co 2p is observed at binding energies of 780.8 eV (Co $2p_{3/2}$) and 795.7 eV (Co $2p_{1/2}$). In addition, two shake up satellite peaks appear at 786.5 eV and 803.9 eV (Xu et al., 2012). The appearance of the first satellite peak at 5.7 eV above the Co $2p_{3/2}$ peak is indicative of the Co^{2+}, while the second satellite peak at 8.2 eV above the Co $2p_{1/2}$ is a characteristic of the Co^{3+}. The Ti-O-Ti bond can be observed from the fitting of O 1s at 530.6 eV, in accordance with the literature (Sahu et al., 2009).

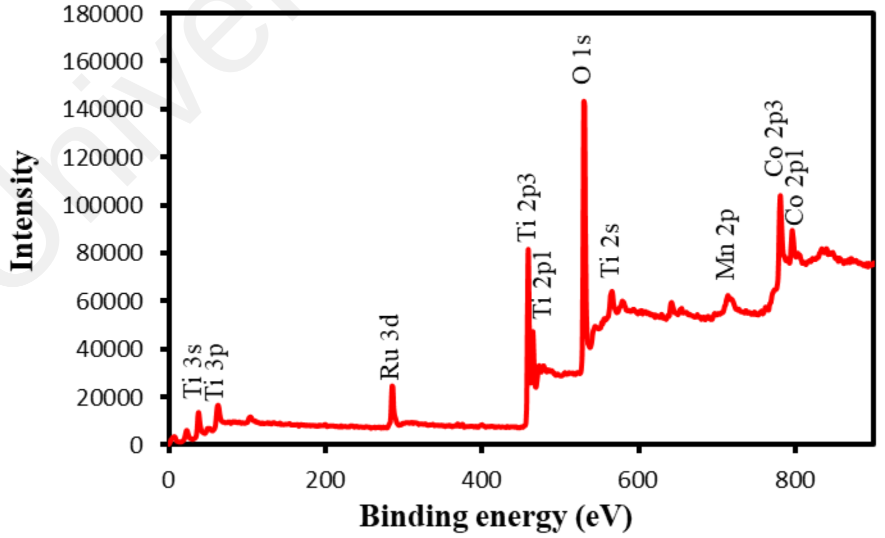

Figure 4.6: XPS spectrum of RuO_2-MnO_2-Co_3O_4 supported TiO_2.

FESEM and TEM analysis were used to study the surface morphology, geometry of the catalytic active site, as well as the interaction with the catalyst-support. **Figure 4.7a** and **Figure 4.7b** show the FESEM images of the as-prepared catalyst and the commercial anatase TiO_2. The TEM images indicates that the as-prepared catalyst from **Figure 4.7c** are well deposited onto the surface of small particle size and high surface area TiO_2 (**Figure 4.7d**). Thus, providing efficient visible light absorbtion for photooxidation of methanol. The presence of an applied electric field during the 20,000 - 100,000 magnifications in the FESEM does not influence the surface morphology and structure of the catalyst. EDX spectroscopy was carried out to investigate the chemical purity and stoichiometry of the catalyst. The EDX spectrum with the presence of elements such as Ru, Mn, Co, Ti and O is showed in **Figure 4.8**. The intensity of XPS spectrum showed that the ratio of the expected element in the prepared catalyst is comparable with EDX analysis (**Table 4.4**). Hence, the trimetallic anatase supported catalyst was successfully synthesized by using the method described in **Chapter 3**.

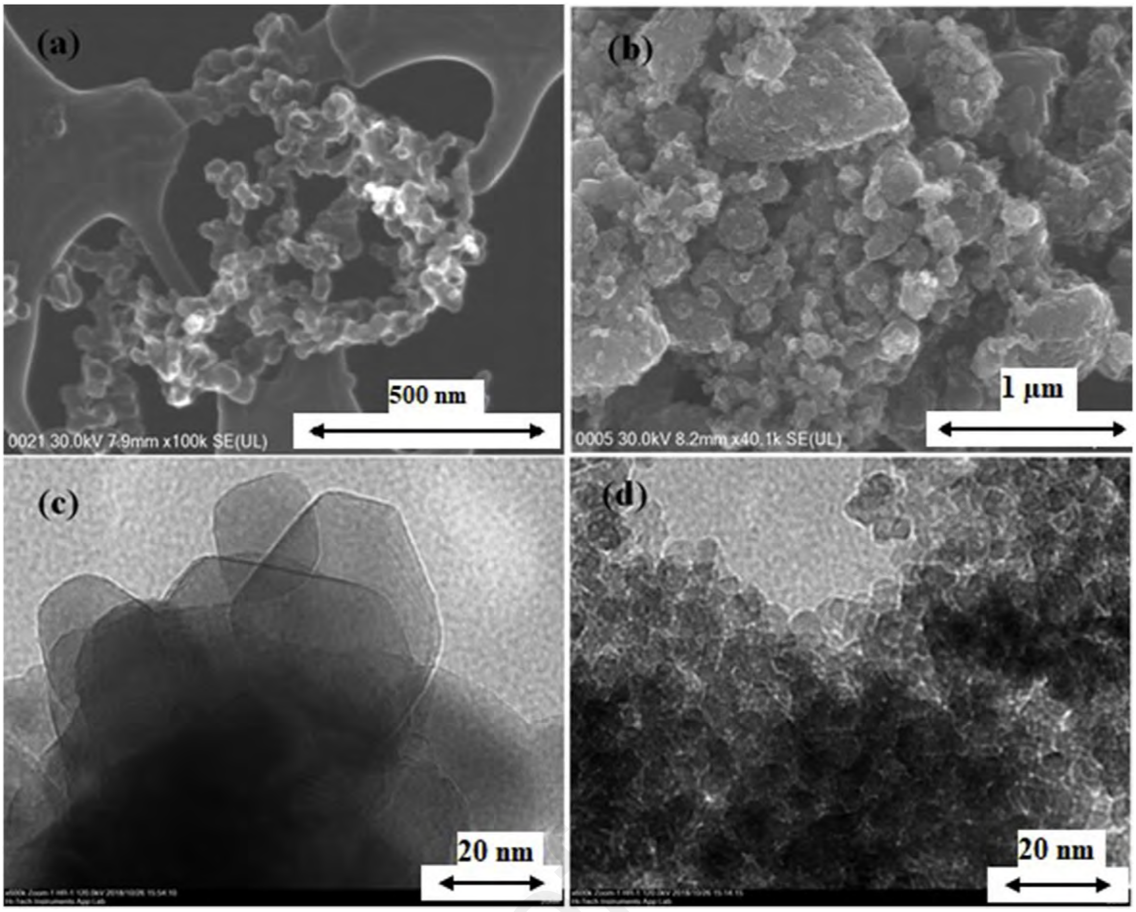

Figure 4.7: FESEM images of (a) RuO_2-MnO_2-Co_3O_4 catalyst supported TiO_2, (b) commercial TiO_2; TEM images of (c) RuO_2-MnO_2-Co_3O_4 supported TiO_2 and (d) commercial TiO_2.

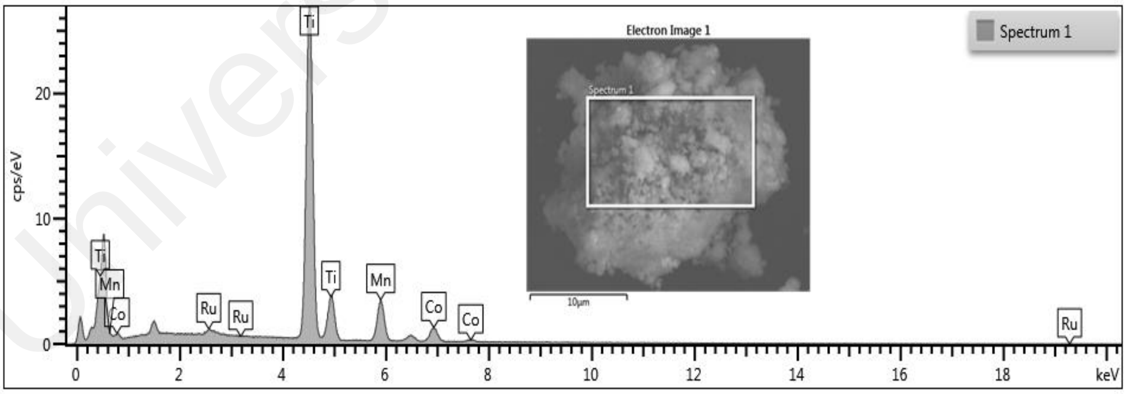

Figure 4.8: EDX spectrum of RuO_2-MnO_2-Co_3O_4 catalyst supported TiO_2.

Table 4.4: EDX composition table of RuO_2-MnO_2-Co_3O_4 catalyst supported TiO_2.

Element	**Line Type**	**Apparent Concentration**	**k Ratio**	**Wt%**	**Wt% Sigma**	**Atomic %**	**Std Label**	**Factory Standard**
Ti	K series	34.31	0.34312	68.41	0.19	72.46	Ti	Yes
Mn	K series	6.18	0.06176	14.41	0.13	13.31	Mn	Yes
Co	K series	6.80	0.06801	15.65	0.15	13.47	Co	Yes
Ru	L series	0.68	0.00679	1.52	0.14	0.76	Ru	Yes
Total:				100		100		

4.1.4 Isotherm analysis of RuO_2-MnO_2-Co_3O_4 supported TiO_2

The BET surface area plot and nitrogen adsorption-desorption isotherm of the as-prepared catalyst and commercial anatase TiO_2 are shown in **Figure 4.9 – 4.11**. The data indicated that the prepared catalyst exhibit type II isotherm for macroporous solid possessing, with a BET surface area of 20.5 m^2 g^{-1} whereas the commercial anatase TiO_2 revealed type IV isotherm indicative of mesoporous properties with BET surface area of 123.1 m^2 g^{-1}. The pore volume and pore size for the synthesized catalyst were 0.00014 cm^3 g^{-1} and 14.5 nm, correspondingly, as compared to anatase TiO_2 which were 0.0037 cm^3 g^{-1} and 2.6 nm for the pore volume and pore diameter, respectively. The lower surface area of the prepared trimetallic catalyst compared to anatase TO_2 suggests successful adsorption of RuO_2, MnO_2 and Co_3O_4 on the surface of anatase TiO_2, thus offering excellent light absorbtion and charge carrier separation. Furthermore, the incorporation of metals onto the surface of TiO_2 enhanced the conductivity of the catalyst as reported by Uddin et al. (Uddin et al., 2013).

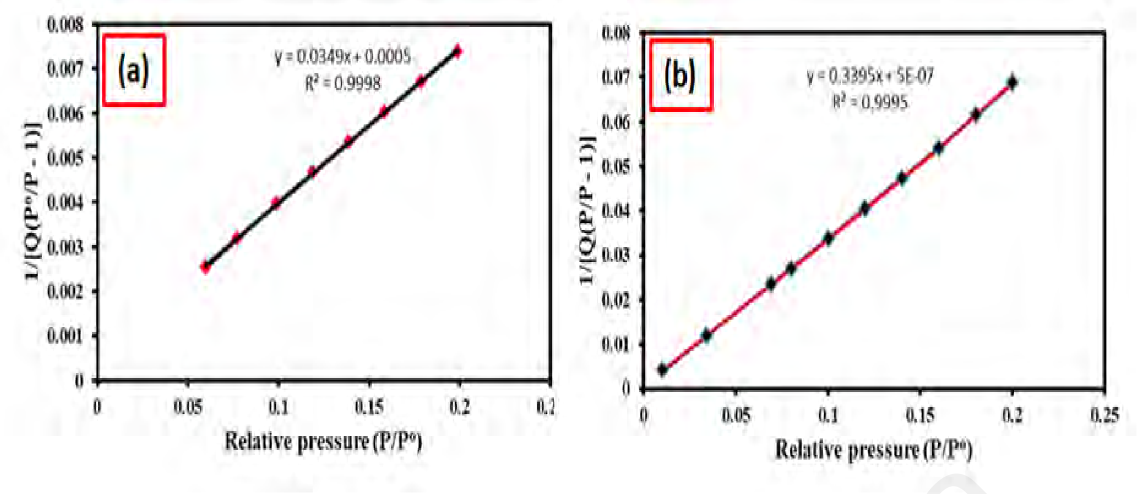

Figure 4.9: BET surface area plot of (a) TiO_2 and (b) RuO_2-MnO_2-Co_3O_4 catalyst supported TiO_2.

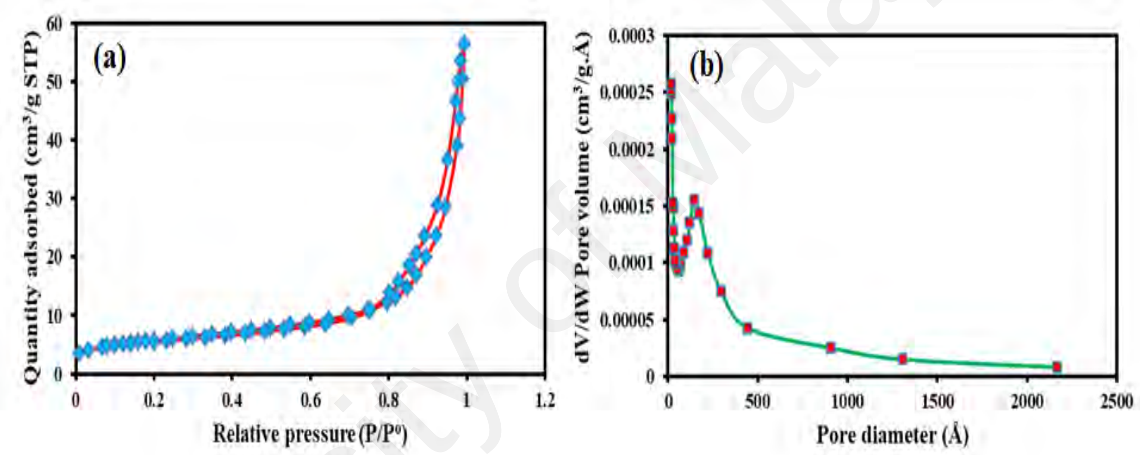

Figure 4.10: (a) N_2 adsorption-desorption isotherms and (b) corresponding BJH pore size distribution plot of RuO_2-MnO_2-Co_3O_4 catalyst supported TiO_2.

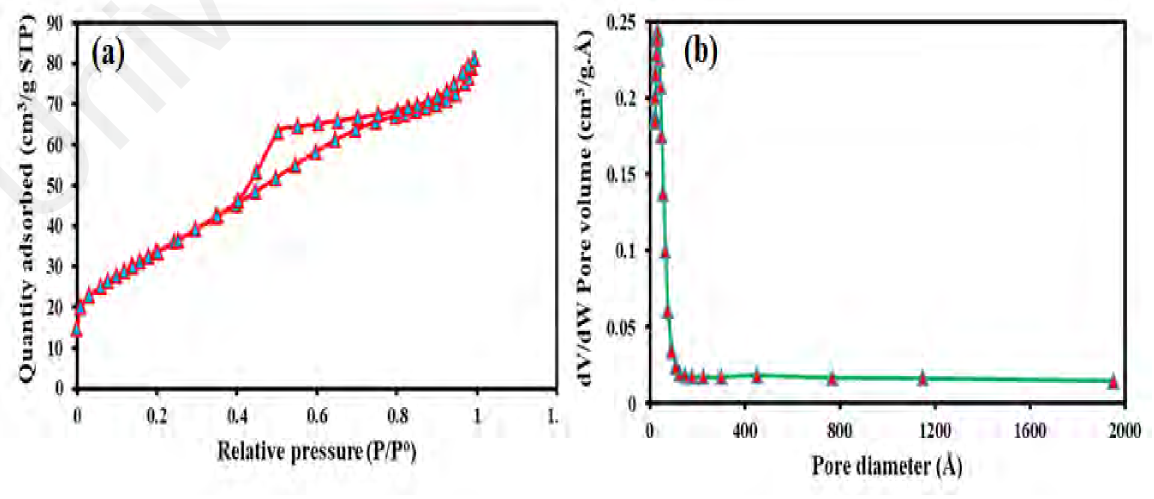

Figure 4.11: (a) N_2 adsorption-desorption isotherms and (b) corresponding BJH pore size distribution plot of TiO_2.

The presence of high electrical conductivity of semiconductor metal oxides is very important for better performance in photocatalytic reaction. The obtained information about the reducibility of the catalyst, the nature of the metal oxide phases and the interaction of the phases with the TiO_2 support are from the H_2-TPR (**Figure 4.12**). H_2-TPR analysis conducted up to 900 ^oC showed three peaks at 220 ^oC, 333 ^oC and 575 ^oC. The sharp peak at 220 ^oC attributed to the reduction of Co_3O_4 (Phienluphon et al., 2014) and the appearance of a broad shoulder in a lower temperature range of 120 to 200 ^oC attributed to the reduction peak of MnO_x and RuO_2 (Mei et al., 2014; Zhao et al., 2015). It is generally accepted that the noble metal oxides are reduced at lower temperatures to facilitate the dissociation of hydrogen via the hydrogen spill-over and thus enhance the reduction process (Lee et al., 2015). The second highest reduction peak at 333 ^oC attributed to the formation of metallic cobalt (Co^0) (Pan & Bukur, 2011). The reduction of TiO_2 was observed at a much higher temperature of 575 ^oC and was in good agreement with the reported (Cao et al., 2016) value of 500 – 750 ^oC.

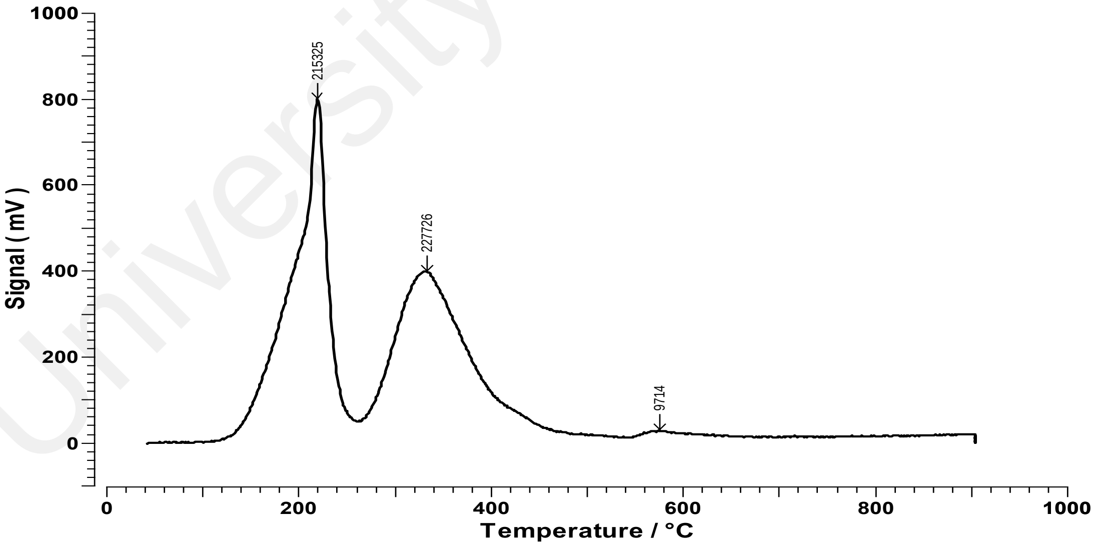

Figure 4.12: H_2-TPR spectrum of RuO_2-MnO_2-Co_3O_4 catalyst supported TiO_2.

4.1.5 PEC methanol oxidation of RuO_2-MnO_2-Co_3O_4 supported TiO_2

The photoelectrochemical oxidation of 0.5 M – 5 M methanol was studied (**Figure 4.13a)** to evaluate the performance of the as-prepared catalyst. The presence of a weak oxidation peak at around +0.3 V (0.12 mA/cm^2) in the absence of methanol and light (0.1 M aqueous KOH) was due to oxidation of water to H_2 and O_2. As the concentration of methanol increases from 0.5 M to 4 M, the current increases to a maximum value of 0.37 mA cm^{-2}. The increase in the photocurrent could be due to the efficient electron-hole separation and effective hole scavenging processes due to the presence of methanol (Lim et al., 2014). However, the peak current starts to level-off at 0.14 mA/cm^2 with a higher concentration of methanol (5 M). This behaviour could be due to the insufficient presence of photogenerated holes at the TiO_2 surface for the further oxidation of methanol (Zhang et al., 2007). The photoelectrochemical oxidation of methanol was also been performed with a commercial Pt/C and TiO_2 catalyst (**Figure 4.13b** and **Figure 4.13c**) as a comparison. The result indicated that the methanol oxidation takes place at a maximum concentration of 3 M, with a photocurrent value of 0.54 mA/cm^2 at -0.12 V. The photocurrent started to decrease with the further increase in the methanol concentration, probably due to the CO poisoning of the Pt/C surface. To further confirmed the oxidation reaction of methanol over commercial anatase TiO_2, the experiment was conducted at the 0.1 – 5 M methanol. At low concentration of methanol namely at 0.1 to 0.4 M (**Figure 4.14**), the current gradually increased until a sudden increment for the concentration of 0.5 M. However, as the concentration of methanol increase from 0.5 M to 5 M, the current slowly decreased (**Figure 4.13c**). This indicated that the photoelectrooxidation of methanol over the as-prepared catalyst is better than Pt/C and TiO_2 due to efficient charge transfer and minimum recombination effect of the generated charge carriers.

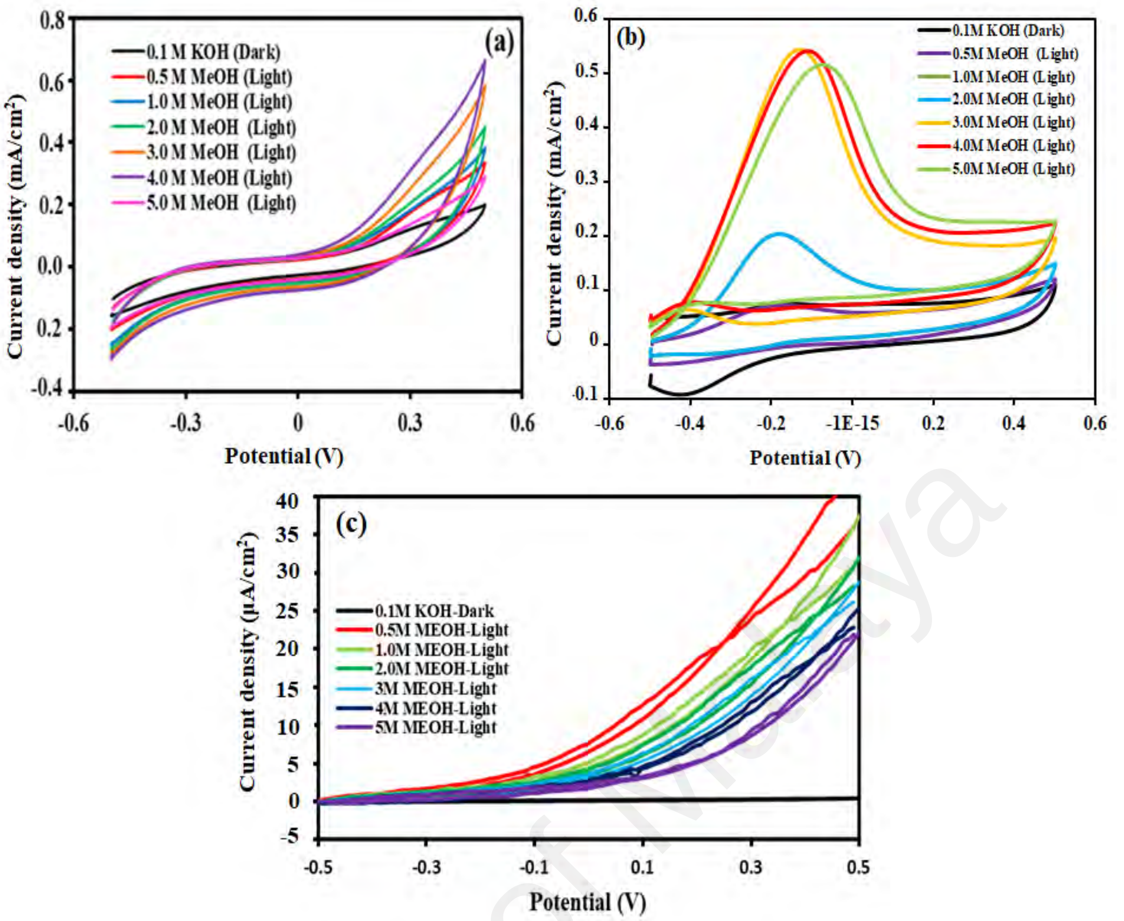

Figure 4.13: Cyclic voltammogram of photoelectrochemical methanol oxidation of thin film at different concentrations in aqueous 0.1 M KOH, 50 mV/s: (a) RuO_2-MnO_2-Co_3O_4 supported TiO_2; (b) Pt/C and (c) TiO_2.

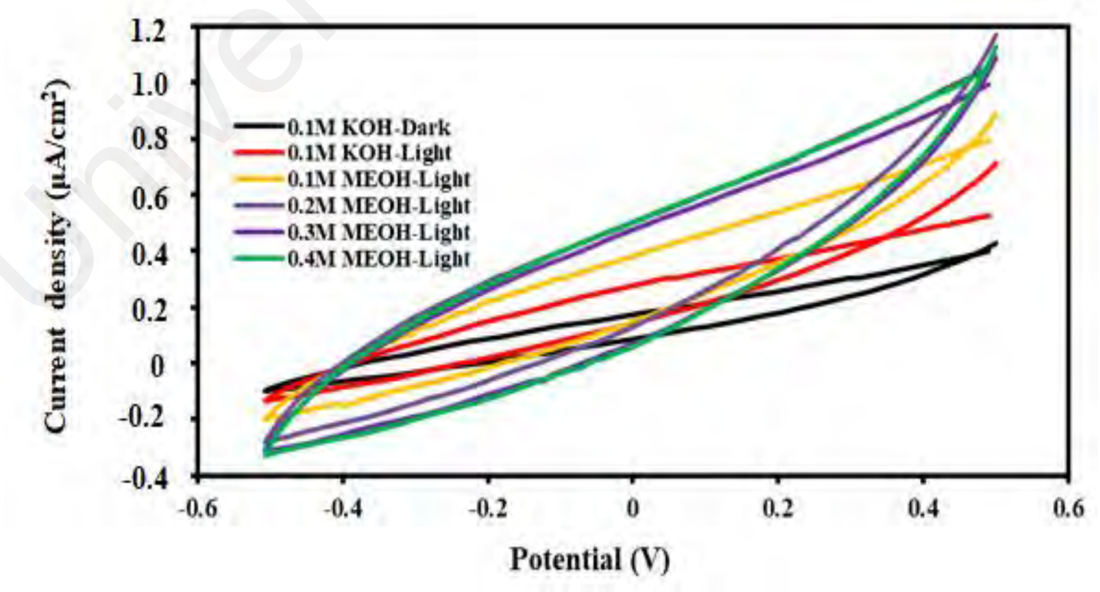

Figure 4.14: Cyclic voltammogram of photoelectrochemical methanol oxidation of anatase TiO_2 at low methanol concentrations in aqueous 0.1 M KOH at 50 mV/s.

The influence of scan rate on the photoelectrochemical currents at 4 M methanol concentration is shown in **Figure 4.15**. The peak current increased as the scan rate increases indicated an efficient charge transfer process across the electrode-electrolyte interface (Ehsan et al., 2015). The stability and reliability of the RuO_2-MnO_2-Co_3O_4 supported TiO_2 towards methanol oxidation was carried out on repeated CV measurements up to 80 cycles, as shown in **Figure 4.16**. After 80 cycles, the photocatalyst showed good stability and sensitivity at around +0.3 V (0.37 mA/cm^2) at the highest methanol concentration of 4 M. From these results, we propose that methanol oxidation could occur through the transport and capture of the electrons at the heterojunction interfaces of RuO_2, Co_3O_4, MnO_2 and TiO_2. Upon illumination by visible light, the excited conduction band electrons of the anatase TiO_2 facilitates the reduction reaction, while the oxidation reaction carried out by the holes in the valence band. The reduction process could occur in two ways. The first is when the dissolved oxygen in the electrolyte absorbs the conduction band electrons to form the oxygen radical anion, which is further reduced to the hydroxyl radical. The second involves the reduction of Ti^{4+} to Ti^{3+}. The Ti^{3+} sites act as an adsorption centre for oxygen, which is further reduced in the same way as the Ru, Mn and Co oxides on the surface (Panayotov et al., 2012). Meanwhile, the valence band holes oxidize the adsorbed water, methanol and hydroxide ion to the hydroxyl and/or methoxy radical, which is further transformed into CO_2 and H_2O (Pradhan et al., 2009).

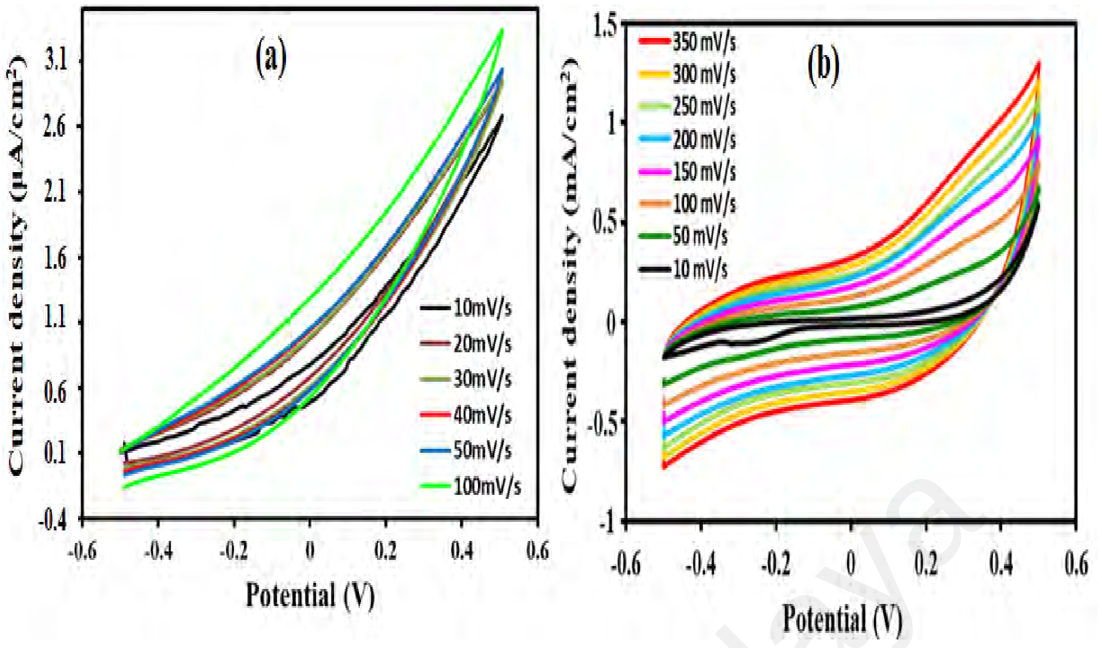

Figure 4.15: Cyclic voltammograms of photoelectrochemical oxidation of (a) commercial anatase TiO_2 in 0.5 M methanol; (b) RuO_2-MnO_2-Co_3O_4 catalyst supported TiO_2 in 4 M methanol at different scan rates in aqueous 0.1 M KOH.

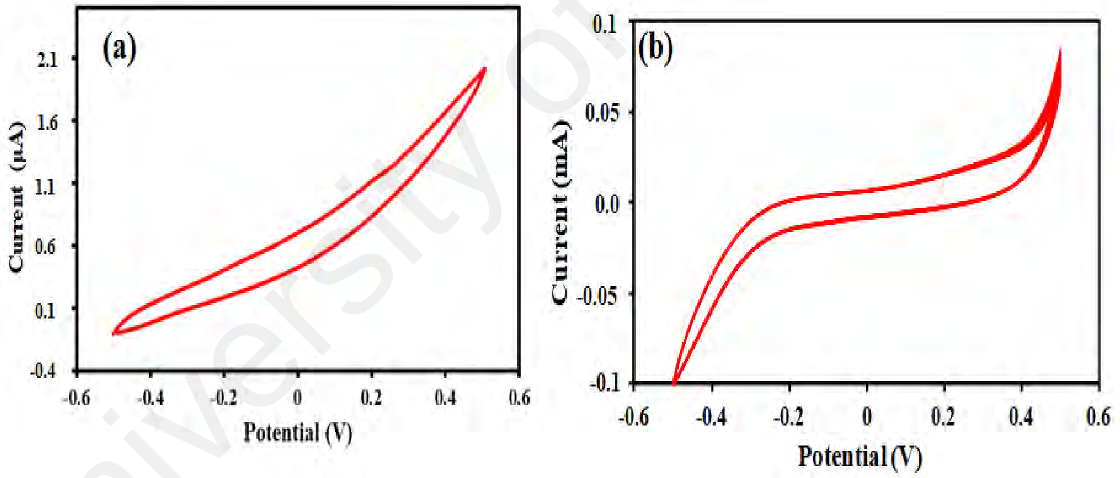

Figure 4.16: Cyclic voltammogram of photoelectrochemical oxidation of (a) 0.5 M methanol of commercial anatase TiO_2; (b) 4 M methanol of RuO_2-MnO_2-Co_3O_4 catalyst supported TiO_2 at 50 mV/s in aqueous 0.1 M KOH for 80 cycles.

The charge transport and recombination process across the semiconductor electrode/electrolyte interface are further investigated by electrochemical impedance spectroscopy (EIS). The Nyquist and Bode phase plots of RuO_2-MnO_2-Co_3O_4 photocatalyst supported TiO_2 (green line) and commercial anatase TiO_2 (black line) deposited on FTO glass were performed in 1 mM $Fe[(CN)_6]^{3-/4-}$ + 0.1 M KCl (1:1) solution in a three electrode system **(Figure 4.17**), recorded between 10 kHz to 0.1 Hz at 5 mV vs. the open circuit potential.

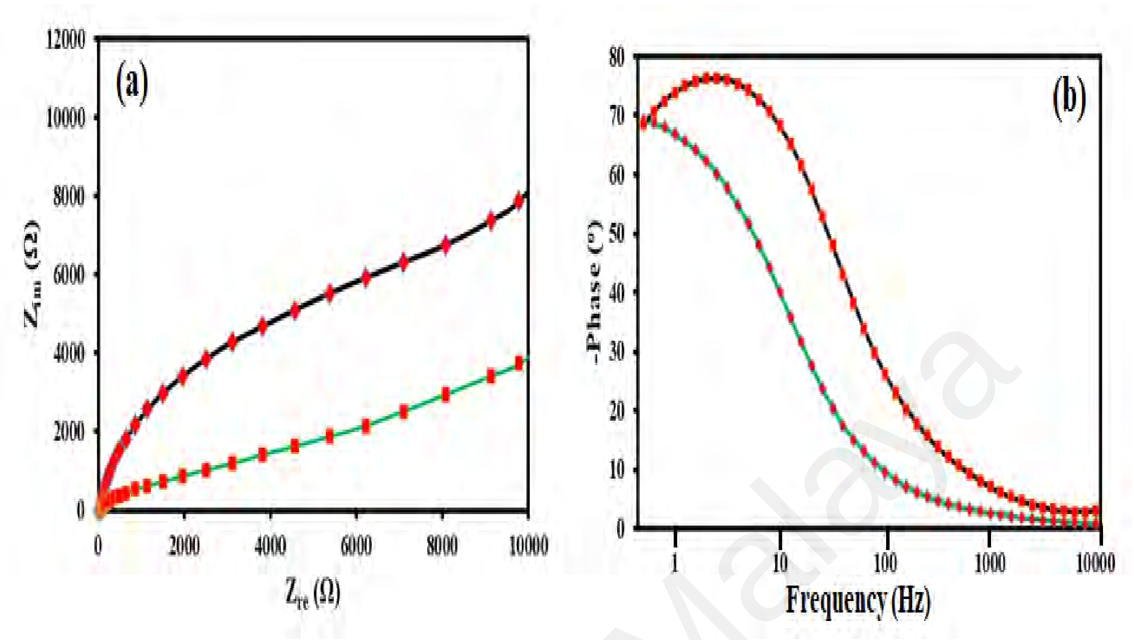

Figure 4.17: (a) Nyquist and (b) Bode phase plots of the impedance spectra recorded on the thin film of RuO_2-MnO_2-Co_3O_4 supported TiO_2 (green line) and commercial TiO_2 (black line) deposited on FTO glass.

The as-prepared trimetallic and Pt/C catalysts show a single semicircle which indicates a simple charge-transfer process across the electrode-electrolyte interface. The electrode potential is the controlling parameter which is in agreement with the concept of electron-hole separation by an external potential bias in a photoelectrochemical degradation reaction (Liu et al., 2000). The EIS diagrams for both electrodes are similar, but differ in the diameters of the two semicircles. The semicircle diameter of the commercial anatase TiO_2 catalyst is larger compared to the as-prepared photocatalyst. The smaller semicircle diameter of the trimetallic RuO_2-MnO_2-Co_3O_4 catalyst is indicative of a lower charge transfer resistance (R_{CT}) which is attributed to the recombination suppression of photogenerated charge carriers, due to the improved charge transport to the electrolyte, better electronic conductivity and conversion efficiency, thus allowing a more rapid degradation reaction to take place (Atta et al., 2011; Liu et al., 2000; Vedarajan et al., 2014). The lifetime of the injected electron, τ_r can be estimated from the equation of $\tau_r = 1/(2\pi f_{\mathrm{max}})$ where f_{max} is the maximum frequency of the mid-frequency peak at the Bode phase plot (Fadadu & Soni, 2013; Kern et al., 2002). The estimated lifetime of the injected electron for the as-prepared catalyst and TiO_2 are 16 and 6.4 ms, respectively. It is evidence that the longer injected electron lifetime in the as-prepared catalyst is indicative of a more active photon-to-current conversion process and a longer injected electron lifetime, where the recombination reaction rate between electrons and holes is lowered. The smaller charge transfer resistance (R_{CT}) and longer injected electron lifetime (τ_r) are the two important features of the as-prepared catalyst which provide the rationalization of a better photocatalytic efficiency.

Upon visible light irradiation, photogenerated electrons will be created and transferred to the respective conduction band and valence band of semiconductors namely RuO_2, Co_3O_4, MnO_2 and TiO_2. The effective alignment of the conduction and valence band in the as-prepared catalyst enable the efficient separation of photogenerated electrons and holes thus, minimizing the recombination effect of electrons and holes. The formation of photogenerated electrons lead to the current increment whereas, the photogenerated holes with high oxidization power result in oxidation of methanol. The effectively transferred electrons will be captured by the surface adsorbed water and oxygen to produce hydroxide ion. In the meantime, the holes will be captured by physisorbed water/hydroxide ion to form hydroxyl radical. The formation of hydroxyl radicals have been regarded as the very important reactive intermediate in the oxidation or decomposition of organic compounds (Dorraj et al., 2018). The hydroxyl radical will further react with surface bonded methanol leading to the production of CO_2 and H_2O.

4.2 Photoelectrochemical reduction of CO_2

4.2.1 RuO_2-MnO_2-Co_3O_4 supported TiO_2

Instead of PEC oxidation of methanol, RuO_2-MnO_2-Co_3O_4 supported TiO_2 also was tested for PEC reduction of CO_2 in aqueous and non-aquoues medium. The outcome of the PEC reduction of CO_2 over RuO_2-MnO_2-Co_3O_4 supported TiO_2 were indicated in aqueous and non-agueous (DMF) were depicted in **Figure 4.18** and **Figure 4.19**. It is well understood that under applied potential with the presence of light illumination in both aqueous and non-aqueous medium, photoelectrons and photoholes will be generated and separated to the respective conduction and valence band. The photogenerated holes will be scavenged by water as sacrificial agent through water oxidation reaction at photoanode to produce O_2 and H_2. Meanwhile, photogenerated electron and H_2 will react by the adsorbed CO_2 molecule to yield $CO_2^{\bullet-}$ as the intermediate reduction product to yield organic compound such as formic acid, methanol and others at counter photocathode. These processes occur simultaneously during the photoelectrochemical reduction of CO_2. In aqueous medium, upon visible light illumination, the onset of photoelectrochemical reduction of CO_2 took place at -0.70 V and reached a maximum photocurrent density of 12.1 μA/cm^2 vs Ag/AgCl as compared to photoelectroreduction in dark condition. The increment of photocurrent upon visible light illumnination as compared to dark condition possibly subsequent from the increase CO_2 reduction product at cathode. Moreover, the photocurrent density of photoelectrochemical reduction of CO_2 in non-aqueous medium is much lower compared to aqueous medium where the presence of 3% H_2O in DMF solution exhibit the highest photocurrent density of 9.3 μA/cm^2. The steady photocurrent density both in aqueous and non-aqueous medium (**Figure 4.20 – 4.21**) suggestive good selectivity of the reduction product which is mainly formic acid as indicated from chronoamperometry analysis.

From the titration method, the amount of dissolved CO_2 in aqueous and DMF medium before photoelectrochemical reduction reaction were 1076 and 1454 ppm, respectively. However, the concentration of CO_2 after 1 h of photoelectrochemical reduction reaction decrease to 882 and 916 ppm which contribute to the formation of 194 and 538 ppm of formic acid in aqueous and DMF medium. This argument was supported by the lower pH value of 3.00 and 4.52 in aqueous and DMF indicative of the formation of acid. The formation of formic acid in aqueous and DMF medium was detected by using GCMS at retention time, R_t of 1.438 minutes which contribute to 18 and 37% of the photoelectrochemical reduction reaction efficiency, respectively. The lower efficiency in aqueous medium compared to DMF most probably due to extensive competition between hydrogen evolution reaction (HER) and carbon dioxide reduction reaction (CDRR) where HER is more favourable reaction as compared to CDRR which lower the overall performance of photocatalyst. Furthermore, the amount of dissolved CO_2 in aqueous medium is much lower than in DMF which further reduced the formation of formic acid.

Based on our previous publication on photoelectrochemical oxidation of methanol into CO_2 and water (Mat et al., 2019), the contemporaneous photocatalyst is suitable and active for both oxidation and reduction reaction and this two reaction are indeed inter-related among each other where if the period of time of photoelectrochmeical reduction of CO_2 is prolonged and/or modification on the method of photoelectrochemical reduction of CO_2, methanol might be able to overcome formic acid as the major product with good yield. Generally, the initial step involve in photoelectrochemical reduction of CO_2 after visible light irradiation was the formation of photogenerated electrons and photogenerated holes. These two reactive species were then separated between each other to prevent charge recombination that might retard the overall performance of the photocatalytic reaction. The photogenerated electron will be captured by the adsorbed CO_2 on the surface of the prepared photocatalyst to produce $CO_2^{\bullet -}$. The proposed reaction mechanism for formic acid production is via the formation of $CO_2^{\bullet -}$ and $^{\bullet}COOH$ as the intermediate species. This is a favourable reaction pathway as reported by Habisreutinger et al. (Habisreutinger et al., 2013). Furthermore, the presence of water in both reaction medium lead to the formation of hydrogen radical ($H^{\bullet}$) as reported previously where the formation of $H^{\bullet}$ might took place in the presence of high dielectric constant solvent such as water (Sasirekha et al., 2006; Subrahmanyam et al., 1999). The following equation summarized the proposed photoelectrochemical reduction of CO_2 over RuO_2-MnO_2-Co_3O_4 catalyst supported anatase to produce formic acid as the major reaction product.

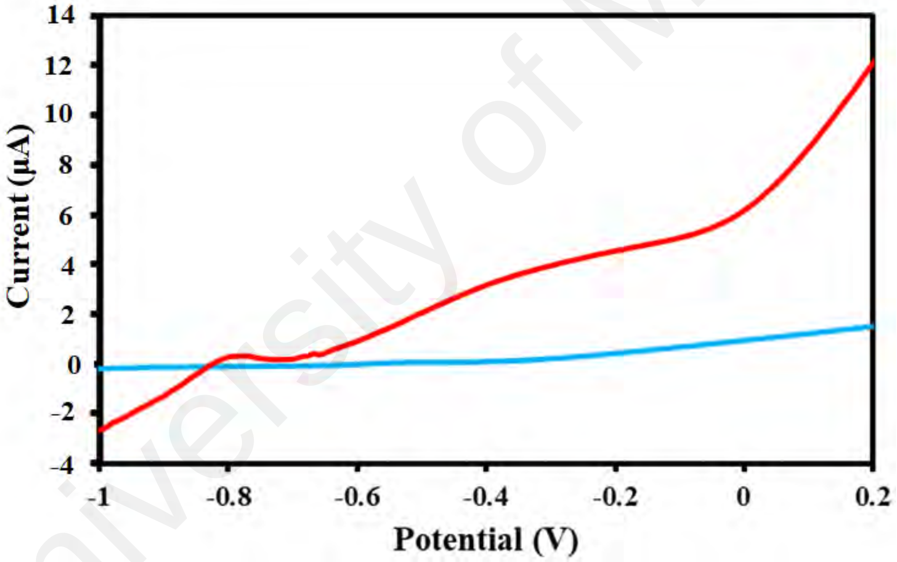

Figure 4.18: LSV of RuO_2-MnO_2-Co_3O_4 catalyst supported TiO_2 in aqueous medium. **Red (**light); **Blue (**dark).

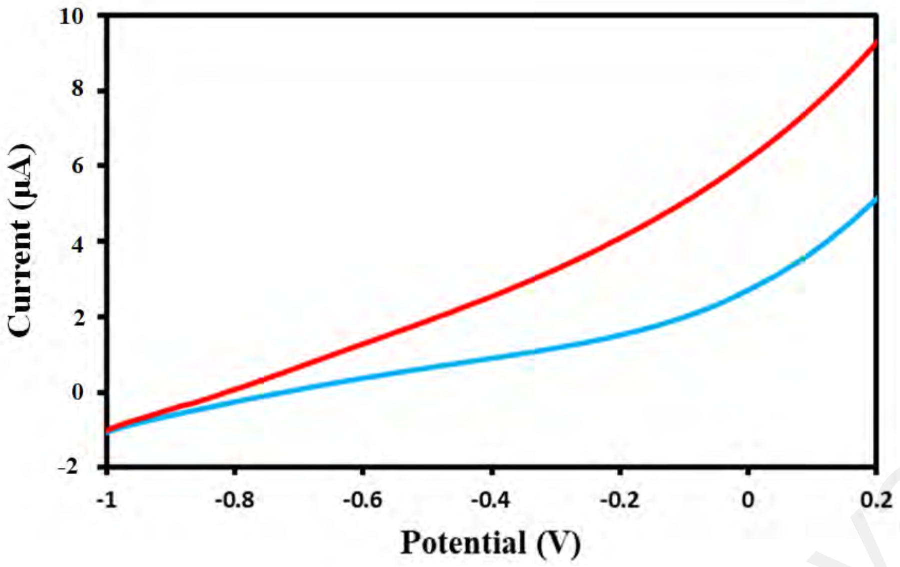

Figure 4.19: LSV of RuO_2-MnO_2-Co_3O_4 catalyst supported TiO_2 in non-aqueous medium. **Red** (light); **Blue** (dark).

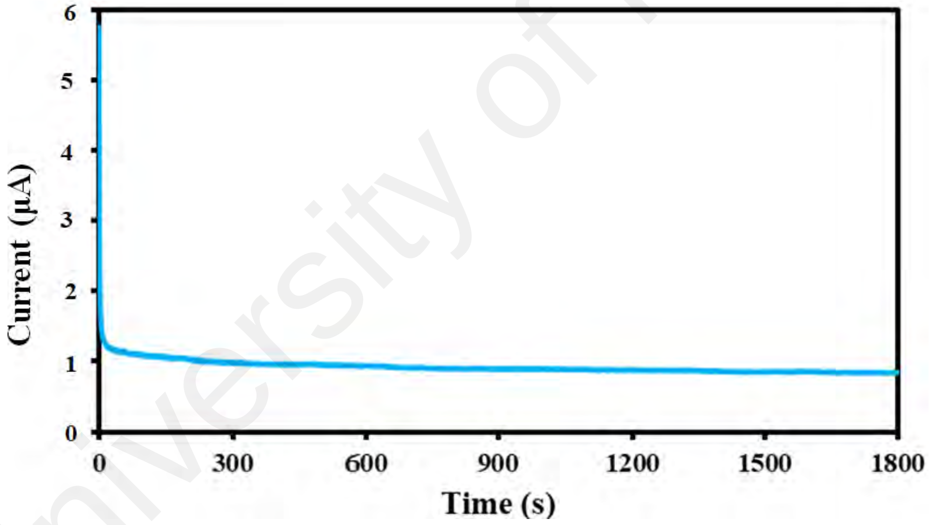

Figure 4.20: Chronoamperometry of RuO_2-MnO_2-Co_3O_4 catalyst supported TiO_2 in aqueous medium.

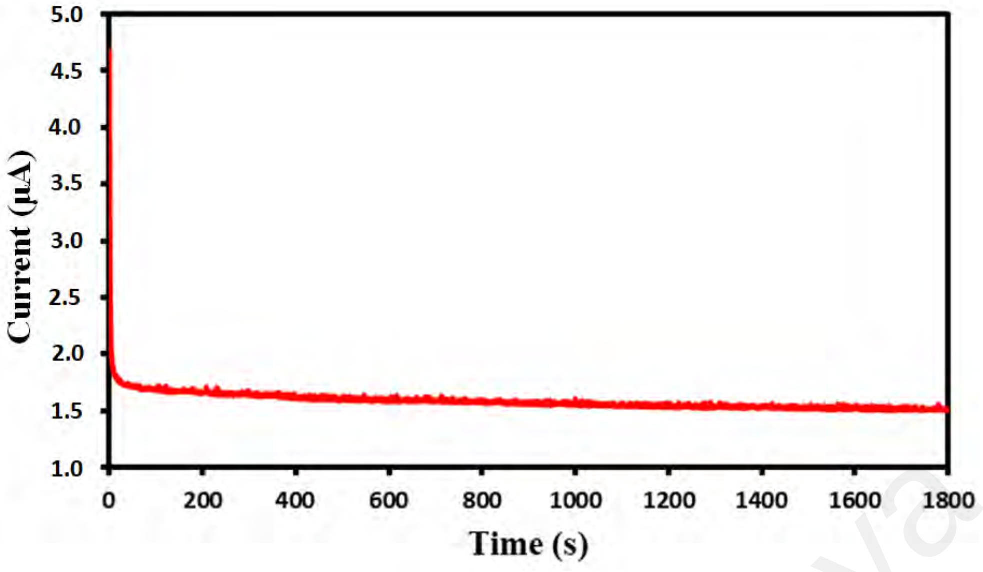

Figure 4.21: Chronoamperometry of RuO_2-MnO_2-Co_3O_4 catalyst supported TiO_2 in DMF+3% H_2O.

4.2.2 Nickel hydroxide

Motivated from the above literatures in **Section 2.7.2** on photocatalytic reduction of CO_2 over $Ni(OH)_2$, it is importance of using $Ni(OH)_2$ in producing valuable organic oxygenates products for the energy generation from CO_2 gas. Mechanism in the formation of higher hydrocarbon than mainly CO as reported before such as formic acid, methanol, ethanol and acethyldehyde in aqueous and DMF will be discussed with better photocurrent density are also reported due to alkalinity of $Ni(OH)_2$ which play significant role in capturing acidic CO_2 thus reducing the gas into valuable chemicals. In addition, the transformation of $Ni(OH)_2$ into NiO after photoelectrochemical reduction of CO_2 play an important role in producing valuable organic product also will be acknowledged as an innovative and novel strategies in this current manuscript.

X-ray powder diffraction analysis from **Figure 4.22** shows that the 2θ of $Ni(OH)_2$ having crystallite size of 11.2 nm was measured by Debye-Scherrer‘s formula $D = K\lambda/\beta \cos\theta$ (where D is the crystallite size; K is a dimensionless constant = 0.94; λ is the X-ray wavelength equal to 1.54056 Å; β is the full-width at half-maximum of the diffraction peak and θ is the diffraction angle. The appearance of β-$Ni(OH)_2$ was observed at peak positions of 19.1°, 33.1°, 38.5°, 51.6°, 59.1°, 62.6°, 69.1° and 72.4° which correspond to (001), (010), (002), (012), (110), (111), (020) and (112) plane, respectively. These arguments were matched very well with theophrastite mineral with crystal system and space group of hexagonal and P-3m1, correspondingly. The other parameters of β-$Ni(OH)_2$ that can be attained from powder x-ray diffraction pattern are $a = b = 3.1300$ Å and $c = 4.6300$ Å while $\alpha = \beta = 90°$ and $\gamma = 120°$ [ICDS code no. 98-002-8101]. After 6 hours of photoelectrochemical reduction of CO_2, some of the $Ni(OH)_2$ are converted into NiO, with the presence of 2θ peak at 45° attributed to the (200) of NiO.

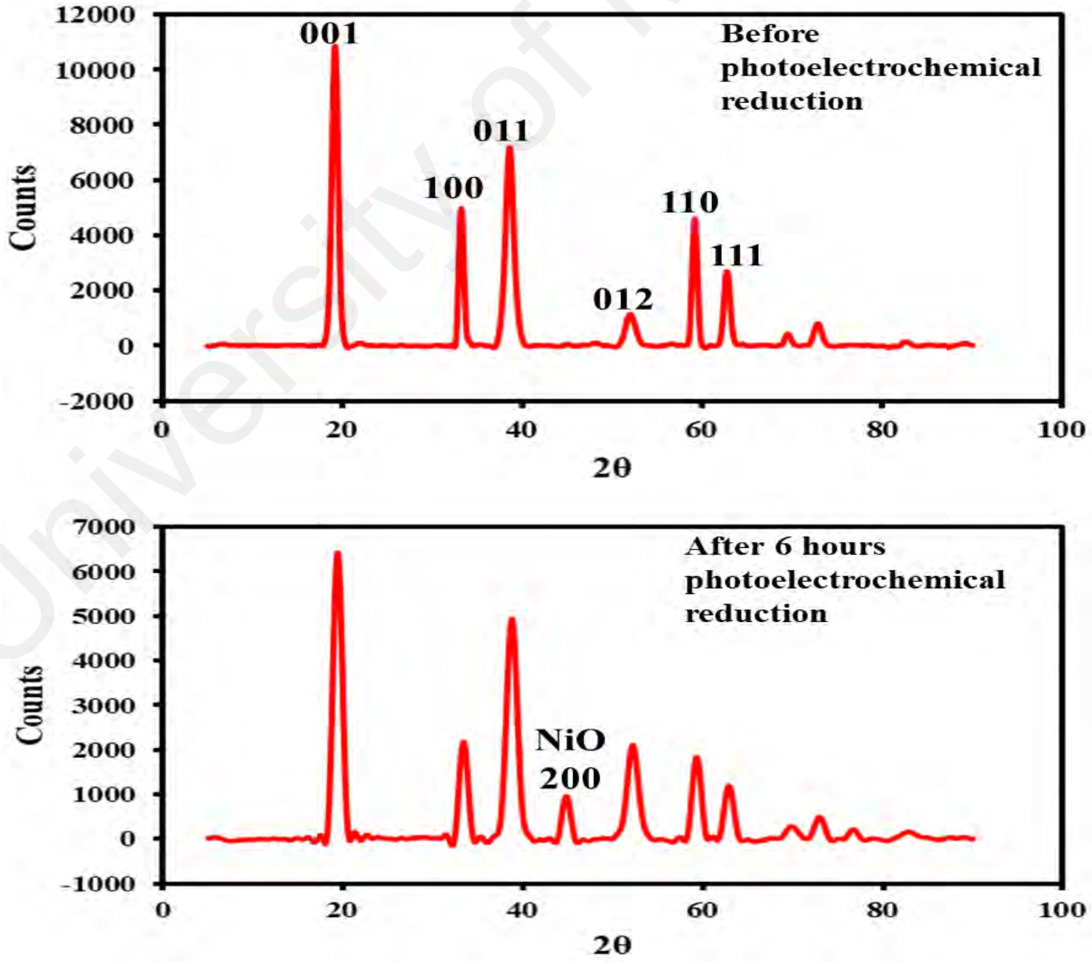

Figure 4.22: XRD spectrum of $Ni(OH)_2$ film before and after 6 hours reaction.

The optical characteristics of the corresponding $Ni(OH)_2$ film can be observed in **Figure 4.23a** which showed a broad visible absorption range from 400 to 800 nm. The calculated band gap of $Ni(OH)_2$ film was 1.3 eV obtained from Tauc‘s plot (**Figure 4.23b**). The absorption of $Ni(OH)_2$ film in the visible light region was very important in harvesting a broader portion of solar light for photochemical reaction proposes. Additionally, the conduction band edge (E_{CB}) and valance band edge (E_{VB}) of $Ni(OH)_2$ were 0.8 and 2.6 eV, respectively.

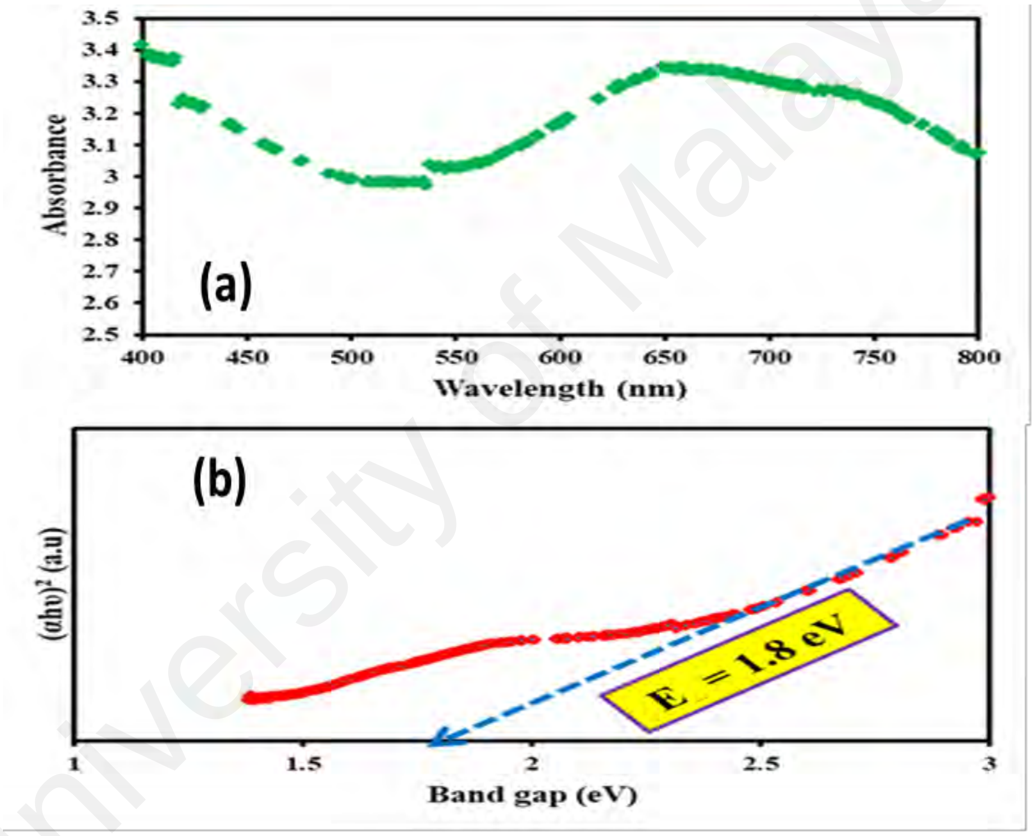

Figure 4.23: (a) UV-Vis spectrum and (b) Tauc‘s plot of $Ni(OH)_2$.

Meanwhile, **Figure 4.24a** showed the photoluminescence spectrum of $Ni(OH)_2$ film. The photoluminescence spectrum of the $Ni(OH)_2$ microparticles which showed three peaks centered at 412, 547 and 677 nm. These peaks can be assigned as the electronic transition of Ni^{2+} ion namely $^1T_{2g}(D) \rightarrow {}^3A_{2g}(F)$ and $^1T_{2g}(D) \rightarrow {}^3T_{2g}(F)$. These values were comparable to the band-gap energy obtained from ultraviolet-vivible measurement of

1.73 eV by Qi et al. (Qi et al., 2009a), which was due to the electronic transition from the $^3A_{2g}$ to $^3T_{2g}$ level. They also reported larger band-gap value of 2.95 and 3.22 eV for nanoplates $Ni(OH)_2$ with thickness of 20-50 nm. The larger band-gap observed is due to the quantum confinement effect when the particle sizes become smaller (De Moura et al., 2011; Lakshminarayana & Buddhudu, 2006; Qi et al., 2009b).

Figure 4.24b indicated five Raman active modes were found in the present study namely positioned at 442, 526, 690, 1040 and 1520 cm^{-1}. The first weak peak and appeared as a shoulder at 442 cm^{-1} was assigned for the translational $E_g(T)$ phonons (Murli et al., 2001) and the second peak at 526 cm^{-1} was due to the harmonic overtone of an acoustic vibration mode which generally more intense indicative of less crystalline material (Hall et al., 2015). The third Raman peak at 690 cm^{-1} in our study is closed to 725 cm^{-1} of brucite [$Mg(OH)_2$]. A broad and medium peak at 1040 cm^{-1} was a signed of the presence of sulphate ion (SO_4^{2-}) from the preparation of $Ni(OH)_2$ (Hall et al., 2012). The final peak at 1520 cm^{-1} appeared to be very weak was apportioned for two magnon transition states arose from anti-ferromagnetism behaviour of NiO at room temperature (Lockwood et al., 1992). However, the FTIR spectrum of $Ni(OH)_2$ (**Figure 4.24c**) over the range of 4000 – 400 cm^{-1} reveals five peaks positioned at 503, 524, 1384, 1631 and 3622 cm^{-1}. The sharp peak at 3622 cm^{-1} is assigned to the stretching vibration of the O–H stretching mode, which is characteristic of free O–H group of the brucite like structure (Liu et al., 2005). This peak indicates the absence of the interlayer water molecules in $Ni(OH)_2$, leading to the vibration of free hydroxyl in the nickel hydroxide. While peak at 1631 cm^{-1} indicate the bending vibration mode of water molecules (Dubal et al., 2012). The presence of carbonate ion, CO_3^{2-} from the interaction with air can be observed at 1384 cm^{-1} (Yu et al., 2012; Yu et al., 2013). While the peaks at 503 and 524 cm^{-1} are attributed to the bending vibration of water molecule and Ni-O(-H) stretching vibration which are the characteristics of $Ni(OH)_2$, respectively (Jeevanandam et al., 2001; Ramesh & Kamath, 2006; Shangguan et al., 2011; Yang et al., 2005; Yu & Lampert, 1987).

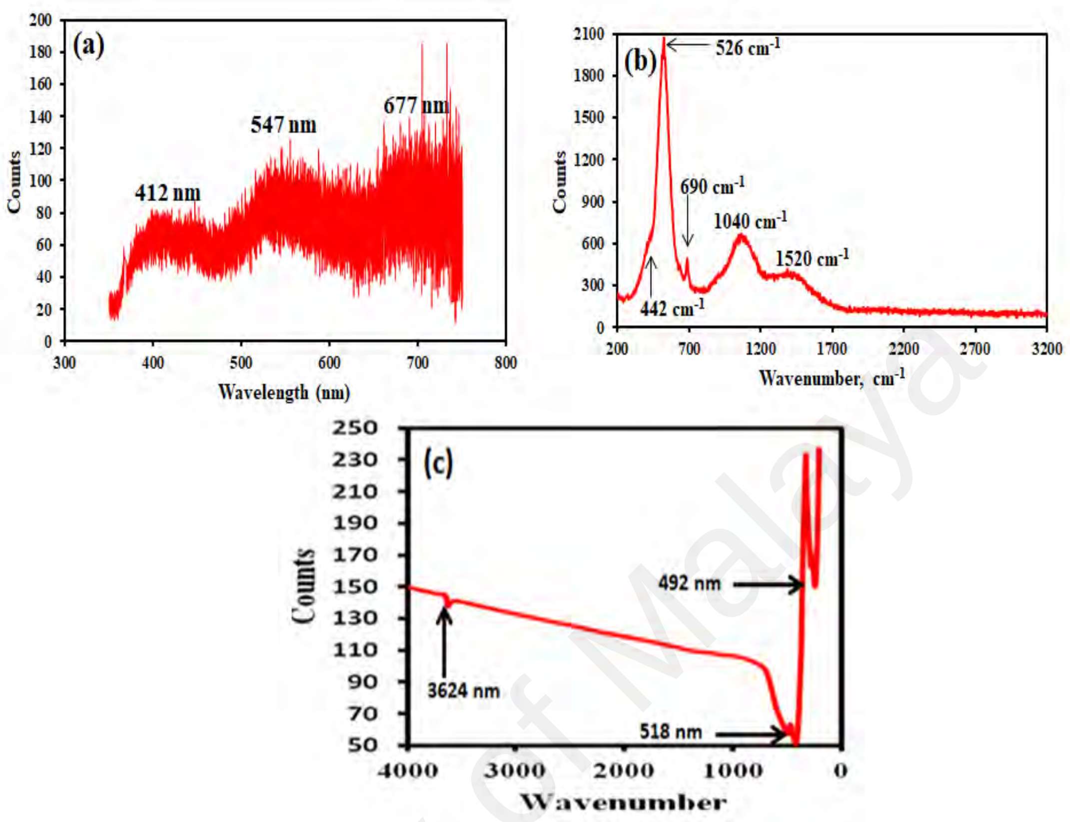

Figure 4.24: (a) PL; (b) Raman and (c) FTIR spectrum of $Ni(OH)_2$.

The elemental compositions and morphology of $Ni(OH)_2$ can be observed in **Figure 4.25 – 4.26**, respectively which designated the occurrence of spherical shape structure. The N_2 absorption-desorption behaviour of sample was showed in **Figure 4.27a**. The sample represents type IV isotherms with an apparent hysteresis loop in the range of 0.5 – 1.0 P/P^o was attained from Brunauer-Deming-Deming-Teller (BDDT) classification, indicating the existence of mesopores (2 – 50 nm). The estimated hysteresis loop for $Ni(OH)_2$ was type H1 suggesting the occurrence of narrow distribution of uniform cylindrical pores (Ma et al., 2014; Zhou et al., 2009). **Figure 4.27b** indicates BET plot of spherical $Ni(OH)_2$ nanoparticles. The surface area of spherical particles of $Ni(OH)_2$ was 18.9 m^2/g calculated by using multipoint BET equation. The pore width distribution calculated from the desorption branch of N_2 isotherms by Barrett-Joyner-Halenda (BJH) method shows the pore width and pore volume of 14.7 nm and 0.02 cm^3/g, respectively, confirming the presence of mesopores (**Figure 4.27c**).

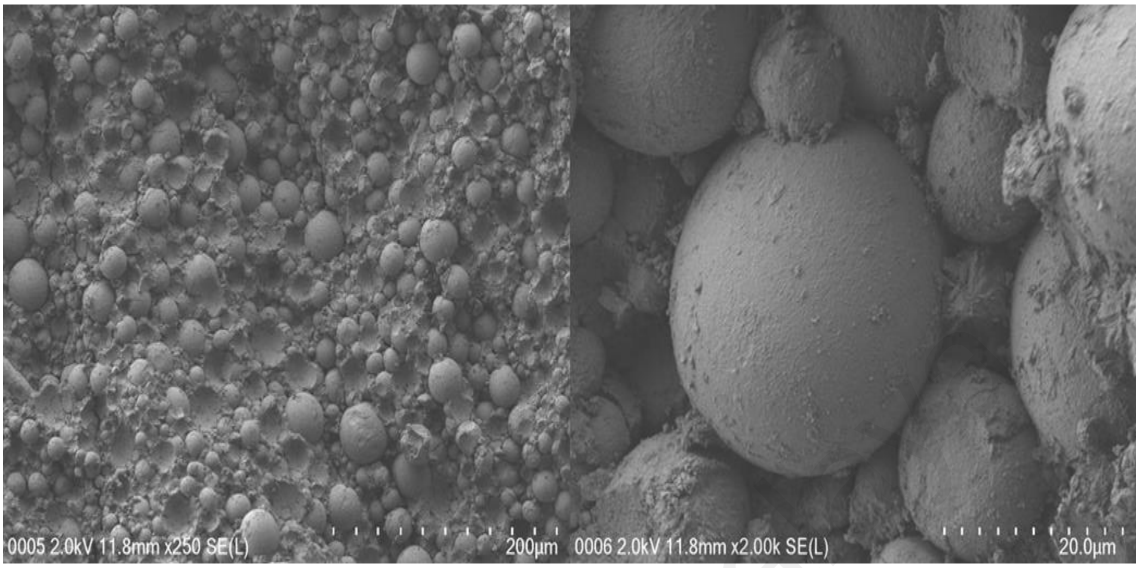

Figure 4.25: FESEM images of $Ni(OH)_2$.

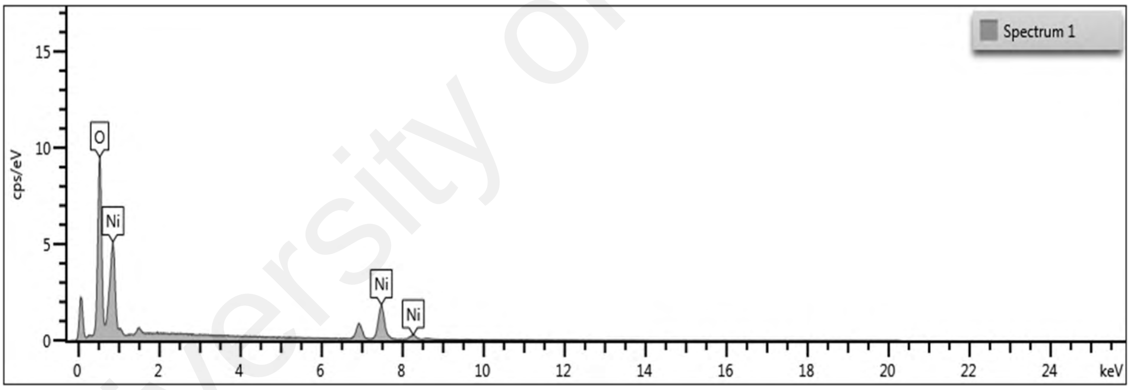

Element	Line Type	Apparent Concentration	k Ratio	Wt%	Wt% Sigma	Atomic %	Standard Label	Factory Standard	Standard Calibration Date
O	K series	7.26	0.02442	36.76	0.34	68.08	SiO2	Yes	
Ni	K series	5.96	0.05961	63.24	0.34	31.92	Ni	Yes	
Total:				100.00		100.00			

Figure 4.26: EDX analysis of $Ni(OH)_2$.

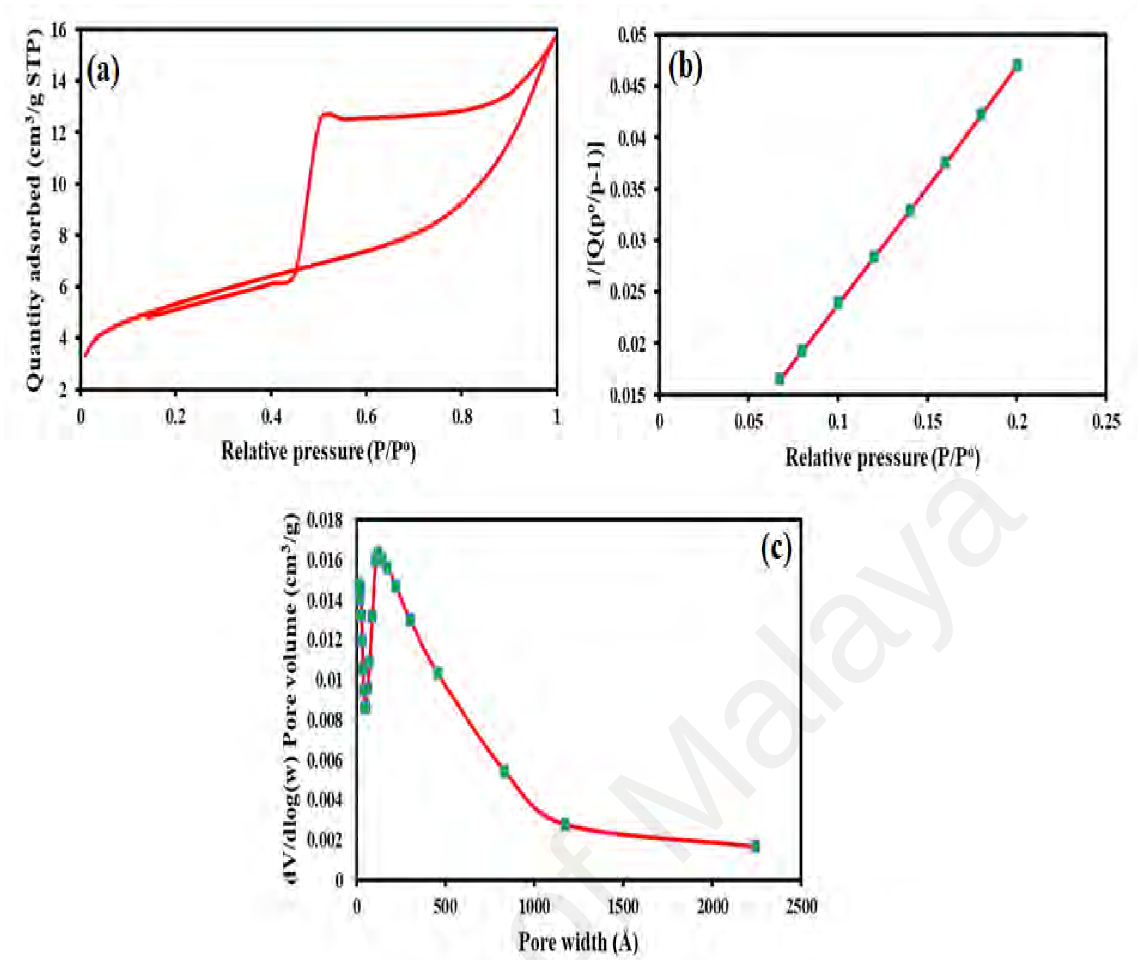

Figure 4.27: (a) Isotherm linear plot; (b) BET surface area plot; (c) BJH pore volume distribution plot of $Ni(OH)_2$.

In aqueous solution, the photoelectrochemical oxidation begins at -0.48 V with a maximum photocurrent density of 24 mA cm^{-2} (0.2 V) under visible light irradiation as compared to the dark condition. While in DMF solution, the photoelectrochemical oxidation starts at -0.61 V. The photocurrent density under visible light irradiation in DMF is maximum at 5 mA cm^{-2} (0.2 V) which is higher than in the dark condition, but still lower than in the aqueous solution. The control experiments were conducted on acetylene black without the presence of CO_2 gas in aqueous and DMF solution. The results showed that without the presence of CO_2, no reduction reaction take place indicative that the products of photoelectrochemical reaction were generated form the reduction of CO_2 and not from any other sources of carbon (**Figure 4.28**). Based on our previous study [33], the fluctuation in voltammetric analysis is indicative of the lower selectivity of the products. Hence, methanol, ethanol and acetaldehyde were detected in this study during chronoamperometry (**Figure 4.29**) in aqueous solution. Meanwhile, the steady photocurrent (**Figure 4.30**) is indicative of the high selectivity of reduction products which is mainly formic acid. The summary of the photoelectrochemical reduction of CO_2 is tabulated in **Table 4.5**.

The amount of dissolved CO_2 in aqueous and DMF are determined before and after the experiment by using titration method as mentioned in experimental section. Before photoelectrochemical reduction of dissolved CO_2, the concentration of CO_2 in aqueous and DMF are 1076 and 1454 ppm, respectively. The concentration of CO_2 after 6 hours of photoelectrochemical reduction (at -0.5 V vs Ag/AgCl) in aqueous and non-aqueous medium decreased to 464 and 600 ppm, respectively. This suggests that 612 ppm and 854 ppm of products were formed during the photoelectrochemical reduction of CO_2 in aqueous and nonaqueous medium, respectively, after 6 hours. It must be mentioned that the pH of the electrolyte also changed after the experiment in both reaction media. After 1 hour bubbling the solution with CO_2, the pH in aqueous and DMF are 3.82 and 8.83, respectively. However, after 6 hours of photoelectrochemical reduction, the pH of the solution changed to 7.47 and 5.83, in aqueous and DMF solution, respectively. This indicates that the increment in pH reading is due to the conversion of formic acid into alcohols and acetaldehyde in aqueous solution, while the major product formed during the photoelectrochemical reduction of CO_2 in DMF medium is formic acid, detected by GCMS. After 6 hours of photoelectrochemical reduction reaction in aqueous solution, methanol as the major product and ethanol as the minor product were detected at R_t of 1.3 minutes. The major reduction product in aqueous solution is acetaldehyde with an efficiency of 77% (471 ppm) at R_t of 1.5 and 1.7 minutes. The slight increase in pH of the aqueous solution after 6 hours of photoelectrochemical reduction is due to the formation of methanol, ethanol and acetaldehyde from the loss of formic acid as the early intermediate. The formation of ethanol and acetaldehyde from an aqueous medium indicates that the $Ni(OH)_2$ is a suitable photoelectrocatalyst for the production of organic compounds with slightly higher carbon content. It is suggested that the formation of methanol is due to the further reduction of formic acid, while the formation of higher carbon compounds such as ethanol and acetaldehyde is unclear.

Meanwhile, formic acid appears at R_t of 1.487 minutes during the photoelectrochemical reduction of CO_2 in DMF. The formation of ethanol in DMF was not detected even after 6 hours reaction due to the low amount of water (3%) content in the reaction medium, in addition to the competition with the hydrogen evolution reaction (HER) from water oxidation and the re-oxidation of product into CO_2. Therefore, formic acid is the major product from photoelectrochemical reduction of CO_2 in DMF. The photochemical reduction mechanism of CO_2 to produce formic acid and methanol is still unclear. There are two mechanisms which describe the reduction of CO_2, namely the formaldehyde pathway (Ji & Luo, 2016) and carbene pathway (Nea u et al., 2014). Ji et al. (Ji & Luo, 2016) proposed that formic acid and formaldehyde could be formed according to the formaldehyde pathway which is thermodynamically feasible (Mao et al., 2013) and these products could be desorbed from the surface of catalyst into the solution upon the reduction reaction (Habisreutinger et al., 2013; Zhang et al., 2018). The formation of photogenerated electron-hole pairs as the major charge carriers occurs upon visible light irradiation on the surface of $Ni(OH)_2$ photoanode. The electrons with higher energy than the band gap of $Ni(OH)_2$ will be promoted to the conduction band while leaving the photogenerated holes in the valence band. Generally, the initial step of activation of dissolved CO_2 in the solution for most semiconductors is the formation of $^{\bullet}CO_2^{-}$ radical anion after accepting an electron from the conduction band (Gattrell et al., 2006; White et al., 2015). In **Pathway 1**, we proposed the involvement of hydroxyl radical ($OH^{\bullet}$) from the oxidation reaction of water producing

H^+ and OH^-. The adsorption of $^{\bullet}CO_2^-$ by means of monodentate binding is through one of the oxygen atom or carbon atom which favours the formation of the hydroxyformyl radical ($^{\bullet}COOH$) (Gattrell et al., 2006). Further reaction between $^{\bullet}COOH$ and OH- in the presence of water yielded formic acid. In **Pathway 2**, after the generation of $CO_2^{\bullet -}$, the free hydrogen atom ($^{\bullet}H$) originates from the reduction of proton by the conduction band electron will further react with hydroxyformyl radical to yield formic acid (Sasirekha et al., 2006; Subrahmanyam et al., 1999). The proposed reaction mechanism for formic acid production is via the formation of $^{\bullet}CO_2^-$ and $^{\bullet}COOH$ as the intermediate species. This is a favourable reaction pathway as reported by Habisreutinger *et al.* (Habisreutinger et al., 2013), since the CO_2 reduction in this study proceeds in a high dielectric medium such as aqueous solution. The proposed reaction mechanism for the formation of formic acid as the major CO_2 reduction are shown in **Figure 4.31** (Habisreutinger et al., 2013).

On the other hand, from the XRD results, after 6 hours of photoelectrochemical reduction reaction, some of the $Ni(OH)_2$ was transformed into NiO (JCPDS #47-1049) with a distinct peak at 44°. The water content in $Ni(OH)_2$ is an important source for the CO_2 reduction to release formic acid. Hence, $Ni(OH)_2$ in the present study can be suggested as the suitable candidate for CO_2 reduction reaction into valuable organic oxygenates.

The production of methanol is the result of further reduction of formic acid while the production of acetaldehyde and ethanol is most probably due to the reduction of acetic acid (eq. 16, although undetected by GCMS after 6 hours), which is accompanied by the increase in pH. The production of ethanol and acetaldehyde is unclear, but nevertheless, the combination of formic acid and $\bullet CO_2^-$ radical anion could be the major step in the formation of acetaldehyde and ethanol.

The presence of reductants such as the conduction band electrons (CB_e^-), H^+, water and $Ni(OH)_2$ could play a major role in the further reduction to eliminate the oxygen atoms to produce ethanol and acetaldehyde in aqueous solution.

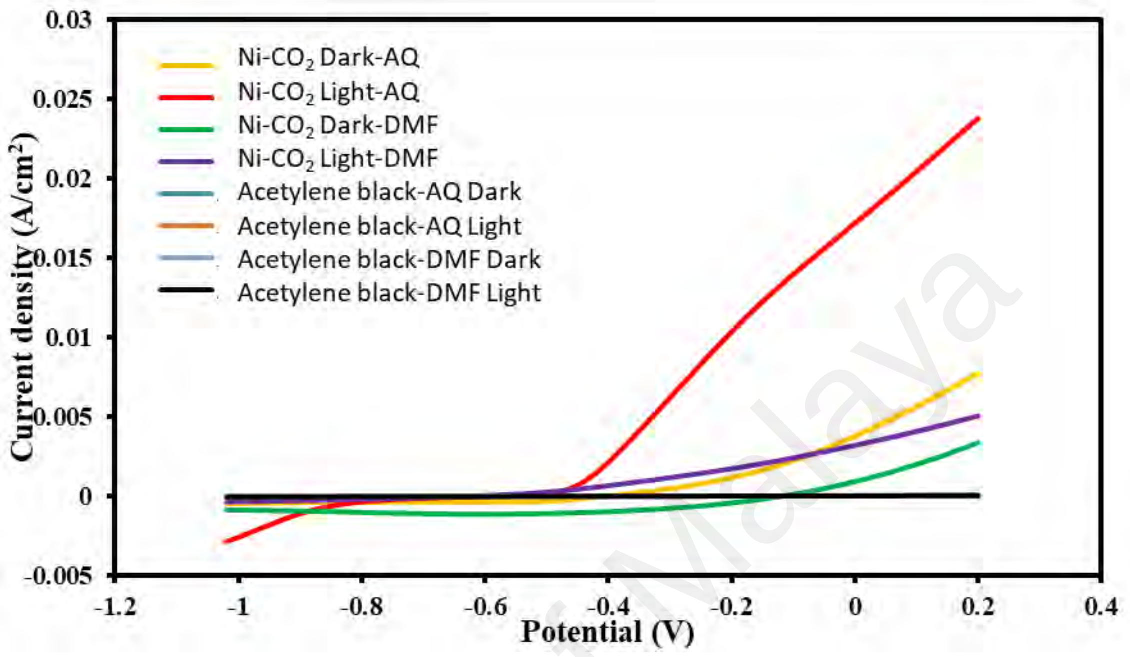

Figure 4.28: LSV measurement of PEC reduction of CO_2 over $Ni(OH)_2$ and acetylene black in aqueous and DMF solution.

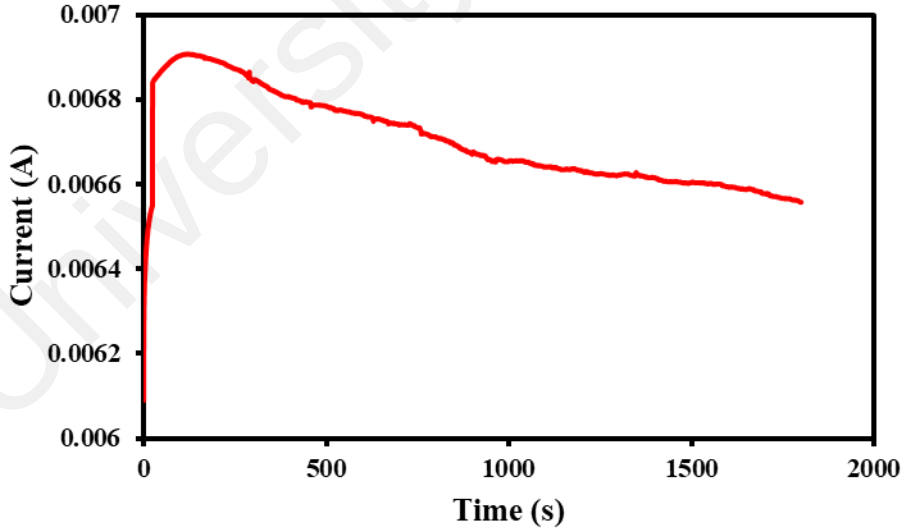

Figure 4.29: CA of $Ni(OH)_2$ in aqueous solution.

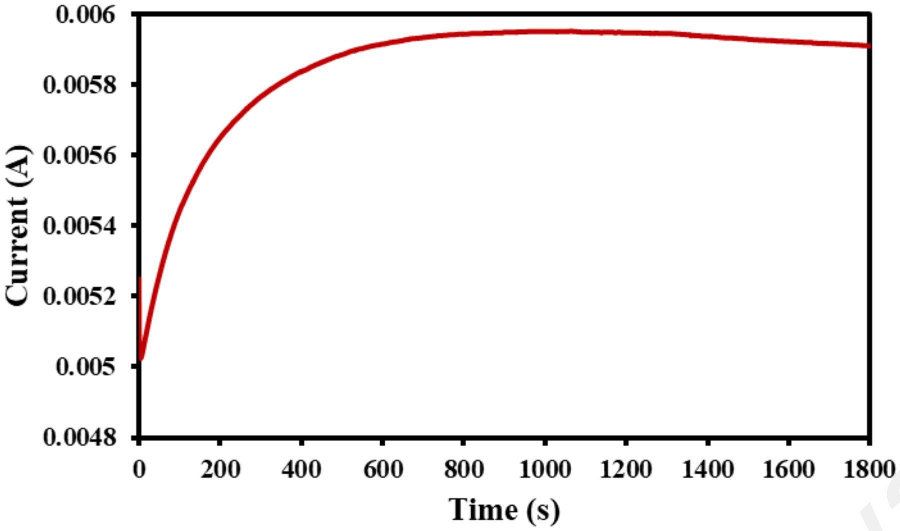

Figure 4.30: CA of $Ni(OH)_2$ in DMF solution.

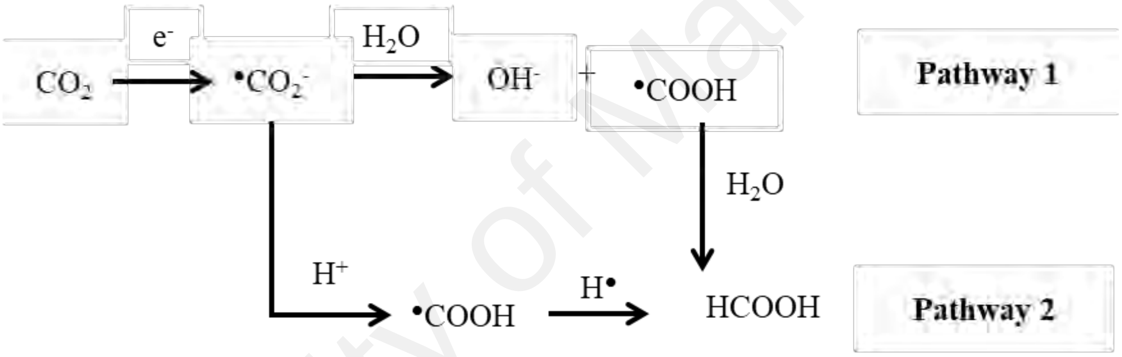

Figure 4.31: Proposed reaction mechanism of photoelectrochemical reduction of CO_2 over $Ni(OH)_2$.

Table 4.5: Summary of photoelectrochemical reduction studies of CO_2 in aqueous and non-aqueous medium.

Photoelectroreduction of CO_2 in aqueous 0.2 M $LiClO_4$ solution.	**Photoelectrochemical reduction of CO_2 in 0.2 M $LiClO_4$ in DMF + 3% H_2O solution.**
Concentration of CO_2 after 1 hour bubbling: 1076 ppm	Concentration of CO_2 after 1 hour bubbling: 1454 ppm
Concentration of CO_2 after 6 hours reduction reaction: 464 ppm	Concentration of CO_2 after 6 hours reduction reaction: 600 ppm
pH before bubbling CO_2: 3.82	pH before bubbling CO_2: 8.83
pH after 6 hours reduction reaction: 7.47	pH after 6 hours reduction reaction: 5.83
Photocurrent density: 24 mA/cm^2	Photocurrent density: 5 mA/cm^2
Major Product: Acetyldehyde, methanol	Major product: Formic acid
Minor Product: Ethanol	Minor product: methanol

CHAPTER 5: CONCLUSIONS AND FUTURE OUTLOOK

Trimetallic (RuO_2-MnO_2-Co_3O_4) catalyst supported on anatase TiO_2 was synthesized by a co-precipitation method and tested for the photoelectrochemical oxidation of methanol at room temperature under atmospheric pressure. It was found that the presence of oxygen vacancies during the catalyst pre-treatment under H_2 atmosphere allowed the diffusion of Ru, Mn and Co into the TiO_2 lattice, forming structural defects which are responsible for the shift in optical absorption into the visible region of 400 - 800 nm, hence decreased the band gap of anatase TiO_2 to 1.66 eV. Further photoluminescence study depicts that the recombination rate of the as-prepared catalyst is significantly suppressed as compared to the unmodified anatase TiO_2 due to presence of oxygen vacancies, which act as an electron sink for the efficient separation of the photogenerated charge carriers. The as-prepared catalyst was more efficient in the photoelectrochemical oxidation of methanol at higher concentration which oxidized 4 M methanol at 0.3V at 0.37 mA/cm^2, compared to Pt/C which oxidized 3 M at -0.12 V and 0.54 mA/cm^2. This result indicates that the trimetallic Ru-Mn-Co anatase supported catalyst can be a suitable substitute for the replacement of precious metal catalysts for DMFC energy generation.

The photoelectrochemical reduction of CO_2 in visible region has been studied in aqueous and non-aqueous medium by using a trimetallic photocatalyst of RuO_2-MnO_2-Co_3O_4 supported anatase TiO_2 was successfully synthesized by precipitation method and tested for photoelectrochemical reduction of CO_2 into formic acid. $CO_2^{\bullet -}$ and $^{\bullet}COOH$ were the major reactive radicals that lead to the formation of formic acid. The aqueous medium lead to lower amount of formic acid due to extensive competition between HER and low solubility of CO_2 which contribute only 18% of the efficiency. The steady photocurrent obtained from chronoamperometry indicative of good selectivity of the final product where formic acid remain the major product in both aqueous and DMF medium. Other product such as methanol is expected to form but in small amount as a minor product.

The spherical $Ni(OH)_2$ was successfully developed by using hydrothermal method showed the band gap energy of 1.8 eV is indeed very important in harvesting visible light for better photoelectrocatalytic activity. The high photocurrent density of 24 mA/cm^2 was obtained in aqueous solution of 0.2 M $LiClO_4$ as compared to 5 mA/cm^2 in DMF solution. The product efficiency was 77% and 59% in aqueous and DMF, respectively. Apart from the formation of $^{\bullet}CO_2^-$ radical anion as the intermediate species for the dissolved CO_2 reduction in both aqueous and non-aqueous medium, the presence of OH group from the transformation of $Ni(OH)_2$ was paramount important for the production of organic oxygenates such as ethanol and acetaldehyde. In brief, as for the future recommendations in order to minimize competitive reaction between water splitting and CO_2 reduction reaction, the experiment can be conducted in non-aquoeus solution at low temperature and neutral pH. Furthermore, methanol and amine such as triethanolamine can be used as hydrogen source instead of water for CO_2 reduction reaction, thus will reduce the competitive reaction between water splitting and CO_2 reduction reaction. Various photocatalysts not only limited to metal oxides but also sulphides, oxynitrides, nitrides, polyoxometalates and metal organic frameworks. will be developed and studied thoroughly by the improvement of the current synthetic method such as by using electrochemical deposition method, electric field assisted chemical vapour deposition (EFACVD) and aerosol assisted chemical vapour deposition (AACVD) from various metal precursors, experimental condition (pH, solvent, concentration, temperature and pressure, sacrificial agents) and materials characterizations for further understanding on the fundamental of photochemical reaction. Laboratory set-up such as apparatus for EFACVD, AACVD, electrochemical cell and light source will be developed in a better way than the current set-up. The photoelectrochemical studies will be widen not only towards CO_2 reduction but also water splitting, degradation of organic pollutant and N_2 reduction reaction. The bi and tri layered stacks of these ceramic thin films will be developed to enhance photoelectrochemical efficiency. Last but not least, engangement with experienced researchers in the field of electrochemistry and photoelectrochemistry will be developed in the future.

REFERENCES

Abe, T., Tanizawa, M., Watanabe, K., & Taguchi, A. (2009). CO_2 methanation property of Ru nanoparticle-loaded TiO_2 prepared by a polygonal barrel-sputtering method. *Energy & Environmental Science, 2*(3), 315-321.

Abida, B., Chirchi, L., Baranton, S., Napporn, T. W., Kochkar, H., Léger, J.-M., & Ghorbel, A. (2011). Preparation and characterization of Pt/TiO_2 nanotubes catalyst for methanol electro-oxidation. *Applied Catalysis B: Environmental, 106*(3-4), 609-615.

Acharya, R., Subbaiah, T., Anand, S., & Das, R. (2003). Effect of precipitating agents on the physicochemical and electrolytic characteristics of nickel hydroxide. *Materials Letters, 57*(20), 3089-3095.

Ahmed, A. Y., Kandiel, T. A., Oekermann, T., & Bahnemann, D. (2011). Photocatalytic activities of different well-defined single crystal TiO_2 surfaces: Anatase versus rutile. *The Journal of Physical Chemistry Letters, 2*(19), 2461-2465.

Akhade, S. A., Luo, W., Nie, X., Bernstein, N. J., Asthagiri, A., & Janik, M. J. (2014). Poisoning effect of adsorbed CO during CO_2 electroreduction on late transition metals. *Physical Chemistry Chemical Physics, 16*(38), 20429-20435.

Akple, M. S., Low, J., Qin, Z., Wageh, S., Al-Ghamdi, A. A., Yu, J., & Liu, S. (2015). Nitrogen-doped TiO_2 microsheets with enhanced visible light photocatalytic activity for CO_2 reduction. *Chinese Journal of Catalysis, 36*(12), 2127-2134.

Alavi, B., Aghajani, H., & Rasooli, A. (2019). Electrophoretic deposition of electroless nickel coated YSZ core-shell nanoparticles on a nickel based superalloy. *Journal of the European Ceramic Society, 39*(7), 2526-2534.

Albo, J., Alvarez-Guerra, M., Castaño, P., & Irabien, A. (2015). Towards the electrochemical conversion of carbon dioxide into methanol. *Green Chemistry, 17*(4), 2304-2324.

Alfaifi, B. Y., Ullah, H., Alfaifi, S., Tahir, A. A., & Mallick, T. K. (2018). Photoelectrochemical solar water splitting: From basic principles to advanced devices. *Veruscript Functional Nanomaterials, 2*, 1-26.

Aljabour, A., Coskun, H., Apaydin, D. H., Ozel, F., Hassel, A. W., Stadler, P., . . . Kus, M. (2018). Nanofibrous cobalt oxide for electrocatalysis of CO_2 reduction to carbon monoxide and formate in an acetonitrile-water electrolyte solution. *Applied Catalysis B: Environmental, 229*, 163-170.

Almquist, C. B., & Biswas, P. (2002). Role of synthesis method and particle size of nanostructured TiO_2 on its photoactivity. *Journal of Catalysis, 212*(2), 145-156.

Alstrum-Acevedo, J. H., Brennaman, M. K., & Meyer, T. J. (2005). Chemical approaches to artificial photosynthesis. 2. *Inorganic Chemistry, 44*(20), 6802-6827.

Amatore, C., & Saveant, J. M. (1981). Mechanism and kinetic characteristics of the electrochemical reduction of carbon dioxide in media of low proton availability. *Journal of the American Chemical Society, 103*(17), 5021-5023.

Amir, F. Z., Pham, V., Mullinax, D., & Dickerson, J. (2016). Enhanced performance of HRGO-RuO_2 solid state flexible supercapacitors fabricated by electrophoretic deposition. *Carbon, 107*, 338-343.

Anitha, V., Zazpe, R., Krbal, M., Yoo, J., Sopha, H., Prikryl, J., . . . Macak, J. M. (2018). Anodic TiO_2 nanotubes decorated by Pt nanoparticles using ALD: An efficient electrocatalyst for methanol oxidation. *Journal of Catalysis, 365*, 86-93.

Anpo, M., Yamashita, H., Ichihashi, Y., & Ehara, S. (1995). Photocatalytic reduction of CO_2 with H_2O on various titanium oxide catalysts. *Journal of Electroanalytical Chemistry, 396*(1-2), 21-26.

Antolini, E. (2010). Composite materials: an emerging class of fuel cell catalyst supports. *Applied Catalysis B: Environmental, 100*(3-4), 413-426.

Antolini, E., & Gonzalez, E. (2009). Ceramic materials as supports for low-temperature fuel cell catalysts. *Solid State Ionics, 180*(9-10), 746-763.

Argüello, J. A., Rojo, J. M., & Moreno, R. (2019). Electrophoretic deposition of manganese oxide and graphene nanoplatelets on graphite paper for the manufacture of supercapacitor electrodes. *Electrochimica Acta, 294*, 102-109.

Arsov, L. D., Kormann, C., & Plieth, W. (1991). Electrochemical synthesis and in situ Raman spectroscopy of thin films of titanium dioxide. *Journal of Raman Spectroscopy, 22*(10), 573-575.

Askari, M. B., Salarizadeh, P., Seifi, M., & Rozati, S. M. (2019). Ni/NiO coated on multi-walled carbon nanotubes as a promising electrode for methanol electro-oxidation reaction in direct methanol fuel cell. *Solid State Sciences, 97*, 106012-106018.

Ata, M. S., Poon, R., Syed, A. M., Milne, J., & Zhitomirsky, I. (2018). New developments in non-covalent surface modification, dispersion and electrophoretic deposition of carbon nanotubes. *Carbon, 130*, 584-598.

Atta, N. F., Amin, H. M., Khalil, M. W., & Galal, A. (2011). Nanotube arrays as photoanodes for dye sensitized solar cells using metal phthalocyanine dyes. *International Journal of Electrochemical Science, 6*, 3316-3332.

Avcı, C., Aydın, A., Tuna, Z., Yavuz, Z., Yamauchi, Y., Suzuki, N., & Dag, O. M. (2014). Molten salt assisted self assembly (MASA): Synthesis of mesoporous metal titanate ($CoTiO_3$, $MnTiO_3$, and $Li_4Ti_5O_{12}$) Thin Films and Monoliths. *Chemistry of Materials, 26*(20), 6050-6057.

Bahnemann, W., Muneer, M., & Haque, M. M. (2007). Titanium dioxide-mediated photocatalysed degradation of few selected organic pollutants in aqueous suspensions. *Catalysis Today, 124*(3-4), 133-148.

Bailón-García, E., Carrasco-Marín, F., Pérez-Cadenas, A. F., & Maldonado-Hódar, F. J. (2015). Influence of the pretreatment conditions on the development and performance of active sites of Pt/TiO_2 catalysts used for the selective citral hydrogenation. *Journal of Catalysis, 327*, 86-95.

Balu, S., Velmurugan, S., Palanisamy, S., Chen, S.-W., Velusamy, V., Yang, T. C., & El-Shafey, E.-S. I. (2019). Synthesis of α-Fe_2O_3 decorated g-C_3N_4/ZnO ternary Z-scheme photocatalyst for degradation of tartrazine dye in aqueous media. *Journal of the Taiwan Institute of Chemical Engineers, 99*, 258-267.

Bamwenda, G. R., Tsubota, S., Nakamura, T., & Haruta, M. (1995). Photoassisted hydrogen production from a water-ethanol solution: a comparison of activities of Au/TiO_2 and Pt/TiO_2. *Journal of Photochemistry and Photobiology A: Chemistry, 89*(2), 177-189.

Bandi, A. (1990). Electrochemical reduction of carbon dioxide on conductive metallic oxides. *Journal of The Electrochemical Society, 137*(7), 2157-2160.

Bandi, A., & Kühne, H. M. (1992). Electrochemical reduction of carbon dioxide in water: analysis of reaction mechanism on ruthenium-titanium-oxide. *Journal of The Electrochemical Society, 139*(6), 1605-1610.

Barakat, N. A., Abdelkareem, M. A., & Kim, H. Y. (2013). Ethanol electro-oxidation using cadmium-doped cobalt/carbon nanoparticles as novel non precious electrocatalyst. *Applied Catalysis A: General, 455*, 193-198.

Bard, A. J. (1979). Photoelectrochemistry and heterogeneous photo-catalysis at semiconductors. *Journal of Photochemistry, 10*(1), 59-75.

Barrera, E., González, I., & Viveros, T. (1998). A new cobalt oxide electrodeposit bath for solar absorbers. *Solar Energy Materials and Solar Cells, 51*(1), 69-82.

Barsan, N., & Weimar, U. (2001). Conduction model of metal oxide gas sensors. *Journal of Electroceramics, 7*(3), 143-167.

Barton Cole, E., Lakkaraju, P. S., Rampulla, D. M., Morris, A. J., Abelev, E., & Bocarsly, A. B. (2010). Using a one-electron shuttle for the multielectron reduction of CO_2 to methanol: kinetic, mechanistic, and structural insights. *Journal of the American Chemical Society, 132*(33), 11539-11551.

Baruah, B., & Kumar, A. (2018). PEDOT: PSS/MnO_2/rGO ternary nanocomposite based anode catalyst for enhanced electrocatalytic activity of methanol oxidation for direct methanol fuel cell. *Synthetic Metals, 245*, 74-86.

Baştan, F. E., Rehman, M. A. U., Avcu, Y. Y., Avcu, E., Üstel, F., & Boccaccini, A. R. (2018). Electrophoretic co-deposition of PEEK-hydroxyapatite composite coatings for biomedical applications. *Colloids and Surfaces B: Biointerfaces, 169*, 176-182.

Basu, R. N., Randall, C. A., & Mayo, M. J. (2001). Fabrication of dense zirconia electrolyte films for tubular solid oxide fuel cells by electrophoretic deposition. *Journal of the American Ceramic Society, 84*(1), 33-40.

Berghian-Grosan, C., Radu, T., Biris, A. R., Dan, M., Voica, C., Watanabe, F., . . . Vulcu, A. (2020). Platinum nanoparticles coated by graphene layers: A low-metal loading catalyst for methanol oxidation in alkaline media. *Journal of Energy Chemistry, 40*, 81-88.

Besra, L., & Liu, M. (2007). A review on fundamentals and applications of electrophoretic deposition (EPD). *Progress in Materials Science, 52*(1), 1-61.

Bessekhouad, Y., Robert, D., & Weber, J. (2003). Preparation of TiO_2 nanoparticles by sol-gel route. *International Journal of Photoenergy, 5*(3), 153-158.

Beydoun, D., Amal, R., Low, G., & McEvoy, S. (1999). Role of nanoparticles in photocatalysis. *Journal of Nanoparticle Research, 1*(4), 439-458.

Bhavani, K. S., Anusha, T., & Brahman, P. K. (2019). Fabrication and characterization of gold nanoparticles and fullerene-C60 nanocomposite film at glassy carbon electrode as potential electro-catalyst towards the methanol oxidation. *International Journal of Hydrogen Energy, 44*(47), 25863-25873.

Bi, Y., Hu, H., Ouyang, S., Jiao, Z., Lu, G., & Ye, J. (2012). Selective growth of Ag_3PO_4 submicro-cubes on Ag nanowires to fabricate necklace-like heterostructures for photocatalytic applications. *Journal of Materials Chemistry, 22*(30), 14847-14850.

Bolton, J. R., & Hall, D. O. (1991). The maximum efficiency of photosynthesis. *Photochemistry and Photobiology, 53*(4), 545-548.

Bordbar, M., Alimohammadi, T., Khoshnevisan, B., Khodadadi, B., & Yeganeh-Faal, A. (2015). Preparation of MWCNT/TiO_2–Co nanocomposite electrode by electrophoretic deposition and electrochemical study of hydrogen storage. *International Journal of Hydrogen Energy, 40*(31), 9613-9620.

Bott, A. W. (1998). Electrochemistry of semiconductors. *Current Separations, 17*, 87-92.

Boucher, M. B., Goergen, S., Yi, N., & Flytzani-Stephanopoulos, M. (2011). ‗Shape effects' in metal oxide supported nanoscale gold catalysts. *Physical Chemistry Chemical Physics, 13*(7), 2517-2527.

Brillson, L. (1982). The structure and properties of metal-semiconductor interfaces. *Surface Science Reports, 2*(2), 123-326.

Bullard, J. W., & Cima, M. J. (2006). Orientation dependence of the isoelectric point of TiO_2 (rutile) surfaces. *Langmuir, 22*(24), 10264-10271.

Burda, C., Chen, X., Narayanan, R., & El-Sayed, M. A. (2005). Chemistry and properties of nanocrystals of different shapes. *Chemical Reviews, 105*(4), 1025-1102.

Cabanas-Polo, S., Suslick, K. S., & Sanchez-Herencia, A. (2011). Effect of reaction conditions on size and morphology of ultrasonically prepared $Ni(OH)_2$ powders. *Ultrasonics Sonochemistry, 18*(4), 901-906.

Cai, C., Xu, Y.-F., Chen, H.-Y., Wang, X.-D., & Kuang, D.-B. (2018). Porous ZnO@ ZnSe nanosheet array for photoelectrochemical reduction of CO_2. *Electrochimica Acta, 274*, 298-305.

Cao, R., Yang, H., Zhang, S., & Xu, X. (2019). Engineering of Z-scheme 2D/3D architectures with $Ni(OH)_2$ on 3D porous g-C_3N_4 for efficiently photocatalytic H_2 evolution. *Applied Catalysis B: Environmental, 258*, 117997-118008.

Cao, S., Chen, C., Zhang, J., Zhang, C., Yu, W., Liang, B., & Tsang, Y. (2015). MnO_x quantum dots decorated reduced graphene oxide/TiO_2 nanohybrids for enhanced activity by a UV pre-catalytic microwave method. *Applied Catalysis B: Environmental, 176*, 500-512.

Cao, S., Wang, H., Yu, F., Shi, M., Chen, S., Weng, X., . . . Wu, Z. (2016). Catalyst performance and mechanism of catalytic combustion of dichloromethane (CH_2Cl_2) over Ce doped TiO_2. *Journal of Colloid and Interface Science, 463*, 233-241.

Chang, C.-J., Chao, P.-Y., & Lin, K.-S. (2019). Flower-like BiOBr decorated stainless steel wire-mesh as immobilized photocatalysts for photocatalytic degradation applications. *Applied Surface Science, 494*, 492-500.

Chang, J. S., Phuan, Y. W., Chong, M. N., & Ocon, J. D. (2020). Exploration of a novel Type II 1D-ZnO nanorods/$BiVO_4$ heterojunction photocatalyst for water depollution. *Journal of Industrial and Engineering Chemistry, 83*, 303-314.

Chang, Y.-H., Liu, C.-M., Chen, C., & Cheng, H.-E. (2012). The effect of geometric structure on photoluminescence characteristics of 1-D TiO_2 nanotubes and 2-D TiO_2 films fabricated by atomic layer deposition. *Journal of The Electrochemical Society, 159*(7), D401-D405.

Chen, C.-Y., Chen, S.-Y., & Liu, D.-M. (1999). Electrophoretic deposition forming of porous alumina membranes. *Acta Materialia, 47*(9), 2717-2726.

Chen, C., Lee, Y.-R., & Ahn, W.-S. (2016). CO_2 adsorption over metal-organic frameworks: A mini review. *Journal of Nanoscience and Nanotechnology, 16*(5), 4291-4301.

Chen, F., & Liu, M. (2001). Preparation of yttria-stabilized zirconia (YSZ) films on $La_{0.85}Sr_{0.15}MnO_3$ (LSM) and LSM–YSZ substrates using an electrophoretic deposition (EPD) process. *Journal of the European Ceramic Society, 21*(2), 127-134.

Cheng, H.-H., Chen, S.-S., Yang, S.-Y., Liu, H.-M., & Lin, K.-S. (2018). Sol-Gel hydrothermal synthesis and visible light photocatalytic degradation performance of Fe/N codoped TiO_2 catalysts. *Materials, 11*(6), 939-948.

Cheng, J., Yang, X., Xuan, X., Liu, N., & Zhou, J. (2020). Development of an efficient catalyst with controlled sulfur vacancies and high pyridine nitrogen content for the photoelectrochemical reduction of CO_2 into methanol. *Science of the Total Environment, 702*, 134981-134989.

Cheng, J., Zhang, M., Wu, G., Wang, X., Zhou, J., & Cen, K. (2014). Photoelectrocatalytic reduction of CO_2 into chemicals using Pt-modified reduced graphene oxide combined with Pt-modified TiO_2 nanotubes. *Environmental Science & Technology, 48*(12), 7076-7084.

Cheng, J., Zhang, M., Wu, G., Wang, X., Zhou, J., & Cen, K. (2015). Optimizing CO_2 reduction conditions to increase carbon atom conversion using a Pt-RGO/Pt-TNT photoelectrochemical cell. *Solar Energy Materials and Solar Cells, 132*, 606-614.

Chiorboli, C., Indelli, M., & Scandola, F. (2005). Photoinduced electron/energy transfer across molecular bridges in binuclear metal complexes *Molecular Wires and Electronics* (pp. 63-102). Berlin, Germany: Springer.

Cho, H., Kim, W. D., Lee, K., Lee, S., Kang, G.-S., Joh, H.-I., & Lee, D. C. (2018). Selectivity of photoelectrochemical CO_2 reduction modulated with electron transfer from size-tunable quantized energy states of CdSe nanocrystals. *Applied Surface Science, 429*, 2-8.

Choi, S. K., Kang, U., Lee, S., Ham, D. J., Ji, S. M., & Park, H. (2014). Sn-Coupled p-Si Nanowire Arrays for Solar Formate Production from CO_2. *Advanced Energy Materials, 4*(11), 1301614.

Chong, R., Fan, Y., Du, Y., Liu, L., Chang, Z., & Li, D. (2018). Hydroxyapatite decorated TiO_2 as efficient photocatalyst for selective reduction of CO_2 with H_2O into CH_4. *International Journal of Hydrogen Energy, 43*(49), 22329-22339.

Choudhury, B., & Choudhury, A. (2013). Oxygen vacancy and dopant concentration dependent magnetic properties of Mn doped TiO_2 nanoparticle. *Current Applied Physics, 13*(6), 1025-1031.

Chung, J., Park, S. H., Kim, E.-H., & Woo, S. I. (2015). Photoelectrochemical production of useful fuels from carbon dioxide on a polypyrrole-coated p-ZnTe photocathode under visible light irradiation. *Journal of Materials Chemistry A, 3*(3), 1089-1095.

Clavijo, S., Membrives, F., Quiroga, G., Boccaccini, A. R., & Santillán, M. J. (2016). Electrophoretic deposition of chitosan/Bioglass® and chitosan/Bioglass/TiO_2 composite coatings for bioimplants. *Ceramics International, 42*(12), 14206-14213.

Çögenli, M. S., & Yurtcan, A. B. (2020). Heteroatom doped 3D graphene aerogel supported catalysts for formic acid and methanol oxidation. *International Journal of Hydrogen Energy, 45*(1), 650-666.

Cokoja, M., Bruckmeier, C., Rieger, B., Herrmann, W. A., & Kühn, F. E. (2011). Transformation of Carbon Dioxide with Homogeneous Transition-Metal Catalysts: A Molecular Solution to a Global Challenge? *Angewandte Chemie International Edition, 50*(37), 8510-8537.

Colombo, D. P., & Bowman, R. M. (1996). Does interfacial charge transfer compete with charge carrier recombination? A femtosecond diffuse reflectance investigation of TiO_2 nanoparticles. *The Journal of Physical Chemistry, 100*(47), 18445-18449.

Cordoba, M., Miranda, C., Lederhos, C., Coloma-Pascual, F., Ardila, A., Fuentes, G., . . . Ramírez, A. (2017). Catalytic performance of Co_3O_4 on different activated carbon supports in the benzyl alcohol oxidation. *Catalysts, 7*(12), 384-395.

Corni, I., Ryan, M. P., & Boccaccini, A. R. (2008). Electrophoretic deposition: From traditional ceramics to nanotechnology. *Journal of the European Ceramic Society, 28*(7), 1353-1367.

Cozzoli, P., Comparelli, R., Fanizza, E., Curri, M., & Agostiano, A. (2003). Photocatalytic activity of organic-capped anatase TiO_2 nanocrystals in homogeneous organic solutions. *Materials Science and Engineering: C, 23*(6-8), 707-713.

D'Elia, A., Deering, J., Clifford, A., Lee, B., Grandfield, K., & Zhitomirsky, I. (2020). Electrophoretic deposition of polymethylmethacrylate and composites for biomedical applications. *Colloids and Surfaces B: Biointerfaces, 188*, Article#110763.

D‘Arienzo, M., Carbajo, J., Bahamonde, A., Crippa, M., Polizzi, S., Scotti, R., . . . Morazzoni, F. (2011). Photogenerated defects in shape-controlled TiO_2 anatase nanocrystals: a probe to evaluate the role of crystal facets in photocatalytic processes. *Journal of the American Chemical Society, 133*(44), 17652-17661.

Dai, L., Qin, Q., Wang, P., Zhao, X., Hu, C., Liu, P., . . . Xu, C. (2017). Ultrastable atomic copper nanosheets for selective electrochemical reduction of carbon dioxide. *Science Advances, 3*(9), e1701069-e1701078.

Daryakenari, A. A., Hosseini, D., Mirfasih, M. H., Apostoluk, A., Müller, C. R., & Delaunay, J.-J. (2017). Formation of NiO nanoparticle-attached nanographitic flake layers deposited by pulsed electrophoretic deposition for ethanol electro-oxidation. *Journal of Alloys and Compounds, 698*, 571-576.

Dashairya, L., Mehta, A., Saha, P., & Basu, S. (2020). Visible-light-induced enhanced photocatalytic degradation of Rhodamine-B dye using $Bi_xSb_{2-x}S_3$ solid-solution photocatalysts. *Journal of Colloid and Interface Science, 561*, 71-82.

Dau, H., & Zaharieva, I. (2009). Principles, efficiency, and blueprint character of solar-energy conversion in photosynthetic water oxidation. *Accounts of Chemical Research, 42*(12), 1861-1870.

de Brito, J. F., & Zanoni, M. V. B. (2017). On the application of Ti/TiO_2/CuO np junction semiconductor: A case study of electrolyte, temperature and potential influence on CO_2 reduction. *Chemical Engineering Journal, 318*, 264-271.

De la Cruz-Cruz, J., Domínguez-Crespo, M., Ramírez-Meneses, E., Torres-Huerta, A., Brachetti-Sibaja, S., Cayetano-Castro, N., & Dorantes-Rosales, H. (2020). Efficient stabilization of in situ fabrication of Pt_xPd_{1-x} nanostructures for electro-oxidation of methanol in alkaline medium. *International Journal of Hydrogen Energy, 45*, 4570-4586.

De Moura, A., Lima, R., Paris, E., Li, M., Varela, J. A., & Longo, E. (2011). Formation of β-nickel hydroxide plate-like structures under mild conditions and their optical properties. *Journal of Solid State Chemistry, 184*(10), 2818-2823.

Di Paola, A., Bellardita, M., & Palmisano, L. (2013). Brookite, the least known TiO_2 photocatalyst. *Catalysts, 3*(1), 36-73.

Diebold, U. (2003). The surface science of titanium dioxide. *Surface Science Reports, 48*(5-8), 53-229.

Dong, G., Wang, Y., Lei, H., Tian, G., Qi, S., & Wu, D. (2020). Hierarchical mesoporous titania nanoshell encapsulated on polyimide nanofiber as flexible, highly reactive, energy saving and recyclable photocatalyst for water purification. *Journal of Cleaner Production*, 120021-120031.

Dorraj, M., Goh, B. T., Sairi, N. A., Woi, P. M., & Basirun, W. J. (2018). Improved visible-light photocatalytic activity of TiO_2 co-doped with copper and iodine. *Applied Surface Science, 439*, 999-1009.

Dubal, D., Fulari, V., & Lokhande, C. (2012). Effect of morphology on supercapacitive properties of chemically grown β-$Ni(OH)_2$ thin films. *Microporous and Mesoporous Materials, 151*, 511-516.

Dzepina, B., Sigalas, I., Herrmann, M., & Nilen, R. (2013). The aqueous electrophoretic deposition (EPD) of diamond–diamond laminates. *International Journal of Refractory Metals and Hard Materials, 36*, 126-129.

Ehsan, M. A., Hakeem, A. S., Khaledi, H., Mazhar, M., Shahid, M. M., Pandikumar, A., & Huang, N. M. (2015). Fabrication of CuO–1.5 ZrO_2 composite thin film, from heteronuclear molecular complex and its electrocatalytic activity towards methanol oxidation. *Royal Society of Chemistry Advances, 5*(126), 103852-103862.

Ehsan, M. A., Naeem, R., McKee, V., Hakeem, A. S., & Mazhar, M. (2017). $MgTi_2O_5$ thin films from single molecular precursor for photoelectrochemical water splitting. *Solar Energy Materials and Solar Cells, 161*, 328-337.

Ehsan, M. A., Peiris, T. N., Wijayantha, K. U., Khaledi, H., Ming, H. N., Misran, M., . . . Mazhar, M. (2013). Surface morphological and photoelectrochemical studies of ZnS thin films developed from single source precursors by aerosol assisted chemical vapour deposition. *Thin Solid Films, 540*, 1-9.

Eisenberg, R., & Hendriksen, D. E. (1979). The binding and activation of carbon monoxide, carbon dioxide, and nitric oxide and their homogeneously catalyzed reactions. *Advances in Catalysis* (Vol. 28, pp. 79-172). New York: Elsevier.

Fadadu, K. B., & Soni, S. S. (2013). Spectral sensitization of TiO_2 by new hemicyanine dyes in dye solar cell yielding enhanced photovoltage: Probing chain length effect on performance. *Electrochimica Acta, 88*, 270-277.

Fan, C., Fan, Y., Zhen, C., Zheng, Q., & Sun, S. (2007). Studies of surface processes of electrocatalytic reduction of CO_2 on Pt (210), Pt (310) and Pt (510). *Science in China Series B: Chemistry, 50*(5), 593-598.

Feng, H., Xu, H., Feng, H., Gao, Y., & Jin, X. (2019). The sol-gel synthesis and photocatalytic activity of Gd-SiO_2-TiO_2 photocatalyst. *Chemical Physics Letters, 733*, 136676-136681.

Ferrari, B., & Moreno, R. (1997). Electrophoretic deposition of aqueous alumina slips. *Journal of the European Ceramic Society, 17*(4), 549-556.

Fischer, J., Lehmann, T., & Heitz, E. (1981). The production of oxalic acid from CO_2 and H_2O. *Journal of Applied Electrochemistry, 11*(6), 743-750.

Fisher, B. J., & Eisenberg, R. (1980). Electrocatalytic reduction of carbon dioxide by using macrocycles of nickel and cobalt. *Journal of the American Chemical Society, 102*(24), 7361-7363.

Friedlingstein, P., Andrew, R. M., Rogelj, J., Peters, G. P., Canadell, J. G., Knutti, R., . . . van Vuuren, D. P. (2014). Persistent growth of CO_2 emissions and implications for reaching climate targets. *Nature Geoscience, 7*(10), 709-715.

Fu, F., Shen, H., Xue, W., Zhen, Y., Soomro, R. A., Yang, X., . . . Chi, R. (2019). Alkali-assisted synthesis of direct Z-scheme based Bi_2O_3/Bi_2MoO_6 photocatalyst for highly efficient photocatalytic degradation of phenol and hydrogen evolution reaction. *Journal of Catalysis, 375*, 399-409.

Fujishima, A., & Honda, K. (1972). Electrochemical photolysis of water at a semiconductor electrode. *Nature, 238*(5358), 37-38.

Fujishima, A., Zhang, X., & Tryk, D. A. (2008). TiO_2 photocatalysis and related surface phenomena. *Surface Science Reports, 63*(12), 515-582.

Fujita, E., Creutz, C., Sutin, N., & Szalda, D. J. (1991). Carbon dioxide activation by cobalt (I) macrocycles: factors affecting carbon dioxide and carbon monoxide binding. *Journal of the American Chemical Society, 113*(1), 343-353.

Ganesh, V., Farzana, S., & Berchmans, S. (2011). Nickel hydroxide deposited indium tin oxide electrodes as electrocatalysts for direct oxidation of carbohydrates in alkaline medium. *Journal of Power Sources, 196*(23), 9890-9899.

Gangeri, M., Perathoner, S., Caudo, S., Centi, G., Amadou, J., Begin, D., . . . Su, D. S. (2009). Fe and Pt carbon nanotubes for the electrocatalytic conversion of carbon dioxide to oxygenates. *Catalysis Today, 143*(1-2), 57-63.

Gao, E., Wang, W., Shang, M., & Xu, J. (2011). Synthesis and enhanced photocatalytic performance of graphene-Bi_2WO_6 composite. *Physical Chemistry Chemical Physics, 13*(7), 2887-2893.

Gao, S., Jiao, X., Sun, Z., Zhang, W., Sun, Y., Wang, C., . . . Yang, S. (2016). Ultrathin Co_3O_4 layers realizing optimized CO_2 electroreduction to formate. *Angewandte Chemie International Edition, 55*(2), 698-702.

Gattrell, M., Gupta, N., & Co, A. (2006). A review of the aqueous electrochemical reduction of CO_2 to hydrocarbons at copper. *Journal of Electroanalytical Chemistry, 594*(1), 1-19.

Ge, M., Li, Q., Cao, C., Huang, J., Li, S., Zhang, S., . . . Lai, Y. (2017). One-dimensional TiO_2 nanotube photocatalysts for solar water splitting. *Advanced Science, 4*(1), 1600152-1600183.

Gennaro, A., Isse, A. A., Saveant, J.-M., Severin, M.-G., & Vianello, E. (1996). Homogeneous electron transfer catalysis of the electrochemical reduction of carbon dioxide. Do aromatic anion radicals react in an outer-sphere manner? *Journal of the American Chemical Society, 118*(30), 7190-7196.

Ghadimkhani, G., de Tacconi, N. R., Chanmanee, W., Janaky, C., & Rajeshwar, K. (2013). Efficient solar photoelectrosynthesis of methanol from carbon dioxide using hybrid CuO–Cu_2O semiconductor nanorod arrays. *Chemical Communications, 49*(13), 1297-1299.

Gholidoust, A., Atkinson, J. D., & Hashisho, Z. (2017). Enhancing CO_2 adsorption via amine-impregnated activated carbon from oil sands coke. *Energy & Fuels, 31*(2), 1756-1763.

Ghosh, M., & Raychaudhuri, A. (2011). Electric field induced reversible control of visible photoluminescence from ZnO nanoparticles. *Applied Physics Letters, 98*(15), 153109.

Gibson, D. H. (1999). Carbon dioxide coordination chemistry: metal complexes and surface-bound species. What relationships? *Coordination Chemistry Reviews, 185*, 335-355.

González, Z., Pérez-Mas, A. M., Blanco, C., Granda, M., & Santamaría, R. (2018). Influence of the electrophoretic deposition parameters on the formation of suspended graphene-based films. *Materials & Design, 160*, 58-64.

Gonzalez, Z., Yus, J., Caballero, A., Morales, J., Sanchez-Herencia, A., & Ferrari, B. (2017). Electrochemical performance of pseudo-capacitor electrodes fabricated by electrophoretic deposition inducing $Ni(OH)_2$ nanoplatelets agglomeration by layer-by-layer. *Electrochimica Acta, 247*, 333-343.

Göpel, W., & Schierbaum, K. D. (1995). SnO_2 sensors: current status and future prospects. *Sensors and Actuators B: Chemical, 26*(1), 1-12.

Grätzel, M. (2005). Solar energy conversion by dye-sensitized photovoltaic cells. *Inorganic Chemistry, 44*(20), 6841-6851.

Grills, D. C., & Fujita, E. (2010). New directions for the photocatalytic reduction of CO_2: Supramolecular, $scCO_2$ or biphasic ionic liquid−$scCO_2$ systems. *The Journal of Physical Chemistry Letters, 1*(18), 2709-2718.

Gu, J., Wuttig, A., Krizan, J. W., Hu, Y., Detweiler, Z. M., Cava, R. J., & Bocarsly, A. B. (2013). Mg-doped $CuFeO_2$ photocathodes for photoelectrochemical reduction of carbon dioxide. *The Journal of Physical Chemistry C, 117*(24), 12415-12422.

Guaraldo, T. T., De Brito, J. F., Wood, D., & Zanoni, M. V. B. (2015). A new Si/TiO_2/Pt pn junction semiconductor to demonstrate photoelectrochemical CO_2 conversion. *Electrochimica Acta, 185*, 117-124.

Gupta, S., & Tripathi, M. (2012). A review on the synthesis of TiO_2 nanoparticles by solution route. *Open Chemistry, 10*(2), 279-294.

Gust, D., Moore, T. A., & Moore, A. L. (2009). Solar fuels via artificial photosynthesis. *Accounts of Chemical Research, 42*(12), 1890-1898.

Habisreutinger, S. N., Schmidt-Mende, L., & Stolarczyk, J. K. (2013). Photocatalytic reduction of CO_2 on TiO_2 and other semiconductors. *Angewandte Chemie International Edition, 52*(29), 7372-7408.

Hadraba, H., Drdlik, D., Chlup, Z., Maca, K., Dlouhy, I., & Cihlar, J. (2012). Laminated alumina/zirconia ceramic composites prepared by electrophoretic deposition. *Journal of the European Ceramic Society, 32*(9), 2053-2056.

Hagfeldt, A., & Graetzel, M. (1995). Light-induced redox reactions in nanocrystalline systems. *Chemical Reviews, 95*(1), 49-68.

Haghbin, A., Liaghat, G., Arabi, A., Hadavinia, H., & Pol, M. (2018). Investigations on electrophoretic deposition of carbon nanotubes on glass textures to improve polymeric composites interface. *Composites Science and Technology, 155*, 197-204.

Hall, D. S., Lockwood, D. J., Bock, C., & MacDougall, B. R. (2015). Nickel hydroxides and related materials: a review of their structures, synthesis and properties. *Proceeding of the Royal Society A, 471*(2174), 20140792-20140856.

Hall, D. S., Lockwood, D. J., Poirier, S., Bock, C., & MacDougall, B. R. (2012). Raman and infrared spectroscopy of α and β-phases of thin nickel hydroxide films electrochemically formed on nickel. *The Journal of Physical Chemistry A, 116*(25), 6771-6784.

Halmann, M. (1978). Photoelectrochemical reduction of aqueous carbon dioxide on p-type gallium phosphide in liquid junction solar cells. *Nature, 275*(5676), 115-116.

Han, E., Hu, F., Zhang, S., Luan, B., Li, P., Sun, H., & Wang, S. (2018). Worm-like FeS_2/TiO_2 nanotubes for photoelectrocatalytic reduction of CO_2 to methanol under visible light. *Energy & Fuels, 32*(4), 4357-4363.

Hanaor, D. A., & Sorrell, C. C. (2011). Review of the anatase to rutile phase transformation. *Journal of Materials Science, 46*(4), 855-874.

Harichandran, G., Amalraj, S. D., & Shanmugam, P. (2014). Synthesis and characterization of phosphate anchored MnO_2 catalyzed solvent free synthesis of xanthene laser dyes. *Journal of Molecular Catalysis A: Chemical, 392*, 31-38.

Hawecker, J., Lehn, J.-M., & Ziessel, R. (1983). Efficient photochemical reduction of CO_2 to CO by visible light irradiation of systems containing $Re(bipy)(CO)_3X$ or $Ru(bipy)_3^{2+}$–Co^{2+} combinations as homogeneous catalysts. *Journal of the Chemical Society, Chemical Communications*, 9, 536-538.

He, H., Xiao, P., Zhou, M., Liu, F., Yu, S., Qiao, L., & Zhang, Y. (2013). PtNi alloy nanoparticles supported on carbon-doped TiO_2 nanotube arrays for photo-assisted methanol oxidation. *Electrochimica Acta, 88*, 782-789.

He, Q., Zhang, Q., Yang, X., Zhang, C., Zeng, X., Shi, J., . . . Xu, M. (2019). Enhanced electrocatalytic activity of palladium nanochains by modifying transition metal core-shell nanoparticles ($TM_{core\text{-}shell}$= Ni@NiO, Co@CoO) on reduced graphene oxide for methanol electro-oxidation. *Electrochimica Acta, 321*, 134688-134698.

Heavens, S. (1990). Electrophoretic deposition as a processing route for ceramics. *Noyes Publications, Advanced Ceramic Processing and Technology., 1*, 255-283.

Hedin, N., Chen, L., & Laaksonen, A. (2010). Sorbents for CO_2 capture from flue gas—aspects from materials and theoretical chemistry. *Nanoscale, 2*(10), 1819-1841.

Heise, S., Forster, C., Heer, S., Qi, H., Zhou, J., Virtanen, S., . . . Boccaccini, A. R. (2019). Electrophoretic deposition of gelatine nanoparticle/chitosan coatings. *Electrochimica Acta, 307*, 318-325.

Hinogami, R., Nakamura, Y., Yae, S., & Nakato, Y. (1998). An approach to ideal semiconductor electrodes for efficient photoelectrochemical reduction of carbon dioxide by modification with small metal particles. *The Journal of Physical Chemistry B, 102*(6), 974-980.

Hirota, K., Tryk, D., Hashimoto, K., Okawa, M., & Fujishima, A. (1998). Photoelectrochemical reduction of highly concentrated CO_2 in methanol solution *Studies in Surface Science and Catalysis,* 114, 589-592.

Hoffert, M. I., Caldeira, K., Benford, G., Criswell, D. R., Green, C., Herzog, H., . . . Lewis, J. S. (2002). Advanced technology paths to global climate stability: Energy for a greenhouse planet. *Science, 298*(5595), 981-987.

Hoffert, M. I., & Covey, C. (1992). Deriving global climate sensitivity from palaeoclimate reconstructions. *Nature, 360*(6404), 573.

Hoffmann, M. R., Martin, S. T., Choi, W., & Bahnemann, D. W. (1995). Environmental applications of semiconductor photocatalysis. *Chemical Reviews, 95*(1), 69-96.

Hoffmann, M. R., Moss, J. A., & Baum, M. M. (2011). Artificial photosynthesis: semiconductor photocatalytic fixation of CO_2 to afford higher organic compounds. *Dalton Transactions, 40*(19), 5151-5158.

Hong, S. J., Lee, S., Jang, J. S., & Lee, J. S. (2011). Heterojunction $BiVO_4/WO_3$ electrodes for enhanced photoactivity of water oxidation. *Energy & Environmental Science, 4*(5), 1781-1787.

Hori, Y., Takahashi, I., Koga, O., & Hoshi, N. (2003). Electrochemical reduction of carbon dioxide at various series of copper single crystal electrodes. *Journal of Molecular Catalysis A: Chemical, 199*(1-2), 39-47.

Hoshi, N., Sato, E., & Hori, Y. (2003). Electrochemical reduction of carbon dioxide on kinked stepped surfaces of platinum inside the stereographic triangle. *Journal of Electroanalytical Chemistry, 540*, 105-110.

Hosseinpour-Mashkani, S. M., Maddahfar, M., & Sobhani-Nasab, A. (2016). Precipitation synthesis, characterization, morphological control, and photocatalyst application of $ZnWO_4$ nanoparticles. *Journal of Electronic Materials, 45*(7), 3612-3620.

Hoyos, C. D., Agudelo, P. A., Webster, P. J., & Curry, J. A. (2006). Deconvolution of the factors contributing to the increase in global hurricane intensity. *Science, 312*(5770), 94-97.

Hu, B., Guild, C., & Suib, S. L. (2013). Thermal, electrochemical, and photochemical conversion of CO_2 to fuels and value-added products. *Journal of CO_2 Utilization, 1*, 18-27.

Hu, S., Wang, B., Ju, H., Jiang, L., Ma, Y., & Fan, Y. (2017). Photo-assisted electrocatalytic methanol oxidation based on an efficient 1D-TiO_2 nanorods arrays support electrode. *Journal of the Taiwan Institute of Chemical Engineers, 80*, 533-539.

Huang, X., Cao, T., Liu, M., & Zhao, G. (2013). Synergistic photoelectrochemical synthesis of formate from CO_2 on {121} hierarchical Co_3O_4. *The Journal of Physical Chemistry C, 117*(50), 26432-26440.

Huang, X., Shen, Q., Liu, J., Yang, N., & Zhao, G. (2016). A CO_2 adsorption-enhanced semiconductor/metal-complex hybrid photoelectrocatalytic interface for efficient formate production. *Energy & Environmental Science, 9*(10), 3161-3171.

Hussain, M., Akhter, P., Saracco, G., & Russo, N. (2015). Nanostructured TiO_2/KIT-6 catalysts for improved photocatalytic reduction of CO_2 to tunable energy products. *Applied Catalysis B: Environmental, 170*, 53-65.

Hwang, I., Baek, M., & Yong, K. (2015). Core/shell structured TiO_2/CdS electrode to enhance the light stability of perovskite solar cells. *ACS Applied Materials & Interfaces, 7*(50), 27863-27870.

Ichikawa, S., & Doi, R. (1996). Hydrogen production from water and conversion of carbon dioxide to useful chemicals by room temperature photoelectrocatalysis. *Catalysis Today, 27*(1-2), 271-277.

Ichimura, M., & Kato, Y. (2013). Fabrication of TiO_2/Cu_2O heterojunction solar cells by electrophoretic deposition and electrodeposition. *Materials Science in Semiconductor Processing, 16*(6), 1538-1541.

Iida, H., Takayanagi, K., Nakanishi, T., & Osaka, T. (2007). Synthesis of Fe_3O_4 nanoparticles with various sizes and magnetic properties by controlled hydrolysis. *Journal of Colloid and Interface Science, 314*(1), 274-280.

Irtem, E., Hernández-Alonso, M. D., Parra, A., Fàbrega, C., Penelas-Pérez, G., Morante, J. R., & Andreu, T. (2017). A photoelectrochemical flow cell design for the efficient CO_2 conversion to fuels. *Electrochimica Acta, 240*, 225-230.

Ishihara, T., Sato, K., & Takita, Y. (1996). Electrophoretic deposition of Y_2O_3-stabilized ZrO_2 electrolyte films in solid oxide fuel cells. *Journal of the American Ceramic Society, 79*(4), 913-919.

Ishii, K., Matsunaga, C., Kobayashi, K., Stevenson, A. J., Tardivat, C., & Uchikoshi, T. (2019). Fabrication of BSCF-based mixed ionic-electronic conducting membrane by electrophoretic deposition for oxygen separation application. *Journal of the European Ceramic Society, 39*(16), 5292-5297.

Ishimaki, K., Uchiyama, T., Okazaki, M., Lu, D., Uchimoto, Y., & Maeda, K. (2017). Influence of TiO_2 support on activity of Co_3O_4/TiO_2 photocatalysts for visible-light water oxidation. *Bulletin of the Chemical Society of Japan, 91*(3), 486-491.

Jadhav, A. P., Kim, C. W., Cha, H. G., Pawar, A. U., Jadhav, N. A., Pal, U., & Kang, Y. S. (2009). Effect of different surfactants on the size control and optical properties of Y_2O_3: Eu^{3+} nanoparticles prepared by coprecipitation method. *The Journal of Physical Chemistry C, 113*(31), 13600-13604.

Jaganyi, D., Altaf, M., & Wekesa, I. (2013). Synthesis and characterization of whisker-shaped MnO_2 nanostructure at room temperature. *Applied Nanoscience, 3*(4), 329-333.

Jang, J. W., Cho, S., Magesh, G., Jang, Y. J., Kim, J. Y., Kim, W. Y., . . . Lee, J. S. (2014). Aqueous-Solution Route to Zinc Telluride Films for Application to CO_2 Reduction. *Angewandte Chemie International Edition, 53*(23), 5852-5857.

Jeevanandam, P., Koltypin, Y., & Gedanken, A. (2001). Synthesis of nanosized α-nickel hydroxide by a sonochemical method. *Nano Letters, 1*(5), 263-266.

Ji, Y., & Luo, Y. (2016). Theoretical Study on the Mechanism of Photoreduction of CO_2 to CH_4 on the Anatase TiO_2 (101) Surface. *ACS Catalysis, 6*(3), 2018-2025.

Jiang, L., Zhou, G., Mi, J., & Wu, Z. (2012). Fabrication of visible-light-driven one-dimensional anatase TiO_2/Ag heterojunction plasmonic photocatalyst. *Catalysis Communications, 24*, 48-51.

Jiang, M., Wu, H., Li, Z., Ji, D., Li, W., Liu, Y., . . . Zhang, Z. (2018). Highly selective photoelectrochemical conversion of carbon dioxide to formic acid. *ACS Sustainable Chemistry & Engineering, 6*(1), 82-87.

Jiang, T., Wang, K., Guo, T., Wu, X., & Zhang, G. (2020). Fabrication of Z-scheme MoO_3/Bi_2O_4 heterojunction photocatalyst with enhanced photocatalytic performance under visible light irradiation. *Chinese Journal of Catalysis, 41*(1), 161-169.

Joghee, P., Malik, J. N., Pylypenko, S., & O'Hayre, R. (2015). A review on direct methanol fuel cells–In the perspective of energy and sustainability. *MRS Energy & Sustainability-A Review Journal,2,1-31*.

Ju, W., Bagger, A., Hao, G.-P., Varela, A. S., Sinev, I., Bon, V., . . . Strasser, P. (2017). Understanding activity and selectivity of metal-nitrogen-doped carbon catalysts for electrochemical reduction of CO_2. *Nature Communications, 8*(1), 1-9.

Juma, A. O., Arbab, E. A., Muiva, C. M., Lepodise, L. M., & Mola, G. T. (2017). Synthesis and characterization of CuO-NiO-ZnO mixed metal oxide nanocomposite. *Journal of Alloys and Compounds, 723*, 866-872.

Just, P.-E. (2013). Advances in the development of CO_2 capture solvents. *Energy Procedia, 37*, 314-324.

Kalantari, K., Ahmad, M. B., Shameli, K., & Khandanlou, R. (2013). Synthesis of talc/Fe_3O_4 magnetic nanocomposites using chemical co-precipitation method. *International Journal of Nanomedicine, 8*, 1817-1823.

Kannan, S., & Sundrarajan, M. (2015). Green synthesis of ruthenium oxide nanoparticles: Characterization and its antibacterial activity. *Advanced Powder Technology, 26*(6), 1505-1511.

Karbowniczek, J., Cordero-Arias, L., Virtanen, S., Misra, S. K., Valsami-Jones, E., Tuchscherr, L., . . . Czyrska-Filemonowicz, A. (2017). Electrophoretic deposition of organic/inorganic composite coatings containing ZnO nanoparticles exhibiting antibacterial properties. *Materials Science and Engineering: C, 77*, 780-789.

Karim, K. M. R., Ong, H. R., Abdullah, H., Yousuf, A., Cheng, C. K., & Khan, M. M. R. (2018). Photoelectrochemical reduction of carbon dioxide to methanol on p-type $CuFe_2O_4$ under visible light irradiation. *International Journal of Hydrogen Energy, 43*(39), 18185-18193.

Kecsenovity, E., Endrődi, B., Pápa, Z., Hernádi, K., Rajeshwar, K., & Janáky, C. (2016). Decoration of ultra-long carbon nanotubes with Cu_2O nanocrystals: a hybrid platform for enhanced photoelectrochemical CO_2 reduction. *Journal of Materials Chemistry A, 4*(8), 3139-3147.

Kerkez-Kuyumcu, Ö., Kibar, E., Dayıoğlu, K., Gedik, F., Akın, A. N., & Özkara-Aydınoğlu, Ş. (2015). A comparative study for removal of different dyes over M/TiO_2 (M= Cu, Ni, Co, Fe, Mn and Cr) photocatalysts under visible light irradiation. *Journal of Photochemistry and Photobiology A: Chemistry, 311*, 176-185.

Kern, R., Sastrawan, R., Ferber, J., Stangl, R., & Luther, J. (2002). Modeling and interpretation of electrical impedance spectra of dye solar cells operated under open-circuit conditions. *Electrochimica Acta, 47*(26), 4213-4225.

Keshmarzi, M. K., Daryakenari, A. A., Omidvar, H., Javanbakht, M., Ahmadi, Z., Delaunay, J.-J., & Badrnezhad, R. (2019). Pulsed electrophoretic deposition of nanographitic flake-nanostructured Co_3O_4 layers for efficient lithium-ion-battery anode. *Journal of Alloys and Compounds, 805*, 924-933.

Khajeh, R. T., Aber, S., & Nofouzi, K. (2020). Efficient improvement of microbial fuel cell performance by the modification of graphite cathode via electrophoretic deposition of CuO/ZnO. *Materials Chemistry and Physics, 240*, 122208-122211.

Ki, S. J., Park, Y.-K., Kim, J.-S., Lee, W.-J., Lee, H., & Jung, S.-C. (2019). Facile preparation of tungsten oxide doped TiO_2 photocatalysts using liquid phase plasma process for enhanced degradation of diethyl phthalate. *Chemical Engineering Journal, 377*, 120087-120094.

Kimura, E., Haruta, M., Koike, T., Shionoya, M., Takenouchi, K., & Iitaka, Y. (1993). A new cyclam with an NH_2-pendant donor, 6-amino-1,4,8,11-tetraazacyclotetradecane, and its nickel (II) complexes. *Inorganic Chemistry, 32*(12), 2779-2784.

Kimura, E., Wada, S., Shionoya, M., & Okazaki, Y. (1994). New series of multifunctionalized nickel (II)-cyclam (cyclam= 1, 4, 8, 11-tetraazacyclotetradecane) complexes. Application to the photoreduction of carbon dioxide. *Inorganic Chemistry, 33*(4), 770-778.

Klosek, S., & Raftery, D. (2001). Visible light driven V-doped TiO_2 photocatalyst and its photooxidation of ethanol. *The Journal of Physical Chemistry B, 105*(14), 2815-2819.

Kobayashi, K., Lou, S. N., Takatsuji, Y., Haruyama, T., Shimizu, Y., & Ohno, T. (2020). Photoelectrochemical reduction of CO_2 using a TiO_2 photoanode and a gas diffusion electrode modified with a metal phthalocyanine catalyst. *Electrochimica Acta*, 135805-135817.

Kočí, K., Obalová, L., Matějová, L., Plachá, D., Lacný, Z., Jirkovský, J., & Šolcová, O. (2009). Effect of TiO_2 particle size on the photocatalytic reduction of CO_2. *Applied Catalysis B: Environmental, 89*(3-4), 494-502.

Kolobov, N., Svintsitskiy, D., Kozlova, E., Selishchev, D., & Kozlov, D. (2017). UV-LED photocatalytic oxidation of carbon monoxide over TiO_2 supported with noble metal nanoparticles. *Chemical Engineering Journal, 314*, 600-611.

Korotcov, A. V., Huang, Y. S., Tiong, K. K., & Tsai, D. S. (2007). Raman scattering characterization of well-aligned RuO_2 and IrO_2 nanocrystals. *Journal of Raman Spectroscopy, 38*(6), 737-749.

Krueger, H., Knote, A., Schindler, U., Kern, H., & Boccaccini, A. (2004). Composite ceramic-metal coatings by means of combined electrophoretic deposition and galvanic methods. *Journal of Materials Science, 39*(3), 839-844.

Kudo, A., & Miseki, Y. (2009). Heterogeneous photocatalyst materials for water splitting. *Chemical Society Reviews, 38*(1), 253-278.

Kumar, B., Smieja, J. M., & Kubiak, C. P. (2010). Photoreduction of CO_2 on p-type silicon using Re(bipy-But)$(CO)_3$Cl: photovoltages exceeding 600 mV for the selective reduction of CO_2 to CO. *The Journal of Physical Chemistry C, 114*(33), 14220-14223.

Kumar, B., Smieja, J. M., Sasayama, A. F., & Kubiak, C. P. (2012). Tunable, light-assisted co-generation of CO and H_2 from CO_2 and H_2O by Re(bipy-*t*-bu)$(CO)_3$Cl and p-Si in non-aqueous medium. *Chemical Communications, 48*(2), 272-274.

Kuramochi, Y., Kamiya, M., & Ishida, H. (2014). Photocatalytic CO_2 reduction in N,N'-dimethylacetamide/water as an alternative solvent system. *Inorganic Chemistry, 53*(7), 3326-3332.

Kyaw, H. A., Yaacob, K., Noor, A. M., Matsuda, A., & Kawamura, G. (2019). Effect of deposition time CdSe-TiO_2 nanocomposite film by electrophoretic deposition for quantum dot sensitized solar cell. *Materials Today: Proceedings, 17*, 736-742.

Lakhera, S. K., Venkataramana, R., Mathew, G., Hafeez, H. Y., & Neppolian, B. (2020). Fabrication of high surface area AgI incorporated porous $BiVO_4$ heterojunction photocatalysts. *Materials Science in Semiconductor Processing, 106*, 104756-104766.

Lakshminarayana, G., & Buddhudu, S. (2006). Spectral analysis of Mn^{2+}, Co^{2+} and Ni^{2+}: B_2O_3–ZnO–PbO glasses. *Spectrochimica Acta Part A: Molecular and Biomolecular Spectroscopy, 63*(2), 295-304.

LaTempa, T. J., Rani, S., Bao, N., & Grimes, C. A. (2012). Generation of fuel from CO_2 saturated liquids using a p-Si nanowire‖n-TiO_2 nanotube array photoelectrochemical cell. *Nanoscale, 4*(7), 2245-2250.

Lee, K., Lee, S., Cho, H., Jeong, S., Kim, W. D., Lee, S., & Lee, D. C. (2018). Cu^+-incorporated TiO_2 overlayer on Cu_2O nanowire photocathodes for enhanced photoelectrochemical conversion of CO_2 to methanol. *Journal of Energy Chemistry, 27*(1), 264-270.

Lee, Y. H., Kim, H., Choi, H. S., Lee, D.-W., & Lee, K.-Y. (2015). Co-Mn-Ru/Al_2O_3 catalyst for the production of high-calorific synthetic natural gas. *Korean Journal of Chemical Engineering, 32*(11), 2220-2226.

Legrini, O., Oliveros, E., & Braun, A. (1993). Photochemical processes for water treatment. *Chemical Reviews, 93*(2), 671-698.

Li, C., & Liu, S. (2012). Preparation and characterization of $Ni(OH)_2$ and NiO mesoporous nanosheets. *Journal of Nanomaterials, 2012*, 1-6.

Li, H.-b., Zhang, J., Huang, G.-y., Fu, S.-h., Chao, M., Wang, B.-y., . . . Liao, H.-w. (2017). Hydrothermal synthesis and enhanced photocatalytic activity of hierarchical flower-like Fe-doped $BiVO_4$. *Transactions of Nonferrous Metals Society of China, 27*(4), 868-875.

Li, H., Bian, Z., Zhu, J., Huo, Y., Li, H., & Lu, Y. (2007). Mesoporous Au/TiO_2 nanocomposites with enhanced photocatalytic activity. *Journal of the American Chemical Society, 129*(15), 4538-4539.

Li, J., Shi, Q., Chen, Y., & Song, M. (2017). *Hydrothermal synthesis of Bi_2WO_6 and photocatalytic reduction of aqueous Cr (VI) under visible light irradiation.* Paper presented at the IOP Conference Series: Earth and Environmental Science, 22-25 December 2017, Singapore: IOP Publishing.

Li, K., Peng, T., Ying, Z., Song, S., & Zhang, J. (2016). Ag-loading on brookite TiO_2 quasi nanocubes with exposed {2 1 0} and {0 0 1} facets: Activity and selectivity of CO_2 photoreduction to CO/CH_4. *Applied Catalysis B: Environmental, 180*, 130-138.

Li, P., Gu, Y., Yu, Z., Gao, P., An, Y., & Li, J. (2019). TiO_2-SnO_2/SO_4^{2-} mesoporous solid superacid decorated nickel-based material as efficient electrocatalysts for methanol oxidation reaction. *Electrochimica Acta, 297*, 864-871.

Li, P., Zhang, J., Wang, H., Jing, H., Xu, J., Sui, X., . . . Yin, H. (2014). The photoelectric catalytic reduction of CO_2 to methanol on CdSeTe NSs/TiO_2 NTs. *Catalysis Science & Technology, 4*(4), 1070-1077.

Li, W., Song, Z., Deng, X., Fu, X.-Z., & Luo, J.-L. (2020). Decoration of NiO hollow spheres composed of stacked nanosheets with CeO_2 nanoparticles: Enhancement effect of CeO_2 for electrocatalytic methanol oxidation. *Electrochimica Acta*, 135684-135691.

Li, Y., Lu, G., & Li, S. (2003). Photocatalytic production of hydrogen in single component and mixture systems of electron donors and monitoring adsorption of donors by in situ infrared spectroscopy. *Chemosphere, 52*(5), 843-850.

Li, Y., Wang, H., Huang, L., Wang, C., Wang, Q., Zhang, F., . . . Li, H. (2020). Promoting LED light driven photocatalytic inactivation of bacteria by novel *β*-Bi_2O_3@ BiOBr core/shell photocatalyst. *Journal of Alloys and Compounds, 816*, 152665-152675.

Li, Y., Yang, X.-Y., Feng, Y., Yuan, Z.-Y., & Su, B.-L. (2012). One-dimensional metal oxide nanotubes, nanowires, nanoribbons, and nanorods: synthesis, characterizations, properties and applications. *Critical Reviews in Solid State and Materials Sciences, 37*(1), 1-74.

Liang, J., Chai, Y., Li, L., Li, D., Shen, J., Zhang, Y., & Wang, X. (2020). Germanium and iron double-substituted $ZnGa_2O_4$ solid-solution photocatalysts with modulated band structure for boosting photocatalytic CO_2 reduction with H_2O. *Applied Catalysis B: Environmental, 265*, 118551-118559.

Lim, S. P., Pandikumar, A., Huang, N. M., & Lim, H. N. (2014). Silver/titania nanocomposite-modified photoelectrodes for photoelectrocatalytic methanol oxidation. *International Journal of Hydrogen Energy, 39*(27), 14720-14729.

Linsebigler, A. L., Lu, G., & Yates Jr, J. T. (1995). Photocatalysis on TiO_2 surfaces: principles, mechanisms, and selected results. *Chemical Reviews, 95*(3), 735-758.

Liu, H., Cheng, S., Wu, M., Wu, H., Zhang, J., Li, W., & Cao, C. (2000). Photoelectrocatalytic degradation of sulfosalicylic acid and its electrochemical impedance spectroscopy investigation. *The Journal of Physical Chemistry A, 104*(30), 7016-7020.

Liu, X.-y., Guo, R.-t., Qin, H., Wang, Z.-y., Shi, X., Pan, W.-g., . . . Gu, J.-w. (2019). Fabrication of $Bi_2O_2(OH)NO_3/g\text{-}C_3N_4$ nanocomposites for efficient CO_2 photocatalytic reduction. *Colloids and Surfaces A: Physicochemical and Engineering Aspects, 580*, 123782-123791.

Liu, Z., Ma, R., Osada, M., Takada, K., & Sasaki, T. (2005). Selective and controlled synthesis of α-and β-cobalt hydroxides in highly developed hexagonal platelets. *Journal of the American Chemical Society, 127*(40), 13869-13874.

Lockwood, D., Cottam, M., & Baskey, J. (1992). One-and two-magnon excitations in NiO. *Journal of Magnetism and Magnetic Materials, 104*, 1053-1054.

Lokhande, P., Pawar, K., & Chavan, U. (2018). Chemically deposited ultrathin α-$Ni(OH)_2$ nanosheet using surfactant on Ni foam for high performance supercapacitor application. *Materials Science for Energy Technologies, 1*(2), 166-170.

Long, X., Yin, P., Lei, T., Wang, K., & Zhan, Z. (2020). Methanol electro-oxidation on Cu@Pt/C core-shell catalyst derived from Cu-MOF. *Applied Catalysis B: Environmental, 260-265*, 118187-118192.

Luna, A. L., Matter, F., Schreck, M., Wohlwend, J., Tervoort, E., Colbeau-Justin, C., & Niederberger, M. (2020). Monolithic metal-containing TiO_2 aerogels assembled from crystalline pre-formed nanoparticles as efficient photocatalysts for H_2 generation. *Applied Catalysis B: Environmental*, 118660-118670.

Luttrell, T., Halpegamage, S., Tao, J., Kramer, A., Sutter, E., & Batzill, M. (2014). Why is anatase a better photocatalyst than rutile? Model studies on epitaxial TiO_2 films. *Scientific reports, 4*(1), 1-8.

Lv, H., & Mu, S. (2014). Nano-ceramic support materials for low temperature fuel cell catalysts. *Nanoscale, 6*(10), 5063-5074.

Ma, J., Wang, L., Wu, Y., Dong, X., Ma, Q., Qiao, C., . . . Zhang, J. (2014). Facile synthesis of Fe_3O_4 nanoparticles with a high specific surface area. *Materials Transactions, 55*(12), 1900-1902.

Ma, X., Chen, P., Li, D., Zhang, Y., & Yang, D. (2007). Electrophotoluminescence of ZnO film. *Applied Physics Letters, 91*(2), Article#021105.

Ma, Y., Han, J., Wang, M., Chen, X., & Jia, S. (2018). Electrophoretic deposition of graphene-based materials: A review of materials and their applications. *Journal of Materiomics, 4*(2), 108-120.

Magesh, G., Kim, E. S., Kang, H. J., Banu, M., Kim, J. Y., Kim, J. H., & Lee, J. S. (2014). A versatile photoanode-driven photoelectrochemical system for conversion of CO_2 to fuels with high faradaic efficiencies at low bias potentials. *Journal of Materials Chemistry A, 2*(7), 2044-2049.

Mao, J., Li, K., & Peng, T. (2013). Recent advances in the photocatalytic CO_2 reduction over semiconductors. *Catalysis Science & Technology, 3*(10), 2481-2498.

Marandi, M., Pirhadi, M., & Davarnejad, R. (2015). Facile modified cyclic electrophoretic deposition of hydrothermally prepared TiO_2 nanocrystals and their application in dye sensitized solar cells. *Journal of Alloys and Compounds, 646*, 264-270.

Mat, A. N. C., Sairi, N. A., Basirun, W. J., Rezayi, M., Teridi, M. A. M., & Mazhar, M. (2019). Photoelectrocatalytic oxidation of methanol over RuO_2-MnO_2-Co_3O_4 supported porous anatase under visible light irradiation. *Materials Chemistry and Physics, 224*, 196-205.

Mathew, S., kumar Prasad, A., Benoy, T., Rakesh, P., Hari, M., Libish, T., . . . Vallabhan, C. (2012). UV-visible photoluminescence of TiO_2 nanoparticles prepared by hydrothermal method. *Journal of Fluorescence, 22*(6), 1563-1569.

Mathews, T., Manoravi, P., Antony, M., Sellar, J., & Muddle, B. (2000). Fabrication of $La_{1-x}Sr_xGa_{1-y}Mg_yO_{3-(x+y)/2}$ thin films by pulsed laser ablation. *Solid State Ionics, 135*(1-4), 397-402.

Matsuoka, S., Yamamoto, K., Ogata, T., Kusaba, M., Nakashima, N., Fujita, E., & Yanagida, S. (1993). Efficient and selective electron mediation of cobalt complexes with cyclam and related macrocycles in the p-terphenyl-catalyzed photoreduction of carbon dioxide. *Journal of the American Chemical Society, 115*(2), 601-609.

Meher, S. K., & Rao, G. R. (2013). Morphology-controlled promoting activity of nanostructured MnO_2 for methanol and ethanol electrooxidation on Pt/C. *The Journal of Physical Chemistry C, 117*(10), 4888-4900.

Mei, Z., Li, Y., Fan, M., Argyle, M. D., & Tang, J. (2014). The effects of bimetallic Co–Ru nanoparticles on $Co/RuO_2/Al_2O_3$ catalysts for the water gas shift and methanation. *International Journal of Hydrogen Energy, 39*(27), 14808-14816.

Meng, A., Wu, S., Cheng, B., Yu, J., & Xu, J. (2018). Hierarchical $TiO_2/Ni(OH)_2$ composite fibers with enhanced photocatalytic CO_2 reduction performance. *Journal of Materials Chemistry A, 6*(11), 4729-4736.

Michaud, X., Shi, K., & Zhitomirsky, I. (2019). Electrophoretic deposition of $LiFePO_4$ for Li-ion batteries. *Materials Letters, 241*, 10-13.

Mills, A., Duckmanton, P. A., & Reglinski, J. (2010). A simple, novel method for preparing an effective water oxidation catalyst. *Chemical Communications, 46*(14), 2397-2398.

Mills, A., Wang, J., & Crow, M. (2006). Photocatalytic oxidation of soot by P25 TiO_2 films. *Chemosphere, 64*(6), 1032-1035.

Mitoraj, D., Jańczyk, A., Strus, M., Kisch, H., Stochel, G., Heczko, P. B., & Macyk, W. (2007). Visible light inactivation of bacteria and fungi by modified titanium dioxide. *Photochemical & Photobiological Sciences, 6*(6), 642-648.

Mohammadi, E., Aliofkhazraei, M., & Rouhaghdam, A. S. (2018). In-situ study of electrophoretic deposition of zinc oxide nanosheets and nanorods. *Ceramics International, 44*(2), 1471-1482.

Möller, T., Ju, W., Bagger, A., Wang, X., Luo, F., Thanh, T. N., . . . Strasser, P. (2019). Efficient CO_2 to CO electrolysis on solid Ni–N–C catalysts at industrial current densities. *Energy & Environmental Science, 12*(2), 640-647.

Momeni, M. M., & Nazari, Z. (2016). Preparation of TiO_2 and $WO_3–TiO_2$ nanotubes decorated with PbO nanoparticles by chemical bath deposition process: a stable and efficient photo catalyst. *Ceramics International, 42*(7), 8691-8697.

Mondelli, C., Amrute, A. P., Krumeich, F., Schmidt, T., & Pérez-Ramírez, J. (2011). Shaped $RuO_2/SnO_2–Al_2O_3$ Catalyst for Large-Scale Stable Cl_2 Production by HCl Oxidation. *ChemCatChem, 3*(4), 657-660.

Morelli, S., Pérez, R., Querejeta, A., Munoz, J., Lusvarghi, L., Gualtieri, M. L., . . . Grande, H.-J. (2018). Photocatalytic enamel/TiO_2 coatings developed by electrophoretic deposition for methyl orange decomposition. *Ceramics International, 44*(14), 16199-16208.

Moreno, R., & Ferrari, B. (2000). Effect of the slurry properties on the homogeneity of alumina deposits obtained by aqueous electrophoretic deposition. *Materials Research Bulletin, 35*(6), 887-897.

Morris, A. J., Meyer, G. J., & Fujita, E. (2009). Molecular approaches to the photocatalytic reduction of carbon dioxide for solar fuels. *Accounts of chemical research, 42*(12), 1983-1994.

Morris Hotsenpiller, P., Bolt, J., Farneth, W., Lowekamp, J., & Rohrer, G. (1998). Orientation dependence of photochemical reactions on TiO_2 surfaces. *The Journal of Physical Chemistry B, 102*(17), 3216-3226.

Mumtaz, A., Mohamed, N. M., Mazhar, M., Ehsan, M. A., & Mohamed Saheed, M. S. (2016). Core–shell vanadium modified titania@ β-In2S3 hybrid nanorod arrays for superior interface stability and photochemical activity. *ACS Applied Materials & Interfaces, 8*(14), 9037-9049.

Murli, C., Sharma, S. M., Kulshreshtha, S., & Sikka, S. (2001). High-pressure behavior of β-$Ni(OH)_2$—a Raman scattering study. *Physica B: Condensed Matter, 307*(1-4), 111-116.

Mylarappa, M., Lakshmi, V. V., Mahesh, K. V., Nagaswarupa, H., & Raghavendra, N. (2016). *A facile hydrothermal recovery of nano sealed MnO_2 particle from waste batteries: An advanced material for electrochemical and environmental applications.* Paper presented at the IOP Conference Series: Materials Science and Engineering,14-16 July 2016, Bangalore, India.

Naeem, R., Ehsan, M. A., Rehman, A., Yamani, Z. H., Hakeem, A. S., & Mazhar, M. (2018). Single step aerosol assisted chemical vapor deposition of p–n Sn (II) oxide–Ti (IV) oxide nanocomposite thin film electrodes for investigation of photoelectrochemical properties. *New Journal of Chemistry, 42*(7), 5256-5266.

Nakajima, H., Mori, T., & Watanabe, M. (2004). Influence of platinum loading on photoluminescence of TiO_2 powder. *Journal of Applied Physics, 96*(1), 925-927.

Namin, H. E., Hashemipour, H., & Ranjbar, M. (2008). Effect of aging and calcination on morphology and properties of synthesized nanocrystalline TiO_2. *International Journal of Modern Physics B, 22*(18n19), 3210-3215.

Nealson, K. H., & Conrad, P. G. (1999). Life: past, present and future. *Philosophical Transactions of the Royal Society of London B: Biological Sciences, 354*(1392), 1923-1939.

Nea u, S. t., Maciá-Agull , J. A., Concepci n, P., & Garcia, H. (2014). Gold–copper nanoalloys supported on TiO_2 as photocatalysts for CO_2 reduction by water. *Journal of the American Chemical Society, 136*(45), 15969-15976.

Nguyen, B. H., Nguyen, V. H., & Vu, D. L. (2015). Photocatalytic composites based on titania nanoparticles and carbon nanomaterials. *Advances in Natural Sciences: Nanoscience and Nanotechnology, 6*(3), 033001-033015.

Ni, M., Leung, M. K., Leung, D. Y., & Sumathy, K. (2007). A review and recent developments in photocatalytic water-splitting using TiO_2 for hydrogen production. *Renewable and Sustainable Energy Reviews, 11*(3), 401-425.

Noor, T., Zaman, N., Nasir, H., Iqbal, N., & Hussain, Z. (2019). Electro catalytic study of NiO-MOF/rGO composites for methanol oxidation reaction. *Electrochimica Acta, 307*, 1-12.

Norouzi, O., Kheradmand, A., Jiang, Y., Di Maria, F., & Masek, O. (2019). Superior activity of metal oxide biochar composite in hydrogen evolution under artificial solar irradiation: A promising alternative to conventional metal-based photocatalysts. *International Journal of Hydrogen Energy, 44*(54), 28698-28708.

Obregón, S., Hernández-Uresti, D., Vázquez, A., & Sánchez-Martínez, D. (2018). Electrophoretic deposition of $PbMoO_4$ nanoparticles for photocatalytic degradation of tetracycline. *Applied Surface Science, 457*, 501-507.

Ogura, K., Migita, C., & Wadaka, K. (1991). Homogeneous catalysis in the mediated electrochemical reduction of carbon dioxide. *Journal of Molecular Catalysis, 67*(2), 161-173.

Onkani, S. P., Diagboya, P. N., Mtunzi, F. M., Klink, M. J., Olu-Owolabi, B. I., & Pakade, V. (2020). Comparative study of the photocatalytic degradation of 2–chlorophenol under UV irradiation using pristine and Ag-doped species of TiO_2, ZnO and ZnS photocatalysts. *Journal of Environmental Management, 260*, 110145-110154.

Orr, J. C., Fabry, V. J., Aumont, O., Bopp, L., Doney, S. C., Feely, R. A., . . . Joos, F. (2005). Anthropogenic ocean acidification over the twenty-first century and its impact on calcifying organisms. *Nature, 437*(7059), 681-686.

Özdokur, K. V., Çırak, B. B., Caglar, B., Çırak, Ç., Karadeniz, S. M., Kılınç, T., . . . Ekinci, A. E. (2018). Fabrication of TiO_2/ZnO/Pt nanocomposite electrode with enhanced electrocatalytic activity for methanol oxidation. *Vacuum, 155*, 242-248.

Pal, N., Banerjee, S., & Bhaumik, A. (2018). A facile route for the syntheses of $Ni(OH)_2$ and NiO nanostructures as potential candidates for non-enzymatic glucose sensor. *Journal of Colloid and Interface Science, 516*, 121-127.

Palanisamy, S., & Srinivasan, S. (2019). Electrochemical reduction of CO_2 on $Ni(OH)_2$ doped water dispersible graphene under different electrolyte conditions. *SN Applied Sciences, 1*(8), 837-843.

Pan, D., Ye, X., Cao, Y., Zhu, S., Chen, X., Chen, M., . . . Li, G. (2020). Photoanode driven photoelectrocatalytic system for CO_2 reduction to formic acid by using CoO_x cathode. *Applied Surface Science, 511*, 145497-145505.

Pan, F., Deng, W., Justiniano, C., & Li, Y. (2018). Identification of champion transition metals centers in metal and nitrogen-codoped carbon catalysts for CO_2 reduction. *Applied Catalysis B: Environmental, 226*, 463-472.

Pan, Z., & Bukur, D. B. (2011). Fischer–Tropsch synthesis on Co/ZnO catalyst—Effect of pretreatment procedure. *Applied Catalysis A: General, 404*(1), 74-80.

Panayotov, D. A., Burrows, S. P., & Morris, J. R. (2012). Photooxidation mechanism of methanol on rutile TiO_2 nanoparticles. *The Journal of Physical Chemistry C, 116*(11), 6623-6635.

Paracchino, A., Laporte, V., Sivula, K., Grätzel, M., & Thimsen, E. (2011). Highly active oxide photocathode for photoelectrochemical water reduction. *Nature Materials, 10*(6), 456-461.

Park, K.-W., Han, S.-B., & Lee, J.-M. (2007). Photo (UV)-enhanced performance of Pt–TiO_2 nanostructure electrode for methanol oxidation. *Electrochemistry Communications, 9*(7), 1578-1581.

Patil, P., Kadam, L., & Lokhande, C. (1996). Preparation and characterization of spray pyrolysed cobalt oxide thin films. *Thin Solid Films, 272*(1), 29-32.

Pattanayak, P., Pramanik, N., Kumar, P., & Kundu, P. P. (2018). Fabrication of cost-effective non-noble metal supported on conducting polymer composite such as copper/polypyrrole graphene oxide (Cu_2O/PPy–GO) as an anode catalyst for methanol oxidation in DMFC. *International Journal of Hydrogen Energy, 43*(25), 11505-11519.

Patzke, G. R., Zhou, Y., Kontic, R., & Conrad, F. (2011). Oxide nanomaterials: synthetic developments, mechanistic studies, and technological innovations. *Angewandte Chemie International Edition, 50*(4), 826-859.

Paul, A., & Dhar, S. S. (2020). Construction of hierarchical $MnMoO_4/NiFe_2O_4$ nanocomposite: Highly efficient visible light driven photocatalyst in the degradation of different polluting dyes in aqueous medium. *Colloids and Surfaces A: Physicochemical and Engineering Aspects, 585*, 124090-124100.

Peiris, D., Ekanayake, P., & Petra, M. I. (2018). Stacked rGO–TiO_2 photoanode via electrophoretic deposition for highly efficient dye-sensitized solar cells. *Organic Electronics, 59*, 399-405.

Peng, H., Lu, J., Wu, C., Yang, Z., Chen, H., Song, W., . . . Yin, H. (2015). Co-doped MoS_2 NPs with matched energy band and low overpotential high efficiently convert CO_2 to methanol. *Applied Surface Science, 353*, 1003-1012.

Peng, X., Chen, Y., Mi, Y., Zhuo, L., Qi, G., Ren, J., . . . Luo, J. (2019). Efficient Electroreduction CO_2 to CO over MnO_2 Nanosheets. *Inorganic Chemistry*.

Peng, Y.-P., Yeh, Y.-T., Shah, S. I., & Huang, C. (2012). Concurrent photoelectrochemical reduction of CO_2 and oxidation of methyl orange using nitrogen-doped TiO_2. *Applied Catalysis B: Environmental, 123*, 414-423.

Peng, Z., & Liu, M. (2001). Preparation of Dense Platinum-Yttria Stabilized Zirconia and Yttria Stabilized Zirconia Films on Porous $La_{0.9}Sr_{0.1}MnO_3$ (LSM) Substrates. *Journal of the American Ceramic Society, 84*(2), 283-288.

Perini, J. A. L., Cardoso, J. C., de Brito, J. F., & Zanoni, M. V. B. (2018). Contribution of thin films of ZrO_2 on TiO_2 nanotubes electrodes applied in the photoelectrocatalytic CO_2 conversion. *Journal of CO_2 Utilization, 25*, 254-263.

Phienluphon, R., Shi, L., Sun, J., Niu, W., Lu, P., Zhu, P., . . . Tsubaki, N. (2014). Ruthenium promoted cobalt catalysts prepared by an autocombustion method directly used for Fischer–Tropsch synthesis without further reduction. *Catalysis Science & Technology, 4*(9), 3099-3107.

Phoon, B. L., Lai, C. W., Pan, G.-T., Yang, T. C.-K., & Juan, J. C. (2018). One-pot hydrothermal synthesis of strontium titanate nanoparticles photoelectrode using electrophoretic deposition for enhancing photoelectrochemical water splitting. *Ceramics International, 44*(8), 9923-9933.

Pirkanniemi, K., & Sillanpää, M. (2002). Heterogeneous water phase catalysis as an environmental application: a review. *Chemosphere, 48*(10), 1047-1060.

Polo, A. S., Santos, M., De Souza, R. F., & Alves, W. A. (2011). Pt–Ru–TiO_2 photoelectrocatalysts for methanol oxidation. *Journal of Power Sources, 196*(2), 872-876.

Popić, J., Avramov-Ivić, M., & Vuković, N. (1997). Reduction of carbon dioxide on ruthenium oxide and modified ruthenium oxide electrodes in 0.5 M $NaHCO_3$. *Journal of Electroanalytical Chemistry, 421*(1-2), 105-110.

Powers, R. (1975). The Electrophoretic Forming of Beta-Alumina Ceramic. *Journal of The Electrochemical Society, 122*(4), 490-500.

Pradhan, S., Ghosh, D., & Chen, S. (2009). Janus nanostructures based on Au−TiO_2 heterodimers and their photocatalytic activity in the oxidation of methanol. *ACS Applied Materials & Interfaces, 1*(9), 2060-2065.

Qi, Y., Qi, H., Lu, C., Yang, Y., & Zhao, Y. (2009a). Photoluminescence and magnetic properties of β-Ni $(OH)_2$ nanoplates and NiO nanostructures. *Journal of Materials Science: Materials in Electronics, 20*(5), 479-483.

Qi, Y., Qi, H., Lu, C., Yang, Y., & Zhao, Y. (2009b). Photoluminescence and magnetic properties of β-$Ni(OH)_2$ nanoplates and NiO nanostructures. *Journal of Materials Science: Materials in Electronics, 20*(5), 479-483.

Qian, L., Luo, S., Wu, L., Hu, X., Chen, W., & Wang, X. (2020). In situ growth of metal organic frameworks derived hierarchical hollow porous $Co_3O_4/NiCo_2O_4$ nanocomposites on nickel foam as self-supported flexible electrode for methanol electrocatalytic oxidation. *Applied Surface Science, 503*, 144306-144315.

Qiao, J., Liu, Y., Hong, F., & Zhang, J. (2014). A review of catalysts for the electroreduction of carbon dioxide to produce low-carbon fuels. *Chemical Society Reviews, 43*(2), 631-675.

Qingliang, S., Hejun, L., Fengling, Z., Qiang, S., & Qiangang, F. (2018). Electrophoretic deposition of carbon nanotubes for improved ablation resistance of carbon/carbon composites. *Corrosion Science, 132*, 204-213.

Qiu, J., Zeng, G., Ha, M.-A., Ge, M., Lin, Y., Hettick, M., . . . Cronin, S. B. (2015). Artificial photosynthesis on TiO_2-passivated InP nanopillars. *Nano Letters, 15*(9), 6177-6181.

Qu, J., Zhang, X., Wang, Y., & Xie, C. (2005). Electrochemical reduction of CO_2 on RuO_2/TiO_2 nanotubes composite modified Pt electrode. *Electrochimica Acta, 50*(16), 3576-3580.

Qu, Z., Liu, Z., Wu, A., Piao, C., Li, S., Wang, J., & Song, Y. (2020). Preparation of a coated Z-scheme and H-type $SrTiO_3$/($BiFeO_3$@ ZnS) composite photocatalyst and application in degradation of 2,4-dichlorophenol with simultaneous conversion of Cr (VI). *Separation and Purification Technology, 240*, 116653-116667.

Rahmstorf, S., Cazenave, A., Church, J. A., Hansen, J. E., Keeling, R. F., Parker, D. E., & Somerville, R. C. (2007). Recent climate observations compared to projections. *Science, 316*(5825), 709-709.

Rajakumar, G., Rahuman, A. A., Roopan, S. M., Khanna, V. G., Elango, G., Kamaraj, C., . . . Velayutham, K. (2012). Fungus-mediated biosynthesis and characterization of TiO_2 nanoparticles and their activity against pathogenic bacteria. *Spectrochimica Acta Part A: Molecular and Biomolecular Spectroscopy, 91*, 23-29.

Ramesh, T., & Kamath, P. V. (2006). Synthesis of nickel hydroxide: effect of precipitation conditions on phase selectivity and structural disorder. *Journal of Power Sources, 156*(2), 655-661.

Rau, S., Walther, D., & Vos, J. G. (2007). Inspired by nature: light driven organometallic catalysis by heterooligonuclear Ru (II) complexes. *Dalton Transactions*(9), 915-919.

Rebello, J. S., Samant, P. V., Figueiredo, J. L., & Fernandes, J. B. (2006). Enhanced electrocatalytic activity of carbon-supported MnO_x/Ru catalysts for methanol oxidation in fuel cells. *Journal of Power Sources, 153*(1), 36-40.

Regmi, C., Maya-Flores, E., Lee, S., & Rodríguez-González, V. (2018). Cerium-doped β-$Ni(OH)_2$ hexagon nanosheets: an effective photocatalyst for the degradation of the emerging water pollutant, naproxen. *Nanotechnology, 29*(37), Article#375603.

Rehman, M. A. U., Munawar, M. A., Schubert, D. W., & Boccaccini, A. R. (2019). Electrophoretic deposition of chitosan/gelatin/bioactive glass composite coatings on 316L stainless steel: A design of experiment study. *Surface and Coatings Technology, 358*, 976-986.

Reuter, K., & Scheffler, M. (2006). First-principles kinetic Monte Carlo simulations for heterogeneous catalysis: Application to the CO oxidation at RuO_2 (110). *Physical Review B, 73*(4), 045433-045451.

Roche, I., & Scott, K. (2009). Carbon-supported manganese oxide nanoparticles as electrocatalysts for oxygen reduction reaction (orr) in neutral solution. *Journal of Applied Electrochemistry, 39*(2), 197-204.

Roy, A., Jadhav, H. S., Cho, M., & Seo, J. G. (2019). Electrochemical deposition of self-supported bifunctional copper oxide electrocatalyst for methanol oxidation and oxygen evolution reaction. *Journal of industrial and Engineering chemistry, 76*, 515-523.

Russell, W. W., & Miller, G. H. (1950). Catalytic hydrogenation of carbon dioxide to higher hydrocarbons. *Journal of the American Chemical Society, 72*(6), 2446-2454.

Sadegh, H., Shahryari-ghoshekandi, R., & Kazemi, M. (2014). Study in synthesis and characterization of carbon nanotubes decorated by magnetic iron oxide nanoparticles. *International Nano Letters, 4*(4), 129-135.

Sahara, G., Abe, R., Higashi, M., Morikawa, T., Maeda, K., Ueda, Y., & Ishitani, O. (2015). Photoelectrochemical CO_2 reduction using a Ru(II)–Re(I) multinuclear metal complex on a p-type semiconducting NiO electrode. *Chemical Communications, 51*(53), 10722-10725.

Sahu, D. R., Hong, L., Wang, S.-C., & Huang, J.-L. (2009). Synthesis, analysis and characterization of ordered mesoporous TiO_2/SBA-15 matrix: Effect of calcination temperature. *Microporous and Mesoporous Materials, 117*(3), 640-649.

Sajgure, M., Kachare, B., Gawhale, P., Waghmare, S., & Jagadale, G. (2016). Direct methanol fuel cell: A review. *International Journal of Current Engineering and Technology*(6), 8-11.

Sakata, T., Hashimoto, K., & Kawai, T. (1984). Catalytic properties of ruthenium oxide on n-type semiconductors under illumination. *The Journal of Physical Chemistry, 88*(22), 5214-5221.

Salehzadeh, D., Marashi, P., & Sadeghian, Z. (2019). Electrophoretic deposited $Ni(OH)_2$-YSZ and NiO-YSZ nanocomposite coatings, microstructural and electrochemical evaluation. *Surface and Coatings Technology*, 125155-125164.

Samsudin, M. F. R., Jayabalan, P. J., Ong, W.-J., Ng, Y. H., & Sufian, S. (2019). Photocatalytic degradation of real industrial poultry wastewater via platinum decorated $BiVO_4$/g-C_3N_4 photocatalyst under solar light irradiation. *Journal of Photochemistry and Photobiology A: Chemistry, 378*, 46-56.

Sarkar, P., & Nicholson, P. S. (1996). Electrophoretic deposition (EPD): mechanisms, kinetics, and application to ceramics. *Journal of the American Ceramic Society, 79*(8), 1987-2002.

Sasirekha, N., Basha, S. J. S., & Shanthi, K. (2006). Photocatalytic performance of Ru doped anatase mounted on silica for reduction of carbon dioxide. *Applied Catalysis B: Environmental, 62*(1-2), 169-180.

Sato, N., Kawachi, M., Noto, K., Yoshimoto, N., & Yoshizawa, M. (2001). Effect of particle size reduction on crack formation in electrophoretically deposited YBCO films. *Physica C: Superconductivity, 357*, 1019-1022.

Sato, S., Arai, T., Morikawa, T., Uemura, K., Suzuki, T. M., Tanaka, H., & Kajino, T. (2011). Selective CO_2 conversion to formate conjugated with H_2O oxidation utilizing semiconductor/complex hybrid photocatalysts. *Journal of the American Chemical Society, 133*(39), 15240-15243.

Schneider, J., Matsuoka, M., Takeuchi, M., Zhang, J., Horiuchi, Y., Anpo, M., & Bahnemann, D. W. (2014). Understanding TiO_2 photocatalysis: mechanisms and materials. *Chemical Reviews, 114*(19), 9919-9986.

Schreier, M., Gao, P., Mayer, M. T., Luo, J., Moehl, T., Nazeeruddin, M. K., . . . Grätzel, M. (2015). Efficient and selective carbon dioxide reduction on low cost protected Cu_2O photocathodes using a molecular catalyst. *Energy & Environmental Science, 8*(3), 855-861.

Schreier, M., Luo, J., Gao, P., Moehl, T., Mayer, M. T., & Grätzel, M. (2016). Covalent immobilization of a molecular catalyst on Cu_2O photocathodes for CO_2 reduction. *Journal of the American Chemical Society, 138*(6), 1938-1946.

Schulz, M., Karnahl, M., Schwalbe, M., & Vos, J. G. (2012). The role of the bridging ligand in photocatalytic supramolecular assemblies for the reduction of protons and carbon dioxide. *Coordination Chemistry Reviews, 256*(15-16), 1682-1705.

Schwarz, J. A., Contescu, C., & Contescu, A. (1995). Methods for preparation of catalytic materials. *Chemical Reviews, 95*(3), 477-510.

Serpone, N., Lawless, D., Khairutdinov, R., & Pelizzetti, E. (1995). Subnanosecond relaxation dynamics in TiO_2 colloidal sols (particle sizes Rp = 1.0-13.4 nm). Relevance to heterogeneous photocatalysis. *The Journal of Physical Chemistry, 99*(45), 16655-16661.

Serrà, A., Pip, P., Gómez, E., & Philippe, L. (2020). Efficient magnetic hybrid ZnO-based photocatalysts for visible-light-driven removal of toxic cyanobacteria blooms and cyanotoxins. *Applied Catalysis B: Environmental*, 118745-118755.

Setvín, M., Aschauer, U., Scheiber, P., Li, Y.-F., Hou, W., Schmid, M., . . . Diebold, U. (2013). Reaction of O_2 with subsurface oxygen vacancies on TiO_2 anatase (101). *Science, 341*(6149), 988-991.

Setvin, M., Shi, X., Hulva, J., Simschitz, T., Parkinson, G. S., Schmid, M., . . . Diebold, U. (2017). Methanol on anatase TiO_2 (101): Mechanistic insights into photocatalysis. *Acs Catalysis, 7*(10), 7081-7091.

Sfaelou, S., & Lianos, P. (2016). Photoactivated fuel cells (PhotoFuelCells). An alternative source of renewable energy with environmental benefits. *AIMS Materials Science, 3*, 270-288.

Shahid, M. M., Pandikumar, A., Golsheikh, A. M., Huang, N. M., & Lim, H. N. (2014). Enhanced electrocatalytic performance of cobalt oxide nanocubes incorporating reduced graphene oxide as a modified platinum electrode for methanol oxidation. *RSC Advances, 4*(107), 62793-62801.

Shahid, M. M., Rameshkumar, P., & Huang, N. M. (2015). Morphology dependent electrocatalytic properties of hydrothermally synthesized cobalt oxide nanostructures. *Ceramics International, 41*(10), 13210-13217.

Shang, M., Wang, W., Zhang, L., Sun, S., Wang, L., & Zhou, L. (2009). 3D Bi_2WO_6/TiO_2 hierarchical heterostructure: controllable synthesis and enhanced visible photocatalytic degradation performances. *The Journal of Physical Chemistry C, 113*(33), 14727-14731.

Shangguan, E., Tang, H., Chang, Z., Yuan, X.-Z., & Wang, H. (2011). Effects of different $Ni(OH)_2$ precursors on the structure and electrochemical properties of NiOOH. *International Journal of Hydrogen Energy, 36*(16), 10057-10064.

Sharma, A., Varshney, M., Shin, H. J., Lee, B.-H., Chae, K. H., & Won, S. O. (2017). Effect of Cu insertion on structural, local electronic/atomic structure and photocatalyst properties of TiO_2, ZnO and $Ni(OH)_2$ nanostructures: XANES-EXAFS study. *Materials Chemistry and Physics, 191*, 129-144.

Shawky, A., Mohamed, R., Mkhalid, I., Youssef, M., & Awwad, N. (2020). Visible light-responsive Ag/$LaTiO_3$ nanowire photocatalysts for efficient elimination of atrazine herbicide in water. *Journal of Molecular Liquids, 299*, 112163-112170.

Shen, M., & Henderson, M. A. (2011). Identification of the active species in photochemical hole scavenging reactions of methanol on TiO_2. *The Journal of Physical Chemistry Letters, 2*(21), 2707-2710.

Shen, Q., Chen, Z., Huang, X., Liu, M., & Zhao, G. (2015). High-yield and selective photoelectrocatalytic reduction of CO_2 to formate by metallic copper decorated Co_3O_4 nanotube arrays. *Environmental Science & Technology, 49*(9), 5828-5835.

Sheu, J.-K., Liao, P., Huang, T., Chiang, K., Lai, W.-C., & Lee, M. (2017). InGaN-based epitaxial films as photoelectrodes for hydrogen generation through water photoelectrolysis and CO_2 reduction to formic acid. *Solar Energy Materials and Solar Cells, 166*, 86-90.

Shi, J., Chen, J., Feng, Z., Chen, T., Lian, Y., Wang, X., & Li, C. (2007). Photoluminescence characteristics of TiO_2 and their relationship to the photoassisted reaction of water/methanol mixture. *The Journal of Physical Chemistry C, 111*(2), 693-699.

Shi, W., Guo, X., Cui, C., Jiang, K., Li, Z., Qu, L., & Wang, J.-C. (2019). Controllable synthesis of Cu_2O decorated WO_3 nanosheets with dominant (001) facets for photocatalytic CO_2 reduction under visible-light irradiation. *Applied Catalysis B: Environmental, 243*, 236-242.

Shionoya, M., Kimura, E., & Iitaka, Y. (1990). Mono-, di-and tetrafluorinated cyclams. *Journal of the American Chemical Society, 112*(25), 9237-9245.

Shojaeimehr, T., Tasbihi, M., Acharjya, A., Thomas, A., Schomäcker, R., & Schwarze, M. (2020). Impact of operating conditions for the continuous-flow degradation of diclofenac with immobilized carbon nitride photocatalysts. *Journal of Photochemistry and Photobiology A: Chemistry, 388*, 112182-112189.

Silvestre-Albero, J., Wahby, A., Sepúlveda-Escribano, A., Martínez-Escandell, M., Kaneko, K., & Rodríguez-Reinoso, F. (2011). Ultrahigh CO_2 adsorption capacity on carbon molecular sieves at room temperature. *Chemical Communications, 47*(24), 6840-6842.

Singh, S., Singh, G., & Bala, N. (2018). Electrophoretic deposition of bioactive glass composite coating on biomaterials and electrochemical behavior study: A review. *Materials Today: Proceedings, 5*(9), 20160-20169.

Singh, S., Singh, G., & Bala, N. (2020). Electrophoretic deposition of hydroxyapatite-iron oxide-chitosan composite coatings on Ti-13Nb-13Zr alloy for biomedical applications. *Thin Solid Films*, 137801-137812.

Siriwardane, R. V., Shen, M.-S., Fisher, E. P., & Losch, J. (2005). Adsorption of CO_2 on zeolites at moderate temperatures. *Energy & Fuels, 19*(3), 1153-1159.

Skinner, D. E., Colombo Jr, D. P., Cavaleri, J. J., & Bowman, R. M. (1995). Femtosecond investigation of electron trapping in semiconductor nanoclusters. *The Journal of Physical Chemistry, 99*(20), 7853-7856.

Song, C. (2006). Global challenges and strategies for control, conversion and utilization of CO_2 for sustainable development involving energy, catalysis, adsorption and chemical processing. *Catalysis Today, 115*(1-4), 2-32.

Song, W., Chen, Z., Brennaman, M. K., Concepcion, J. J., Patrocinio, A. O. T., Iha, N. Y. M., & Meyer, T. J. (2011). Making solar fuels by artificial photosynthesis. *Pure and Applied Chemistry, 83*(4), 749-768.

Spataru, N., Tokuhiro, K., Terashima, C., Rao, T. N., & Fujishima, A. (2003). Electrochemical reduction of carbon dioxide at ruthenium dioxide deposited on boron-doped diamond. *Journal of Applied Electrochemistry, 33*(12), 1205-1210.

Sreekanth, T., Ramaraghavulu, R., Vattikuti, S. P., Shim, J., & Yoo, K. (2019). Microwave synthesis: $ZnCo_2O_4$ NPs as an efficient electrocatalyst in the methanol oxidation reaction. *Materials Letters, 253*, 450-453.

Su, C., Hong, B.-Y., & Tseng, C.-M. (2004). Sol–gel preparation and photocatalysis of titanium dioxide. *Catalysis Today, 96*(3), 119-126.

Su, N., Hu, X., Zhang, J., Huang, H., Cheng, J., Yu, J., & Ge, C. (2017). Plasma-induced synthesis of Pt nanoparticles supported on TiO_2 nanotubes for enhanced methanol electro-oxidation. *Applied Surface Science, 399*, 403-410.

Subrahmanyam, M., Kaneco, S., & Alonso-Vante, N. (1999). A screening for the photo reduction of carbon dioxide supported on metal oxide catalysts for C_1–C_3 selectivity. *Applied Catalysis B: Environmental, 23*(2-3), 169-174.

Sui, X.-L., Wang, Z.-B., Yang, M., Huo, L., Gu, D.-M., & Yin, G.-P. (2014). Investigation on C–TiO_2 nanotubes composite as Pt catalyst support for methanol electrooxidation. *Journal of Power Sources, 255*, 43-51.

Sun, B., Liu, A., Li, J., Wang, J., & Wang, S. (2020). Development of novel highly stable synergistic quaternary photocatalyst for the efficient hydrogen evolution reaction. *Applied Surface Science*, 145498-145506.

Sun, M., Hu, J., Zhai, C., Zhu, M., & Pan, J. (2017). A pn heterojunction of CuI/TiO_2 with enhanced photoelectrocatalytic activity for methanol electro-oxidation. *Electrochimica Acta, 245*, 863-871.

Szaniawska, E., Bienkowski, K., Rutkowska, I. A., Kulesza, P. J., & Solarska, R. (2018). Enhanced photoelectrochemical CO_2-reduction system based on mixed Cu_2O–nonstoichiometric TiO_2 photocathode. *Catalysis Today, 300*, 145-151.

Tabesh, E., Salimijazi, H., Kharaziha, M., Mahmoudi, M., & Hejazi, M. (2019). Development of an in-situ chitosan-copper nanoparticle coating by electrophoretic deposition. *Surface and Coatings Technology, 364*, 239-247.

Tachikawa, T., Fujitsuka, M., & Majima, T. (2007). Mechanistic insight into the TiO_2 photocatalytic reactions: design of new photocatalysts. *The Journal of Physical Chemistry C, 111*(14), 5259-5275.

Taheri, M., Abdizadeh, H., & Golobostanfard, M. R. (2018). Hierarchical ZnO nanoflowers and urchin-like shapes synthesized via sol-gel electrophoretic deposition with enhanced photocatalytic performance. *Materials Chemistry and Physics, 220*, 118-127.

Takayama, T., Sato, K., Fujimura, T., Kojima, Y., Iwase, A., & Kudo, A. (2017). Photocatalytic CO_2 reduction using water as an electron donor by a powdered Z-scheme system consisting of metal sulfide and an RGO–TiO_2 composite. *Faraday Discussions, 198*, 397-407.

Takeda, H., & Ishitani, O. (2010). Development of efficient photocatalytic systems for CO_2 reduction using mononuclear and multinuclear metal complexes based on mechanistic studies. *Coordination Chemistry Reviews, 254*(3-4), 346-354.

Takeda, H., Koike, K., Inoue, H., & Ishitani, O. (2008). Development of an efficient photocatalytic system for CO_2 reduction using rhenium (I) complexes based on mechanistic studies. *Journal of the American Chemical Society, 130*(6), 2023-2031.

Takeda, H., Koike, K., Morimoto, T., Inumaru, H., & Ishitani, O. (2011). Photochemistry and photocatalysis of rhenium (I) diimine complexes *Advances in Inorganic Chemistry*, 63, 137-186.

Tan, S. S., Zou, L., & Hu, E. (2006). Photocatalytic reduction of carbon dioxide into gaseous hydrocarbon using TiO_2 pellets. *Catalysis Today, 115*(1-4), 269-273.

Tang, M., Ao, Y., Wang, P., & Wang, C. (2019). All-solid-state Z-scheme WO_3 nanorod/$ZnIn_2S_4$ composite photocatalysts for the effective degradation of nitenpyram under visible light irradiation. *Journal of Hazardous Materials*, 387, 121713-121723.

Tao, J., & Batzill, M. (2010). Role of surface structure on the charge trapping in TiO_2 photocatalysts. *The Journal of Physical Chemistry Letters, 1*(21), 3200-3206.

Tao, J., Luttrell, T., & Batzill, M. (2011). A two-dimensional phase of TiO_2 with a reduced bandgap. *Nature Chemistry, 3*(4), 296-300.

Tasbihi, M., Schwarze, M., Edelmannová, M., Spöri, C., Strasser, P., & Schomäcker, R. (2019). Photocatalytic reduction of CO_2 to hydrocarbons by using photodeposited Pt nanoparticles on carbon-doped titania. *Catalysis Today, 328*, 8-14.

Tian, L., Xing, L., Shen, X., Li, Q., Ge, S., Liu, B., & Jie, L. (2020). Visible light enhanced Fe–I–TiO_2 photocatalysts for the degradation of gaseous benzene. *Atmospheric Pollution Research, 11*(1), 179-185.

Tientong, J., Garcia, S., Thurber, C. R., & Golden, T. D. (2014). Synthesis of nickel and nickel hydroxide nanopowders by simplified chemical reduction. *Journal of Nanotechnology, 2014*, 1-6.

Tomita, Y., Teruya, S., Koga, O., & Hori, Y. (2000). Electrochemical reduction of carbon dioxide at a platinum electrode in acetonitrile-water mixtures. *Journal of The Electrochemical Society, 147*(11), 4164-4167.

Trasatti, S. (1991). Physical electrochemistry of ceramic oxides. *Electrochimica Acta, 36*(2), 225-241.

Trivedi, S., & Prasad, R. (2016). Reactive calcination route for synthesis of active Mn–Co_3O_4 spinel catalysts for abatement of CO–CH_4 emissions from CNG vehicles. *Journal of Environmental Chemical Engineering, 4*(1), 1017-1028.

Tsui, E. Y., Kanady, J. S., & Agapie, T. (2013). Synthetic cluster models of biological and heterogeneous manganese catalysts for O_2 evolution. *Inorganic Chemistry, 52*(24), 13833-13848.

Uddin, M. T., Nicolas, Y., Olivier, C. l., Toupance, T., M ll er, M. M., Kleebe, H.-J., . . . Jaegermann, W. (2013). Preparation of RuO_2/TiO_2 mesoporous heterostructures and rationalization of their enhanced photocatalytic properties by band alignment investigations. *The Journal of Physical Chemistry C, 117*(42), 22098-22110.

Usmaniya, U. M., Thampi, V. A., & Subramanian, B. (2019). Electrophoretic deposition of bioactive glass-nanoclay nanocomposites on titanium. *Applied Clay Science, 167*, 1-8.

Van der Biest, O. O., & Vandeperre, L. J. (1999). Electrophoretic deposition of materials. *Annual Review of Materials Science, 29*(1), 327-352.

Vázquez, A., Obregón, S., & Hernández-Uresti, D. (2020). Electrophoretic deposition of flower-like $CaBiVMoO_8$ particles for the photocatalytic degradation of pharmaceutical pollutants. *Colloid and Interface Science Communications, 34*, Article#100223.

Vedarajan, R., Ikeda, S., & Matsumi, N. (2014). Electrochemical characterization of TiO_2/WO_x nanotubes for photocatalytic application. *Nanoscale Research Letters, 9*(1), 573-577.

Vetrivel, V., Rajendran, K., & Kalaiselvi, V. (2015). Synthesis and characterization of pure titanium dioxide nanoparticles by sol-gel method. *International Journal of ChemTech Resesearch, 7*, 1090-1097.

Villarreal, T. L., Gomez, R., Neumann-Spallart, M., Alonso-Vante, N., & Salvador, P. (2004). Semiconductor photooxidation of pollutants dissolved in water: a kinetic model for distinguishing between direct and indirect interfacial hole transfer. I. Photoelectrochemical experiments with polycrystalline anatase electrodes under current doubling and absence of recombination. *The Journal of Physical Chemistry B, 108*(39), 15172-15181.

Wang, C., Shao, C., Zhang, X., & Liu, Y. (2009). SnO_2 nanostructures-TiO_2 nanofibers heterostructures: controlled fabrication and high photocatalytic properties. *Inorganic Chemistry, 48*(15), 7261-7268.

Wang, G., Sarkar, P., & Nicholson, P. S. (1997). Influence of acidity on the electrostatic stability of alumina suspensions in ethanol. *Journal of the American Ceramic Society, 80*(4), 965-972.

Wang, H., Zhang, L., Chen, Z., Hu, J., Li, S., Wang, Z., . . . Wang, X. (2014). Semiconductor heterojunction photocatalysts: design, construction, and photocatalytic performances. *Chemical Society Reviews, 43*(15), 5234-5244.

Wang, L., Hu, H., Xu, J., Zhu, S., Ding, A., & Deng, C. (2019). WO_3 nanocubes: Hydrothermal synthesis, growth mechanism, and photocatalytic performance. *Journal of Materials Research*, *34*(17), 2955-2963.

Wang, L., Jia, Y., Nie, R., Zhang, Y., Chen, F., Zhu, Z., . . . Jing, H. (2017). Ni-foam-supported and amine-functionalized TiO_2 photocathode improved photoelectrocatalytic reduction of CO_2 to methanol. *Journal of Catalysis, 349*, 1-7.

Wang, Q., Luo, J., Zhong, Z., & Borgna, A. (2011). CO_2 capture by solid adsorbents and their applications: current status and new trends. *Energy & Environmental Science, 4*(1), 42-55.

Wang, X., Kafizas, A., Li, X., Moniz, S. J., Reardon, P. J., Tang, J., . . . Durrant, J. R. (2015). Transient absorption spectroscopy of anatase and rutile: the impact of morphology and phase on photocatalytic activity. *The Journal of Physical Chemistry C, 119*(19), 10439-10447.

Wang, Y., Niu, C., & Wang, D. (2018). Metallic nanocatalysts for electrochemical CO_2 reduction in aqueous solutions. *Journal of Colloid and Interface Science, 527*, 95-106.

Wang, Y. C., Leu, I. C., & Hon, M. H. (2004). Kinetics of electrophoretic deposition for nanocrystalline zinc oxide coatings. *Journal of the American Ceramic Society, 87*(1), 84-88.

Wei, L., Shifu, C., Wei, Z., & Sujuan, Z. (2009). Titanium dioxide mediated photocatalytic degradation of methamidophos in aqueous phase. *Journal of Hazardous Materials, 164*(1), 154-160.

Wei, Z.-H., Wang, Y.-F., Li, Y.-Y., Zhang, L., Yao, H.-C., & Li, Z.-J. (2018). Enhanced photocatalytic CO_2 reduction activity of Z-scheme $CdS/BiVO_4$ nanocomposite with thinner $BiVO_4$ nanosheets. *Journal of CO_2 Utilization, 28*, 15-25.

White, J. L., Baruch, M. F., Pander III, J. E., Hu, Y., Fortmeyer, I. C., Park, J. E., . . . Yan, Y. (2015). Light-driven heterogeneous reduction of carbon dioxide: photocatalysts and photoelectrodes. *Chemical Reviews, 115*(23), 12888-12935.

Wilson, J. N., & Idriss, H. (2002). Structure sensitivity and photocatalytic reactions of semiconductors. Effect of the last layer atomic arrangement. *Journal of the American Chemical Society, 124*(38), 11284-11285.

Wu, H., Li, Y., Ren, J., Rao, D., Zheng, Q., Zhou, L., & Lin, D. (2019). CNT-assembled dodecahedra core@ nickel hydroxide nanosheet shell enabled sulfur cathode for high-performance lithium-sulfur batteries. *Nano Energy, 55*, 82-92.

Wu, N.-L., & Lee, M.-S. (2004). Enhanced TiO_2 photocatalysis by Cu in hydrogen production from aqueous methanol solution. *International Journal of Hydrogen Energy, 29*(15), 1601-1605.

Xia, Y., Yang, P., Sun, Y., Wu, Y., Mayers, B., Gates, B., . . . Yan, H. (2003). One-dimensional nanostructures: Synthesis, characterization, and applications. *Advanced Materials, 15*(5), 353-389.

Xie, S., Zhang, Q., Liu, G., & Wang, Y. (2016). Photocatalytic and photoelectrocatalytic reduction of CO_2 using heterogeneous catalysts with controlled nanostructures. *Chemical Communications, 52*(1), 35-59.

Xu, C., Sun, X. W., Dong, Z., Tan, S., Cui, Y., & Wang, B. (2005). Manganese-doped zinc oxide tetratubes and their photoluminescent properties. *Journal of Applied Physics, 98*(11), 113513-113518.

Xu, H., Ouyang, S., Li, P., Kako, T., & Ye, J. (2013). High-active anatase TiO_2 nanosheets exposed with 95% {100} facets toward efficient H_2 evolution and CO_2 photoreduction. *ACS Applied Materials & Interfaces, 5*(4), 1348-1354.

Xu, J., Gao, P., & Zhao, T. (2012). Non-precious Co_3O_4 nano-rod electrocatalyst for oxygen reduction reaction in anion-exchange membrane fuel cells. *Energy & Environmental Science, 5*(1), 5333-5339.

Xu, J., Sun, X., Shan, Y., Xu, J., Wang, G., & Wang, L. (2019). Enhanced UV-light driven photocatalytic performances and recycling properties of $TiO_2/AlON$ composite photocatalyst. *Ceramics International, 45*(6), 6767-6773.

Xu, M., Gao, Y., Moreno, E. M., Kunst, M., Muhler, M., Wang, Y., . . . Wöll, C. (2011). Photocatalytic activity of bulk TiO_2 anatase and rutile single crystals using infrared absorption spectroscopy. *Physical Review Letters, 106*(13), 138302-138305.

Xu, Q., Yu, J., Zhang, J., Zhang, J., & Liu, G. (2015). Cubic anatase TiO_2 nanocrystals with enhanced photocatalytic CO_2 reduction activity. *Chemical Communications, 51*(37), 7950-7953.

Xu, X., Zhou, X., Li, X., Yang, F., Jin, B., Xu, T., . . . Li, M. (2014). Electrodeposition synthesis of MnO_2/TiO_2 nanotube arrays nanocomposites and their visible light photocatalytic activity. *Materials Research Bulletin, 59*, 32-36.

Xu, Y., Gong, Y., Ren, H., Liu, W., Li, C., Liu, X., & Niu, L. (2018). Insight into enhanced photocatalytic H_2 production by $Ni(OH)_2$-decorated $Zn_xCd_{1-x}S$ nanocomposite photocatalysts. *Journal of Alloys and Compounds, 735*, 2551-2557.

Xu, Y., Lin, H., Li, L., Huang, X., & Li, G. (2015). Precursor-directed synthesis of well-faceted brookite TiO_2 single crystals for efficient photocatalytic performances. *Journal of Materials Chemistry A, 3*(44), 22361-22368.

Xu, Y., & Schoonen, M. A. (2000). The absolute energy positions of conduction and valence bands of selected semiconducting minerals. *American Mineralogist, 85*(3-4), 543-556.

Yamashita, H., Kamada, N., He, H., Tanaka, K.-i., Ehara, S., & Anpo, M. (1994). Reduction of CO_2 with H_2O on TiO_2 (100) and TiO_2 (110) single crystals under UV-irradiation. *Chemistry Letters, 23*(5), 855-858.

Yan, J., Wu, H., Chen, H., Pang, L., Zhang, Y., Jiang, R., . . . Liu, S. F. (2016). One-pot hydrothermal fabrication of layered β-$Ni(OH)_2$/g-C_3N_4 nanohybrids for enhanced photocatalytic water splitting. *Applied Catalysis B: Environmental, 194*, 74-83.

Yang, C.-C. (2002). Synthesis and characterization of active materials of $Ni(OH)_2$ powders. *International Journal of Hydrogen Energy, 27*(10), 1071-1081.

Yang, D., Wang, R., He, M., Zhang, J., & Liu, Z. (2005). Ribbon-and boardlike nanostructures of nickel hydroxide: Synthesis, characterization, and electrochemical properties. *The Journal of Physical Chemistry B, 109*(16), 7654-7658.

Yang, H., Yin, D., Gao, L., Zhang, X., Zhang, X., & Liu, Q. (2020). 5, 10, 15, 20-Tetrakis (4-carboxylphenyl) porphyrin modified nickel-cobalt layer double hydroxide nanosheets as enhanced photoelectrocatalysts for methanol oxidation under visible-light. *Journal of Colloid and Interface Science, 561*, 881-889.

Yang, Y.-h., Xie, R.-r., Hang, L., Liu, C.-j., Liu, W.-h., & Zhan, F.-q. (2016). Photoelectrocatalytic reduction of CO_2 into formic acid using WO_{3-x}/TiO_2 film as novel photoanode. *Transactions of Nonferrous Metals Society of China, 26*(9), 2390-2396.

Yang, Z., Wang, H., Song, W., Wei, W., Mu, Q., Kong, B., . . . Yin, H. (2017). One dimensional SnO_2 NRs/Fe_2O_3 NTs with dual synergistic effects for photoelectrocatalytic reduction CO_2 into methanol. *Journal of Colloid and Interface Science, 486*, 232-240.

Yoo, J. M., Ahn, C.-Y., Lee, J., & Sung, Y.-E. (2020). Effect of different surface functional groups on carbon supports toward methanol electro-oxidation of Pt nanoparticles. *Journal of Electroanalytical Chemistry*, 113931-113937.

Yu, H., Wang, D., Zhao, B., Lu, Y., Wang, X., Zhu, S., . . . Huo, M. (2020). Enhanced photocatalytic degradation of tetracycline under visible light by using a ternary photocatalyst of Ag_3PO_4/AgBr/g-C_3N_4 with dual Z-scheme heterojunction. *Separation and Purification Technology, 237*, 116365-116374.

Yu, J., Le, Y., & Cheng, B. (2012). Fabrication and CO_2 adsorption performance of bimodal porous silica hollow spheres with amine-modified surfaces. *RSC Advances, 2*(17), 6784-6791.

Yu, J., Low, J., Xiao, W., Zhou, P., & Jaroniec, M. (2014). Enhanced photocatalytic CO_2-reduction activity of anatase TiO_2 by coexposed {001} and {101} facets. *Journal of the American Chemical Society, 136*(25), 8839-8842.

Yu, J., Wang, S., Cheng, B., Lin, Z., & Huang, F. (2013). Noble metal-free $Ni(OH)_2$–gC_3N_4 composite photocatalyst with enhanced visible-light photocatalytic H_2-production activity. *Catalysis Science & Technology, 3*(7), 1782-1789.

Yu, K. M. K., Curcic, I., Gabriel, J., & Tsang, S. C. E. (2008). Recent advances in CO_2 capture and utilization. *ChemSusChem: Chemistry & Sustainability Energy & Materials, 1*(11), 893-899.

Yu, P., & Lampert, C. (1987). *Optical materials technology for energy and solar energy conversion VI.* Paper presented at the SPIE Optical and Optoelectronics Applied Science and Engineering Conference, 18 August 1987, San Diego, USA.

Yu, W., Liu, T., Cao, S., Wang, C., & Chen, C. (2016). Constructing MnO_2/single crystalline ZnO nanorod hybrids with enhanced photocatalytic and antibacterial activity. *Journal of Solid State Chemistry, 239*, 131-138.

Yuan, Y.-P., Ruan, L.-W., Barber, J., Loo, S. C. J., & Xue, C. (2014). Hetero-nanostructured suspended photocatalysts for solar-to-fuel conversion. *Energy & Environmental Science, 7*(12), 3934-3951.

Yus, J., Bravo, Y., Sanchez-Herencia, A. J., Ferrari, B., & Gonzalez, Z. (2019). Electrophoretic deposition of RGO-NiO core-shell nanostructures driven by heterocoagulation method with high electrochemical performance. *Electrochimica Acta, 308*, 363-372.

Zahn, D. T. (1999). Vibrational spectroscopy of bulk and supported manganese oxides. *Physical Chemistry Chemical Physics, 1*(1), 185-190.

Zanchi, E., Talic, B., Sabato, A., Molin, S., Boccaccini, A., & Smeacetto, F. (2019). Electrophoretic co-deposition of Fe_2O_3 and $Mn_{1.5}Co_{1.5}O_4$: Processing and oxidation performance of Fe-doped Mn-Co coatings for solid oxide cell interconnects. *Journal of the European Ceramic Society, 39*(13), 3768-3777.

Zangiabadi, M., Saljooqi, A., Shamspur, T., & Mostafavi, A. (2020). Evaluation of GO nanosheets decorated by $CuFe_2O_4$ and CdS nanoparticles as photocatalyst for the degradation of dinoseb and imidacloprid pesticides. *Ceramics International, 46*(5), 6124-6128.

Zeng, G., Qiu, J., Li, Z., Pavaskar, P., & Cronin, S. B. (2014). CO_2 reduction to methanol on TiO_2-passivated GaP photocatalysts. *ACS Catalysis, 4*(10), 3512-3516.

Zhang, D., Li, X., Guo, X., & Lai, C. (2014). Fabrication of cobalt oxide (Co_3O_4) coating by electrophoretic deposition. *Materials Letters, 126*, 211-213.

Zhang, M., Cheng, J., Xuan, X., Zhou, J., & Cen, K. (2016). CO_2 synergistic reduction in a photoanode-driven photoelectrochemical cell with a Pt-modified TiO_2 nanotube photoanode and a Pt reduced graphene oxide electrocathode. *ACS Sustainable Chemistry & Engineering, 4*(12), 6344-6354.

Zhang, M., Cheng, J., Xuan, X., Zhou, J., & Cen, K. (2017). Pt/graphene aerogel deposited in Cu foam as a 3D binder-free cathode for CO_2 reduction into liquid chemicals in a TiO_2 photoanode-driven photoelectrochemical cell. *Chemical Engineering Journal, 322*, 22-32.

Zhang, N., Li, L., Chu, Y., Zheng, L., Sun, S., Zhang, G., . . . Zhao, J. (2019). High Pt utilization efficiency of electrocatalysts for oxygen reduction reaction in alkaline media. *Catalysis Today, 332*, 101-108.

Zhang, N., Long, R., Gao, C., & Xiong, Y. (2018). Recent progress on advanced design for photoelectrochemical reduction of CO_2 to fuels. *Science China Materials, 61*(6), 771-805.

Zhang, Z., Wang, C.-C., Zakaria, R., & Ying, J. Y. (1998). Role of particle size in nanocrystalline TiO_2-based photocatalysts. *The Journal of Physical Chemistry B, 102*(52), 10871-10878.

Zhang, Z., & Yates Jr, J. T. (2010). Effect of adsorbed donor and acceptor molecules on electron stimulated desorption: O_2/TiO_2 (110). *The Journal of Physical Chemistry Letters, 1*(14), 2185-2188.

Zhang, Z., & Yates Jr, J. T. (2012). Band bending in semiconductors: chemical and physical consequences at surfaces and interfaces. *Chemical Reviews, 112*(10), 5520-5551.

Zhang, Z., Yuan, Y., Fang, Y., Liang, L., Ding, H., Shi, G., & Jin, L. (2007). Photoelectrochemical oxidation behavior of methanol on highly ordered TiO_2 nanotube array electrodes. *Journal of Electroanalytical Chemistry, 610*(2), 179-185.

Zhao, G.-Y., & Li, H.-L. (2008). Electrochemical oxidation of methanol on Pt nanoparticles composited MnO_2 nanowire arrayed electrode. *Applied Surface Science, 254*(10), 3232-3235.

Zhao, J., Wang, X., Xu, Z., & Loo, J. S. (2014). Hybrid catalysts for photoelectrochemical reduction of carbon dioxide: a prospective review on semiconductor/metal complex co-catalyst systems. *Journal of Materials Chemistry A, 2*(37), 15228-15233.

Zhao, Y., Zhan, L., Tian, J., Nie, S., & Ning, Z. (2010). MnO_2 modified multi-walled carbon nanotubes supported Pd nanoparticles for methanol electro-oxidation in alkaline media. *International Journal of Hydrogen Energy, 35*(19), 10522-10526.

Zhao, Z., Lin, J., Wang, G., & Muhammad, T. (2015). Novel Co-Mn-O nanosheet catalyst for CO preferential oxidation toward hydrogen purification. *AIChE Journal, 61*(1), 239-252.

Zhitomirsky, I. (2002). Cathodic electrodeposition of ceramic and organoceramic materials: Fundamental aspects. *Advances in colloid and Interface Science, 97*(1-3), 279-317.

Zhitomirsky, I., & Gal-Or, L. (1997). Electrophoretic deposition of hydroxyapatite. *Journal of Materials Science: Materials in Medicine, 8*(4), 213-219.

Zhou, H., Peng, J., Qiu, X., Gao, Y., Lu, L., & Wang, W. (2017). β-$Ni(OH)_2$ nanosheets: an effective sensing platform for constructing nucleic acid-based optical sensors. *Journal of Materials Chemistry B, 5*(35), 7426-7432.

Zhou, M., Wei, Z., Qiao, H., Zhu, L., Yang, H., & Xia, T. (2009). Particle size and pore structure characterization of silver nanoparticles prepared by confined arc plasma. *Journal of Nanomaterials, 2009*, 3.

Zhou, X., Lan, J., Liu, G., Deng, K., Yang, Y., Nie, G., . . . Zhi, L. (2012). Facet-Mediated Photodegradation of Organic Dye over Hematite Architectures by Visible Light. *Angewandte Chemie International Edition, 124*(1), 182-186.

Zhou, X., Liu, R., Sun, K., Chen, Y., Verlage, E., Francis, S. A., . . . Xiang, C. (2016). Solar-driven reduction of 1 atm of CO_2 to formate at 10% energy-conversion efficiency by use of a TiO_2-protected III–V tandem photoanode in conjunction with a bipolar membrane and a Pd/C cathode. *ACS Energy Letters, 1*(4), 764-770.

Zhou, X., Xia, Z., Zhang, Z., Ma, Y., & Qu, Y. (2014). One-step synthesis of multi-walled carbon nanotubes/ultra-thin $Ni(OH)_2$ nanoplate composite as efficient catalysts for water oxidation. *Journal of Materials Chemistry A, 2*(30), 11799-11806.

Zhu, H., Gong, L., & Li, Z. (2020). Construction and mechanism of a novel Z-scheme photocatalyst α-Fe_2O_3/P3HT with O-Ti-O for organic pollutant degradation under visible light. *Applied Surface Science, 505*, 144639-144653.

Zhu, J., Chen, F., Zhang, J., Chen, H., & Anpo, M. (2006). Fe^{3+}-TiO_2 photocatalysts prepared by combining sol–gel method with hydrothermal treatment and their characterization. *Journal of Photochemistry and Photobiology A: Chemistry, 180*(1-2), 196-204.

Zhu, J., Faria, J. L., Figueiredo, J. L., & Thomas, A. (2011). Reaction Mechanism of Aerobic Oxidation of Alcohols Conducted on Activated-Carbon-Supported Cobalt Oxide Catalysts. *Chemistry–A European Journal, 17*(25), 7112-7117.

Zhu, M., Zhai, C., & Lu, C. (2016). Novel photoelectrocatalytic electrodes materials for fuel cell reactions *Advanced Electrode Materials, Ch. 11* (pp. 435-456). NJ, USA: John Wiley & Son.

Zouzelka, R., Remzova, M., Brabec, L., & Rathousky, J. (2018). Photocatalytic performance of porous TiO_2 layers prepared by quantitative electrophoretic deposition from organic solvents. *Applied Catalysis B: Environmental, 227*, 70-78.

LIST OF PUBLICATIONS AND PAPERS PRESENTED

PUBLICATIONS

1. **Mat, A.N.C.**, Sairi, N.A., Basirun, W.J., Rezayi, M., Teridi, M.A.M., Mazhar, M. (2019). Photoelectrocatalytic oxidation of methanol over RuO_2-MnO_2-Co_3O_4 supported porous anatase under visible light irradiation. *Materials Chemistry and Physics*, 224, 196 – 205.

2. **Mat, A.N.C.**, Sairi, N.A., Basirun, W.J., Mehmood, M.S. (2020). Photoelectrochemical reduction of CO_2 over Ru/Mn/Co trimetallic catalyst supported anatase TiO_2 under visible light irradiation. *Journal of Sol-gel Science and Technology*, DOI: 10.1007/s10971-020-05277-0.

PAPER PRESENTED

Ahmad Nazeer Che Mat, Nor Asrina Sairi, Wan Jefrey Basirun, Mohd Asri Mat Teridi, Muhammad Mazhar (2016). *Photoelectro-oxidation of methanol over trimetallic catalyst supported onto anatase.* Paper presented at International Conference on Catalysis, 21st –22nd September 2016, Johor Bahru, Malaysia.